8-2014

Optimization of Plasmon Decay Through Scattering and Hot Electron Transfer

Drew DeJarnette
University of Arkansas, Fayetteville

Citation

DeJarnette, D. (2014). Optimization of Plasmon Decay Through Scattering and Hot Electron Transfer. *Graduate Theses and Dissertations* Retrieved from https://scholarworks.uark.edu/etd/2266

Optimization of Plasmon Decay Through Scattering and Hot Electron Transfer

Optimization of Plasmon Decay Through Scattering and Hot Electron Transfer

A dissertation submitted in partial fulfillment
of the requirements for the degree of
Doctor of Philosophy in Microelectronics-Photonics

By

Drew DeJarnette
Drury University
Bachelor of Arts in Physics and Mathematics, 2008
Missouri State University
Master of Science in Mathematics, 2010
University of Arkansas
Master of Science in Microelectronics-Photonics, 2012

August 2014
University of Arkansas

This dissertation is approved for recommendation to the Graduate Council.

Dr. D. Keith Roper
Dissertation Director

Dr. Laurent Bellaiche Committee Member	Dr. Salvador Barraza-Lopez Committee Member
Dr. Rick Ulrich Committee Member	Prof. Ken Vickers Ex-Officio Member

The following signatories attest that all software used in this dissertation was legally licensed for use by Mr. Drew DeJarnette for research purposes and publication.

Mr. Drew DeJarnette, Student	Dr. D. Keith Roper, Dissertation Director

This dissertation was submitted to http://www.turnitin.com for plagiarism reviewed by the TurnItIn company's software. The signatories have examined the report on this dissertation that was returned by TurnItIn and attest that, in their opinion, the items highlighted by the software are incidental to common usage and are not plagiarized material.

Prof. Ken Vickers, Program Director	Dr. D. Keith Roper, Dissertation Director

Abstract

Light incident on metal nanoparticles induce localized surface oscillations of conductive electrons, called plasmons, which is a means to control and manipulate light. Excited plasmons decay as either thermal energy as absorbed phonons or electromagnetic energy as scattered photons. An additional decay pathway for plasmons can exist for gold nanoparticles situated on graphene. Excited plasmons can decay directly to the graphene as through hot electron transfer. This dissertation begins by computational analysis of plasmon resonance energy and bandwidth as a function of particle size, shape, and dielectric environment in addition to diffractive coupled in lattices creating a Fano resonance. With this knowledge, plasmon resonance was probed with incident electrons using electron energy loss spectroscopy in a transmission electron microscope. Nanoparticles were fabricated using electron beam lithography on 50 nanometer thick silicon nitride with some particles fabricated with a graphene layer between the silicon nitride and metal structure. Plasmon resonance was compared between ellipses on and off graphene to characterize hot electron transfer as a means of plasmon decay. It was observed that the presence of graphene caused plasmon energy to decrease by as much as 9.8% and bandwidth to increase by 25%. Assuming the increased bandwidth was solely from electron transfer as an additional plasmon decay route, a 20% efficiency of plasmon decay to graphene was calculated for the particular ellipses analyzed.

Acknowledgments

The dissertation would never have come to completion without the guidance and mentoring of my advisor, Dr. Keith Roper. I am indebted to his advice and direction in the completion of this research. I would also like to thank Ken Vickers for his dedication to training and preparing myself and other Microelectronic-Photonics graduate students. Both of these individuals have helped prepare me for my next career step in understanding research as a method, leadership and mentorship, and professional development.

I would also like to acknowledge previous graduate students in Dr. Keith Roper's research group. Dr. Phillip Blake was instrumental in helping me understand and become competent in scanning electron microscopy and electron beam lithography.

Current members of Dr. Keith Roper's group have also been greatly appreciated in completion of this work. In particular, I would like to thank Greg Forcherio for helping with simulation results for far-field spectral analysis.

Furthermore, I would like to thank the Nano Institute for training and use of equipment used in this work. In particular, Dr. Mourad Benemara was particularly helpful in training on transmission electron microscopy for the main experimentation of this dissertation. Completion of this work would not have been possible without his guidance. Also, I would to thank Dr. Mike Hawkridge for helping me with X-ray photoelectron spectroscopy.

I would like to thank my committee members. Each of them have given from their time to support my work and help in the completion of this dissertation.

To my wife and children, who have been supportive of my time and efforts to complete this work. My family are helpers and motivators in life. Without their emotional support, encouragement, and uplifting words, this work would not have been possible.

Financial support. I am indebted to several financial institutions which allowed this work to be performed. I would like to thank the University of Arkansas foundation and the Walton Charitable foundation for support through the Doctoral Academic Fellowship and travel grants to present

my findings at scientific conferences. Additionally, I would like to thank the National Science Foundation for providing funding through grants NSF CMMI-0909749, NSF CMMI-1006927, NSF CBET-1134222. Any opinions, findings, and conclusions or recommendations expressed in this material are those of the author and do not necessarily reflect the views of the National Science Foundation.

Table of Contents

List of Figures

List of Tables

Chapter 1: Introduction

When light passes through an interface where the dielectric function changes sign, a surface wave of electron oscillation can be generated. The evanescent wave can propagate across surface in two-dimensional sheets or can be localized when materials are confined to the nanoscale in all three dimensions. This localized surface wave of electrons is called a localized surface plasmon.

Materials that have a negative dielectric function can support these plasmon oscillations. Such materials includes metals, which have a frequency dependent dielectric function that is negative in the ultra violet to infrared spectrum. This allows increased absorption or scattering of light through surface plasmon decay for devices that depend on enhanced optics. Resonance of plasmon oscillation can be tuned by changing the size, shape, and composition of the nanoparticle as well as changing the refractive index surrounding the particles. This freedom allows tunable optics for frequency dependent applications.

This dissertation considers computational and experimental characterization of plasmon resonance in metal nanostructures. Optical properties were probed with light excitation and characterized with parametric changes in particle size, shape, and dielectric environment. Periodic arrangement of nanoparticles were predicted to give a coupled, Fano resonance between plasmon oscillation and diffracted light. Consideration of individual particle plasmon resonance was performed using electron energy loss spectroscopy in a scanning transmission electron microscope. This technique gave sub-nanometer resolution when determining optical properties of select nanoscale structures. Experimental results were compared to computational techniques to more fully understand the observed physical phenomenon.

Excited electrons from metal nanoparticles were considered with the graphene substrate to consider the possible decay of plasmons into direct transfer into the graphene. Ellipses fabricated on and off graphene were analyzed using electron energy loss spectroscopy and compared to consider the effect of graphene on plasmon resonance. Shifts in plasmon energy and broadening in bandwidth allowed testing of the hypothesis that excited plasmons in nanoparticles can decay directly into graphene which could be used as photocurrent.

In regards to nomenclature, the following terms are used throughout this dissertation:

- *Plasmon*. Quantization of electron gas oscillation relative to stationary atoms in a metal.
- *Surface Plasmon*. A surface plasmon is a surface oscillation of electrons at the interface of two materials through which the real part of the dielectric function changes signs.
- *Localized Surface Plasmon* (LSP). A stationary surface plasmon that is confined to a surface in all three dimensions, typically supported by nanoparticles.
- *Localized Surface Plasmon Resonance* (LSPR). The resonant frequency of the LSP.
- *Fano Resonance*. Coupling between a broad-band and narrow-band resonance resulting in an asymmetric resonance lineshape.
- *Polarizability* (α). Describes the ability of a dipole to response to an incident electric field. Computational models used in this dissertation replaces each particle with a collection of point dipole.
- *Electron energy loss spectroscopy*. Characterization technique performed in a transmission electron microscope where loss energy is evaluated from transmitted electrons.

1.1 Motivation

Demand for understanding photon-matter interactions at interfaces has increased as nanoscience and technology has advanced and true two-dimensional materials have been discovered. This work seeks to further this knowledge by experimental valuation of plasmon-graphene interactions for enhanced surfaces in photonic applications. Plasmonic nanoparticles and graphene have been incorporated in devices for application in alternative energy, energy transport, sensing, and medical applications. Deepening understanding of fundamental interactions will help guide new devices and enhance existing platforms in these applications.

1.2 Dissertation Structure

This dissertation is broken into three main sections, Background, computation, and experimental. Chapters 2 and 3 introduce the background material of electrodynamics and graphene. Chapters 4 through 6 address computational models and results to simulate optical properties of metal nanoparticles. Chapters 7 and 8 discuss the experimental aspect including fabrication and characterization of structures. Finally, Chapter 9 concludes this dissertation.

Chapter 2: Electromagnetic Theory of Plasmons

2.1 Introduction

Light incident on subwavelength metal nanostructures can induce surface waves of electrons at the interface between the metal and the environment. This oscillation of surface electrons is known as a plasmon. A plasmon can only be supported on an interface through with the dielectric function changes signs. Energy and bandwidth of the resonance is determined by particle morphology, composition, proximal density to other structures, and environmental considerations. Bandwidth of the resonance can be related to the time a plasmon exists before decaying. Plasmon resonance in a isolated nanoparticle can decay either as a phonon through absorption or a photon through scattering. Applications in sensing [1], surface enhanced Raman spectroscopy (SERS) [2], antennae [3], Light trapping and guiding [4], nanorulers [5], and similar technologies have all been enhanced through use of plasmon oscillation.

Material dielectric describes the response of electrons in a material to an incident electric field. Dielectric properties of a materials is given by $\epsilon = \epsilon_0 \epsilon_r$ where ϵ_0 is the permittivity of free space. Dielectric functions, related to the refractive index (RI) of the material, are dependent on frequency of incident light. For non-magnetic materials considered here (i.e. $\mu_r = 1$) the relation between refractive index, n, and material dielectric, ϵ_r, is [6, 7]

$$n(\omega) = \sqrt{\epsilon_r(\omega)}. \tag{2.1.1}$$

Depending on the sign and whether dielectric function is real or complex valued, the refracted index can be purely real, indicating no losses, or complex, indicating dispersion. The real component of RI corresponds to how much light bends as it transmits through a material in accordance with Snell's Law. The imaginary component of RI indicates attenuation of light as it travels through the material.

Response of electrons to incident electric fields induces dipoles in, or polarizes, the material. Polarization, $\mathbf{P}$, of the materials is expressed as of the material.

$$\mathbf{P} = \epsilon_0 \chi_e \mathbf{E} \tag{2.1.2}$$

where $\mathbf{E}$, is the incident electric field vector and χ_e is the electric susceptibility of the material [7]. From the definition of the displacement vector,

$$\mathbf{D} = \epsilon_0 \mathbf{E} + \mathbf{P} = \epsilon_0 (1 + \chi_e) \mathbf{E}. \tag{2.1.3}$$

Given that $\mathbf{D} = \epsilon \mathbf{E}$ we have an expression for the dielectric function of a material with

$$\epsilon = \epsilon_0 (1 + \chi_e). \tag{2.1.4}$$

As a result, $\epsilon_r = 1 + \chi_e$. Deriving a function to obtain numerical values of χ_e for metals can be an involved process and is not explained in detail here.

Coherent oscillation of surface conduction electrons coupled to incident light is possible in metals due to their dielectric properties. Bulk metal dielectric functions are complex valued with the real component being negative for most metals in the visible region. Plasmon resonance in nanoparticles occurs at specific negative values of the real part of the dielectric function which depends on the size and shape of the particle. For example, spheres that are much smaller than the incident wavelength of light (less than 40 nm diameter) have a plasmon resonance at frequencies where the real part of the dielectric function equals -2. For Au, this occurs at a vacuum wavelength of approximately 520 nm.

2.2 Plasmon Excitation

Plasmons in metal nanoparticles are excited by incident electric fields. These electric fields can be the result of either incident photons or electrons. In photons, the incident light is a sinusoidal electric field which is oscillating orthogonally to the direction of propagation. The polarized light induces a charge distribution on the nanoparticle which can be dipolar, quadrupolar, or a higher order electric mode. Excitation of a particular electric mode depends on the size and shape of the structure as well the incident wavelength of light.

Plasmon modes can also be excited with a high energy sub-nanometer electron probe incident into or near the structure [8]. An incident electron beam possesses an electric field pointing radially inwardly orthogonal to the direction of incidence. Energy is transferred from the incident electrons to the structure through excitation of a plasmon. Amount of energy lost to the structure is associated with the energy of the plasmon resonance. This energy loss can be measured using a technique called energy electron loss spectroscopy as detailed in Sections 4.3.2 and 8.2.

2.3 Isolated Structures

Single nanoparticles can include many different types of shapes including spheres, spheroids, disks, rings, stars, rods, various polygons, L-shaped, U-shaped, and many more [9, 10, 11]. Plasmon resonance can be tuned from the ultraviolet to infrared spectral range by careful design of nanostructure shape. For shapes topologically identical to a sphere (i.e. solid, connected shapes with no holes), the plasmon resonance tends to redshift with increasing particle size [13, 14]. This is a result of two main factors. First, as the ratio of particle size to wavelength increases, retardation effects of the electric field magnitude across the particle cause depolarization of the induced electric mode. Second, increasing particle size causes more spontaneous light emission to occur which results in a reduction of the resonance energy. Particles with an additional degree of freedom, such as wall thickness in nanorings, have more complicated trends in plasmon resonance shifting. The case of rings is discussed in more detail in Section 6.4.

Resonance location for the induced plasmon can be adjusted by changing the incident polarization angle. For high-symmetry shapes, such as triangles, spheres, and rings, plasmon resonance is not affected by polarization angle [15, 16]. However, low-symmetry shapes have been shown to exhibit significant shifting of the plasmon resonance as polarization angle changes [17, 18]. To explain this, consider the simple case of an ellipse. Without loss of generality, assume the semi-major axis is situated along the x-axis and the semi-minor axis is along the y-axis with incident light along the z-axis. As particle size increases for spheroids, such as the considered ellipse, plasmon resonance redshifts. For light polarized along the x-axis, the particle will be effectively larger than excited along the y-axis. This results in a plasmon resonance that is redshifted when polarized along the long axis as opposed to the short axis. Similar geometric arguments could be made to explain the resonance shifting of more complicated shapes as well.

2.4 Interacting Structures

Nanostructures in proximity to each other interact to shift and/or alter bandwidth of the plasmon resonance. This can be broken into two separate categories of near-field and far-field interactions [19]. Near-field interactions occur when particles are spaced less than approximately 200 nm from each other. More intense interactions indicated by a stronger electric field occur at proximities of less than approximately five to ten nanometers. These near-field interactions occur as dipole-dipole or dipole-higher, order, pole interactions. A single induced dipole creates its own electric field which is superimposed with the incident field to modify the total field on a second, adjacent particle.

Far-field interactions are supported by nanoparticles spaced at distances larger than the plasmon resonance wavelength. Recall for Au, the plasmon resonance wavelength is a minimum of 520 nm. Additionally, the nanostructure must possess primarily scattering of light as opposed to absorption. At spacings near the wavelength of light, scattered light can be in phase with the incident, oscillating electric field. Lattices of such nanoparticles create diffraction patterns from constructive and destructive interference patterns [20, 21, 22]. Narrow-band diffracted resonance coupling to the broad-band plasmon resonance has resulted in an asymmetric Fano resonance [3].

This dissertation will discuss both interacting and isolated nanostructures. Nanoparticle interactions will be given in the context of far-field interactions in nanoparticle lattices creating a Fano resonance. Computational analysis was done to assess nanoparticle and lattice geometry in addition to the dielectric environment showing effects on plasmon and Fano resonance to parametric changes. Isolated nanoparticle analysis is given in the context of microscopic plasmon fields with localized excitation using an incident electron probe. Interactions with a graphene substrate were found to shift and broaden the observed plasmon resonance in single nanostructures.

Chapter 3: Graphene

All life on earth is based on the element, Carbon (C). A compound is considered organic if one of its constituent elements is C. There are two forms that the element C has been observed to take: Diamond and graphitic. Diamond carbon is found in a single form when all four valence electrons in carbon are bonded in a 3D lattice. Graphitic carbon occurs when only three of the four valence electrons bond in a 2D plane. This monolayer of graphitic carbon is known as graphene. Manipulation of the graphitic carbon allows 3D, 2D, 1D, and 0D forms known respectively as graphite, graphene, carbon nanotubes (CNT), and fullerenes. These forms have the same hexagonal-based shape and is described as looking like a honeycomb. Graphite is a 3D material composed of stacked layers of 2D C sheets of graphene. Graphene layers can be rolled up to form 1D CNTs . Closed spheres, or ellipsoids, of carbon are known as the 0D fullerene, the most well-known is C_{60} or ”buckeyball”. The building block of all the graphitic carbon forms is 2D graphene. The focus of this chapter is to introduce the basic properties of graphene.

3.1 History

Carbon is an extremely important and versatile element. It is an excellent industrial lubricant (graphite), a beautiful and strong material (diamond), a good absorber of gas (charcoal), and is used to power a large amount of this country (coal) [23]. It has been used by man almost since there has been man and has been utilized as a tool since it was introduced in pencils in the 1600’s [23]. Graphene, however, has been of much more recent interest.

Before the two dimensional material became available, carbon nanotubes (CNT) were becoming increasingly important in nanotechnology. CNTs are rolled up sheets of graphene so much of the theory and experimental work on them is closely related to graphene sheets. CNTs were discovered in 1991 and haven been shown to be stronger than steel and can switch between insulating, semiconducting, and conducting [24].

Graphene was discovered to exist in a free-standing state in 2004 for which the discoverers earned the 2010 Nobel Prize in Physics. However, assessment of the material goes back much farther. Graphene has been studied theoretically since the 1940's [25] and experimentally since the 1960's [26]. It was a surprise that freestanding graphene was discovered since it was predicted that 2D crystals were too unstable to exist without support [27]. Once the extraordinary theoretical predictions of graphene were confirmed experimentally by its discoverers [28], the amount of publications on the material grew exponentially. A large portion of recent research has been on large scale industrial growth and device applications.

3.2 Electronic and Optical Properties

Carbon is the sixth element in the periodic table with two valence electron filling the $1s^2$ orbital and four electrons filling the $2s$ and $2p$ orbital states. In graphene, three of the conduction electron form sp^3 hybridized σ bonds at 120 degrees in the 2D plane. This arrangement forms the honeycomb lattice with the remaining conduction electron having an sp^2 hybridized π orbital orthogonal to the honeycomb lattice. Stacked graphene sheets are attracted together with electrostatic van der Walls forces resulting from this lone electron. This π electron is also responsible for the extraordinary electronic and optical properties found in graphene.

The honeycomb structure of graphene is not itself a Bravais lattice, but forms two interlaced face-centered rectangular Bravais lattices. Each lattice can be thought of as being its own Bravais sublattice. Solving for electron transport under this lattice in graphene is typically done using the nearest neighbor approximation under the tight-binding method. This method dictates that electron do not hop between atoms of the same sublattice, but only hop from an element of one sublattice to an element of the other sublattice. The dispersion relation of graphene gives the familiar Dirac cone around the K points in reciprocal space, corresponding to atomic locations in the lattice with the Fermi energy located at the crossover point. As a result of the sublattice hoping, electrons do not obey the Schrdinger equation, but instead follow Dirac's equation with each sublattice representing a pseudo spin state of the electrons.

The Hamiltonian of electrons in graphene following the Dirac equation is analogous to massless Dirac fermions. Expanding the Hamiltonian around the K points yields the form

$$\hat{H}_K = -i\hbar v\vec{\sigma} \cdot \nabla \tag{3.2.1}$$

where v is the electron velocity at the K point, $\hbar$ is Plank's constant divided by 2π, $\vec{\sigma}$ are the Pauli spin matrices, and $\nabla$is the gradient operator [29]. Due to the form of the Hamiltonian, the electrons traveling through graphene can be considered ultrarelativistic with velocity, v, approximately one three hundredth the speed of light. This property leads to an electron mobility, μ, in freestanding graphene of approximately $10^4 - 4 \times 10^5 \mathrm{cm}^2\mathrm{V}^{-1}\mathrm{s}^{-1}$, compared to $1.35 \times 10^3 \mathrm{cm}^2\mathrm{V}^{-1}\mathrm{s}^{-1}$ in room temperature Silicon [30].

Graphene has also shown to possess extraordinary optical properties as well as electrical. These properties are governed by the interaction of electrons in graphene to incident photons. The electron-photon interaction of two dimensional, massless Dirac Fermions is described by the fine structure constant given as [29]

$$\alpha = \frac{e^2}{\hbar c} \approx \frac{1}{137.036}, \tag{3.2.2}$$

where e is the fundamental charge and c is the speed of light. The modified Hamiltonian of the electrons in the presence of the electric field from incident photons is expressed as

$$\hat{H} = \hat{H}_0 + \hat{H}_{\mathrm{int}} \tag{3.2.3}$$

with

$$\hat{H}_{\mathrm{int}} = \frac{iev}{2\omega}\vec{\sigma}\vec{E}. \tag{3.2.4}$$

This interaction induces absorption of incident photons by valence electrons into the conduction band about the Dirac cone as illustrated in Figure 3.1. Assuming that the propagation of incident photons is orthogonal to the plane of graphene. The absorption probability determined using

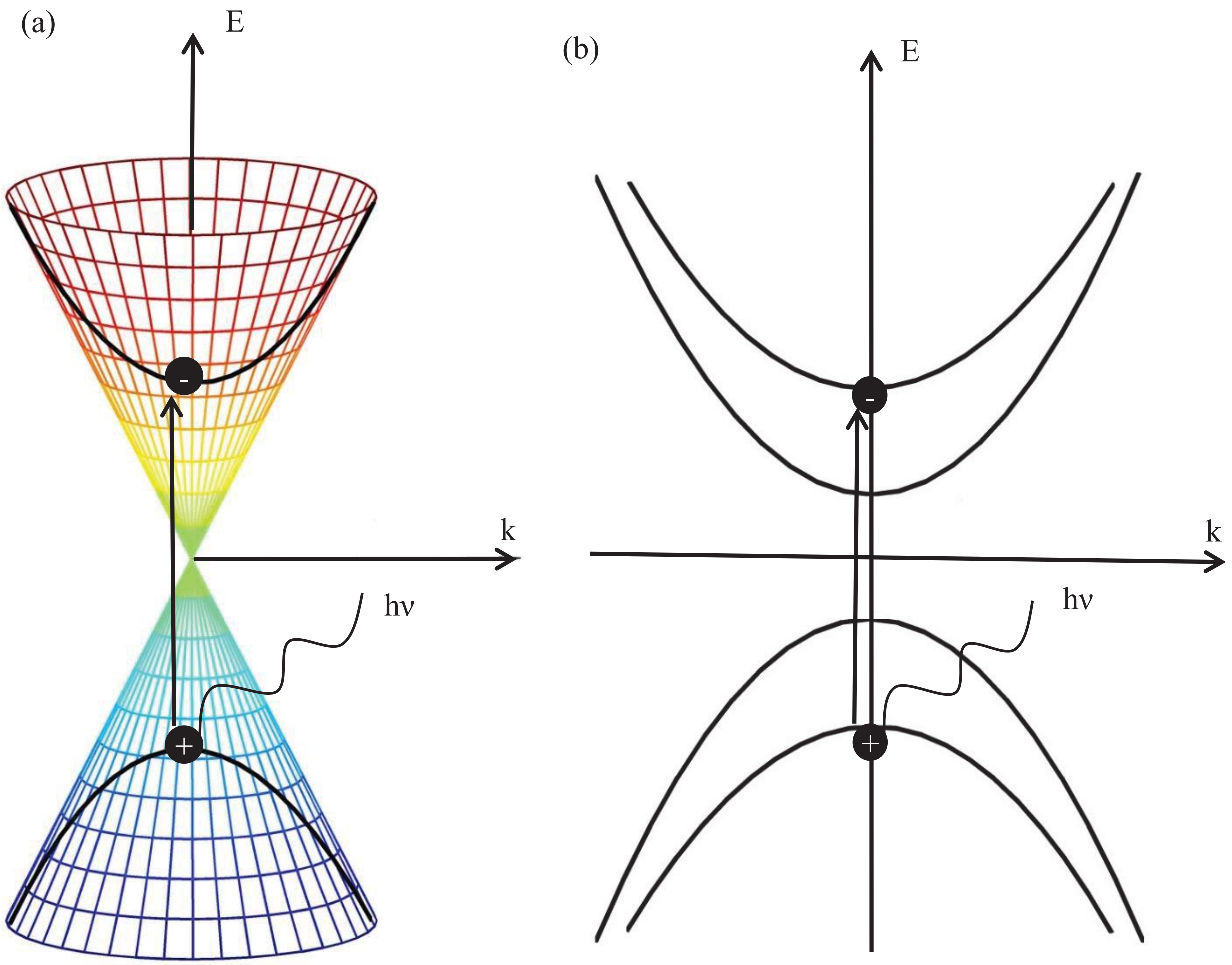

Figure 3.1: Band structure of intrinsic graphene showing (a) Dirac cone about atomic site with electron excited to conduction band with incident light and (b) vertical plane showing excitation of the same valence band electron to conduction band electron through incident light in graphene.

perturbation theory yields an absorption coefficient given by

$$\eta = \pi\alpha_f \tag{3.2.5}$$

where α_f is the fine structure constant defined in Equation 3.2.2. This gives an absorption of approximately 2.3% per monolayer of graphene over a broad range of visible light. This is due to the 1-2 eV visible band being much larger than the Fermi level and band transitions in graphene.

Absorption of 2.3% makes graphene virtually transparent to the naked eye. However, this value is remarkably high considering it is only a monolayer thick. For example, a 10 nm thick gallium arsenic (GaAs) layer near the band gap absorbs approximately 1% of incident light [31]. Even with this relatively large absorption of a graphene monolayer, improvements still need to be made for optical devices. Stacking additional layers on top is one method to linearly increase absorption, but at the cost of a reduction of the remarkable electrical properties. An alternative method to increase absorption in graphene without sacrificing the high mobility of electron transport is to decorate the surface with metal nanoparticles.

Metal nanoparticles possess optical absorption and scattering properties through plasmonic oscillation of the conduction electrons as described in Chapter 2. This ability has been combined with graphene in recent years to couple the electronic properties of graphene with the tunable absorption properties of metal nanoparticles [32, 33, 34, 35]. Combination of the nanoparticle/graphene composite has been previously shown to induce enhanced photocurrent of more than 800% by increased electron-hole pair generation [32].

Increased generation of electron-hole pairs occurs in one of two ways. First, increased electron-hole pairs can be by direct excitation (DE) [36, 37, 38, 39]. Typically, electron-hole pairs in graphene recombine in a matter of picoseconds [40]. It has been shown that the bending of the graphene band structure occurs from internal fields near metal contacts [40]. The plasmonic nanoparticles increase the electric field in the graphene around each structure when the plasmon mode is excited with incident photons with energy corresponding to the plasmon energy. The modified electric field allows increased separation of the induced electron-hole pair when a voltage is applied across the graphene.

Second, increased photocurrent in graphene from metal nanostructures can occur through transfer of hot electrons (HE) [37, 41, 42, 43]. Absorption of incident photons by the nanostructure induces an electron oscillation, or plasmon, within the nanostructure. This electron can decay through transference from the nanoparticle to the graphene [42, 44]. The transferred hot electron would be taken to the contact and contribute to the total photocurrent. While both DE and HE contributions occur in graphene, there is debate as to their relative importance in any given application. In this dissertation, electric fields from plasmonic nanostructures were modeled and mapped to predict nanostructures that would be efficient at generating electrons in graphene based photodevices.

3.3 Growth

The 2010 Nobel Prize in Physics was awarded to Andre Geim and Konstantin Novoselov from the University of Manchester for being the first ones to produce a stable graphene monolayer. They developed the few-layered graphene (FLG) by mechanical exfoliation of bulk graphite [28]. Sheets as large as 10 μm of FLG were seen by this process. One way to increase the size of the graphene sheets was to add an additional layer of polymethyl methacrylate (PMMA) to improve adhesion [45]. These sheets were large enough to characterize the material, but not for industrial scale device production. Since the isolation of graphene in 2004, several more consistent and large scale methods for growing graphene have been realized.

One popular method is to grow graphene by a chemical vapor deposition (CVD) process. This procedure uses a metal substrate (such as Ni [46, 47], Cu [48, 49], Co [50], Ir [51], SiC [52, 53]) to grow the graphene, which can be transferred to an arbitrary substrate. The process involves a mixture of methane (or similar gaseous carbonaceous source) and hydrogen gases in a furnace of temperatures up to 1000 °C. One major advantage of this method is that with a Cu substrate the majority of the graphene ($> 95\%$) is single layer graphene [48]. Use of other metals, such as Ni, are not self-limiting and can produce bilayer and beyond graphene sheets.

Another method to grow graphene in CVD is to use other solid C sources to grow the monolayer, graphene. This method has used PMMA, fluorine, and sucrose as C sources [54]. The source is placed on a metal substrate (namely Cu), and heated to 800 °C while a reductive gas is flowed through the system. The PMMA source can be doped to readily produce doped graphene layers, the number of layers depending upon the flow rate of the gas. This is an important feature since monolayer graphene does not possess a band gap for semiconductor switching applications [55]. One newly developed method is to remove layers of graphene one at a time [56]. This allows graphene to be adjusted to any desired thickness, as well as to produce reduced layers in specific areas to fabricate devices of varying graphene thickness.

3.4 Transfer

After the graphene has been grown on the base substrate using CVD, it must go through a transfer process to be placed onto an arbitrary substrate. This section will be limited to a description of the transfer process for graphene grown on Cu as was done for this work. Available literature has shown transfer methods for the graphene with minimal tearing and defect creation in the transfer process [57][58][59][60]. Graphene used for this work was purchased from the Graphene Supermarket and was grown using CVD on copper. After purchase, a polymethyl methacrylate (PMMA) layer was drop coated on the graphene-Cu composite and cured. Then, the Cu was etched away using an aqueous solution of 0.05 g/ml ferric nitrate ($\mathrm{Fe(NO_3)_3}$). The dissolution chemistry is as follows:

$$\mathrm{Fe(NO_3)_3} \leftrightarrow \mathrm{Fe^{3+}} + 3\mathrm{NO_3^-} \quad \text{(salt dissolved in water)}, \tag{3.4.1}$$

$$\mathrm{H_20} \leftrightarrow \mathrm{H^+} + \mathrm{OH^-} \quad \text{(water molecules to hydrogen and hydroxyl ions)}, \tag{3.4.2}$$

$$\mathrm{Fe^{3+}} + 3\mathrm{OH^-} \leftrightarrow \mathrm{Fe(OH)_3} \quad \text{(leaves excess H making solution acidic)}, \tag{3.4.3}$$

$$2\mathrm{Fe^{3+}} + \mathrm{Cu} \leftrightarrow 2\mathrm{Fe^{2+}} + \mathrm{Cu^{2+}} \quad \text{(Copper dissolves)}. \tag{3.4.4}$$

After dissolution, the PMMA-graphene composite was rinsed with a DI water bath to remove residual ferric nitrate solution. Then, the graphene-PMMA composite was placed on a substrate.

In this work, the PMMA-graphene was placed either directly on silicon for electron microscope imaging or a silicon nitride (SiN) membrane as a substrate for lithographed nanostructures. Once placed, more PMMA was redeposited and cured by drop coating on top the first PMMA that was placed on the substrate. This step was vital for a good transfer of graphene. Finally, the PMMA was removed using an acetone bath until no residual PMMA was observed leaving the graphene on the new substrate.

Intrinsic graphene transferred to a silicon wafer following the process described in this sec-

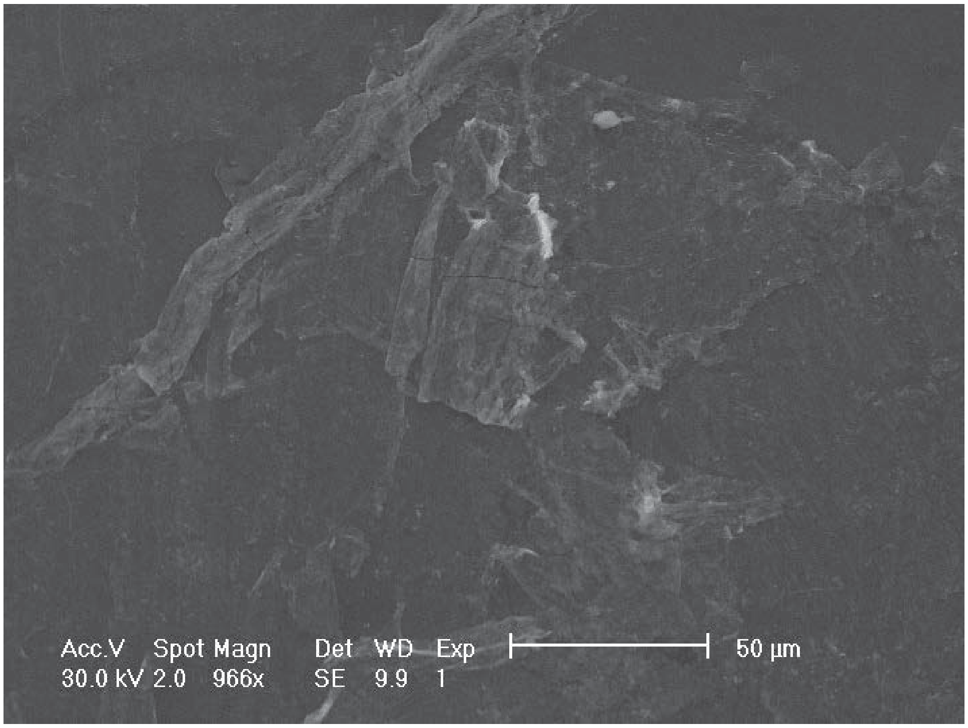

Figure 3.2: Scanning electron micrograph of graphene (brighter contrast) transferred on a silicon wafer.

tion was imaged with scanning electron microscopy (SEM) and is shown in Figure 3.2. While the resolution of the SEM was not sufficient to observe individual atoms in the graphene, there was a clear distinction of where the graphene film was present on the silicon. Large flakes of approximately 500 μm were present throughout the transfer area (data not shown). Fig. 3.2 displays one such flake with some of the transfer defects present. It was observed that some wrinkles, folding, and tearing of the graphene monolayer were present.

To better illustrate some of the observed defects of the transferred, a backscattered micrograph is shown in Figure 3.3. The backscattered electrons were the incident electrons which scattered off the sample back into the chamber. These incident electrons first traveled several nanometers into the substrate before scattering back out. This meant the micrograph displayed information from deeper into the sample which made surface particulates invisible in the micrograph. The figure showed several graphene flakes ranging in size from approximately 50 to 250 μm in size. The center flake showed significant folding and wrinkling with two tears across the

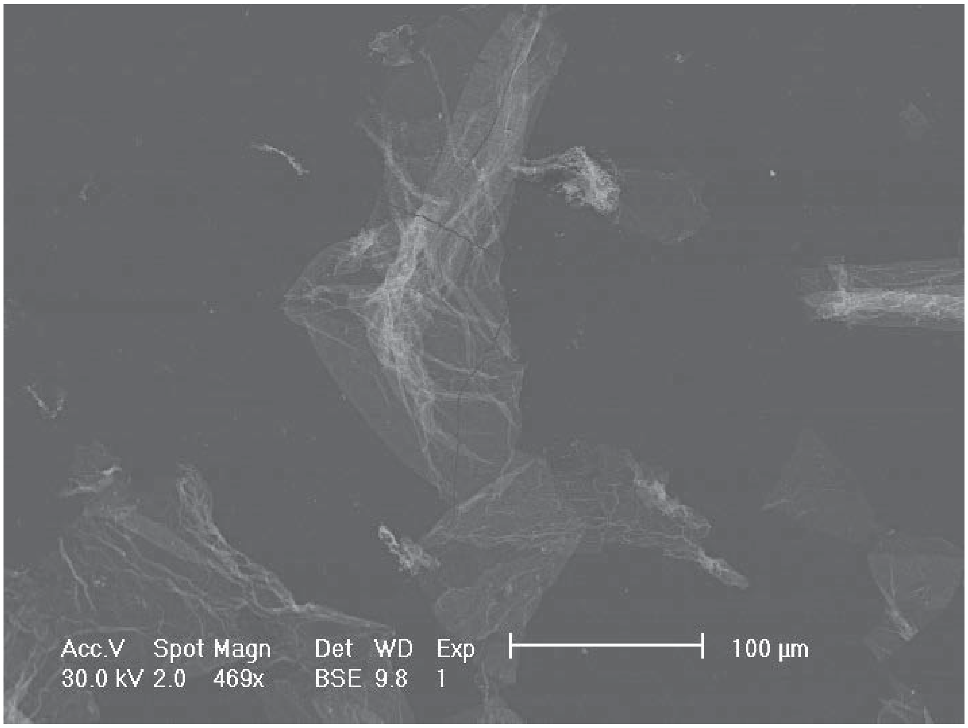

Figure 3.3: Scanning electron micrograph of graphene (brighter contrast) transferred on a silicon wafer.

graphene. This showed successful graphene transfer was performed, but with several defects evident.

The same transfer process was performed on a the 50 nm thick silicon nitride transmission electron microscope (TEM) grid as shown in Figure 3.4. Wrinkling was not as prevalent in this sample, presumably due to the difference in transfer area. Graphene on copper was trimmed down to the approximate 3 mm size of the grid. It was observed that graphene were present over the majority of the sample (data not shown), however, the figure displayed that several tears were present in the transferred graphene. The covered area was sufficient to examine lithographed nanoparticles on graphene in the TEM.

To verify that the observed flakes on the silicon after the transfer process were indeed graphene, the sample was first gold plated using electroless plating. Gold Figures 3.5 and 3.6 show the Au on graphene before and after transfer, respectively. Pre-transferred graphene was decorated with gold nanoparticles by reduction on the graphene surface using a gold tetrachlora aurate (TCA)

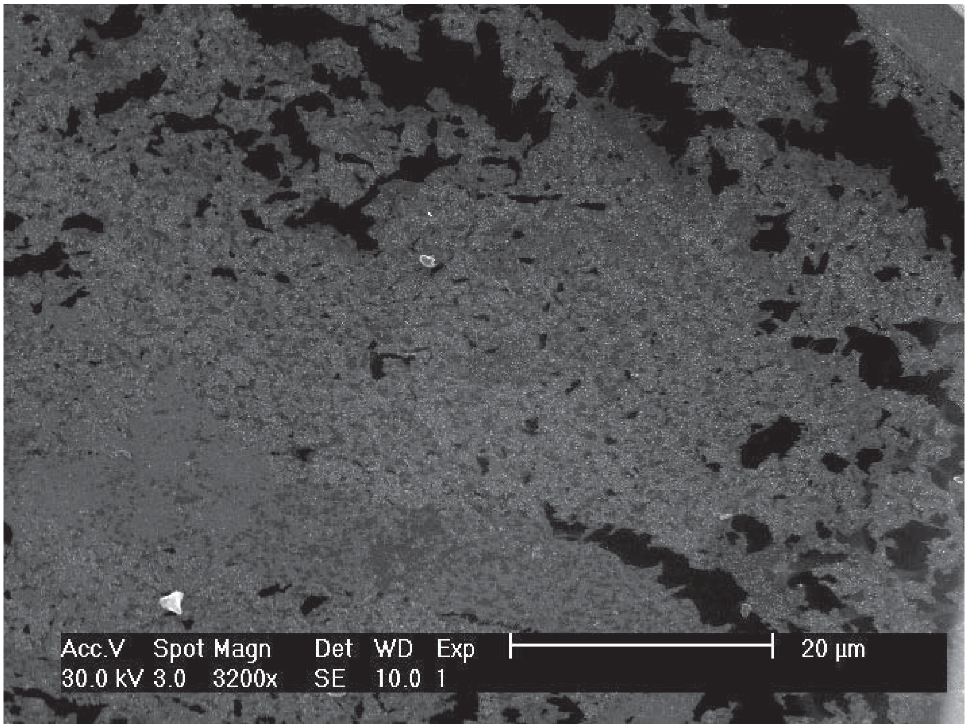

Figure 3.4: Scanning electron micrograph of graphene (brighter contrast) transferred on a 50 nm thick silicon nitride membrane (darker contrast) TEM grid.

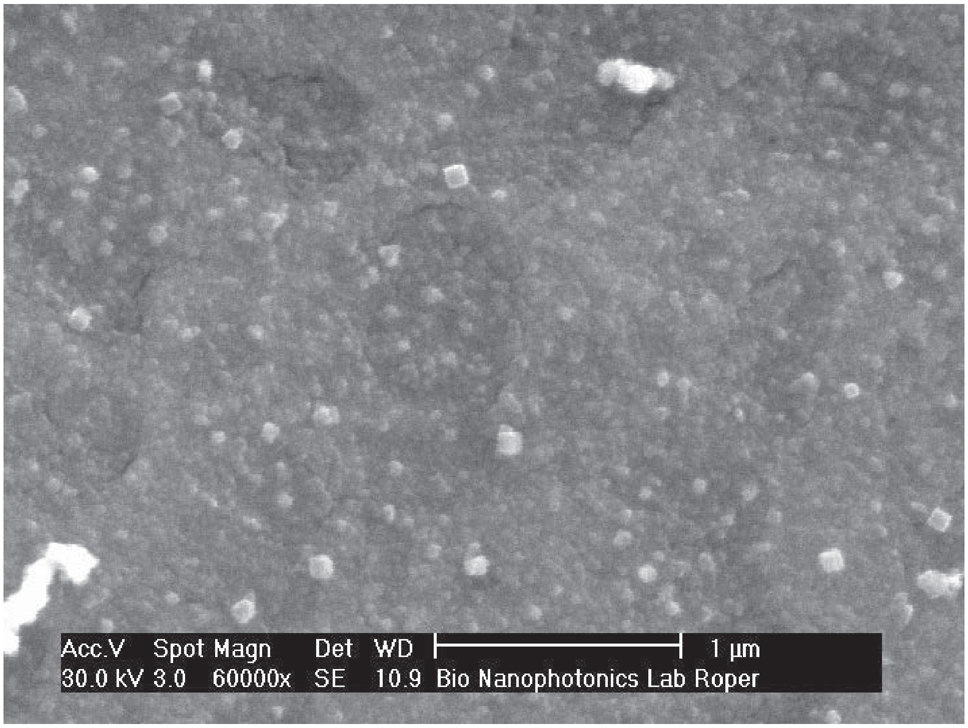

Figure 3.5: Scanning electron micrograph of gold nanoparticles reduced on graphene situated on copper.

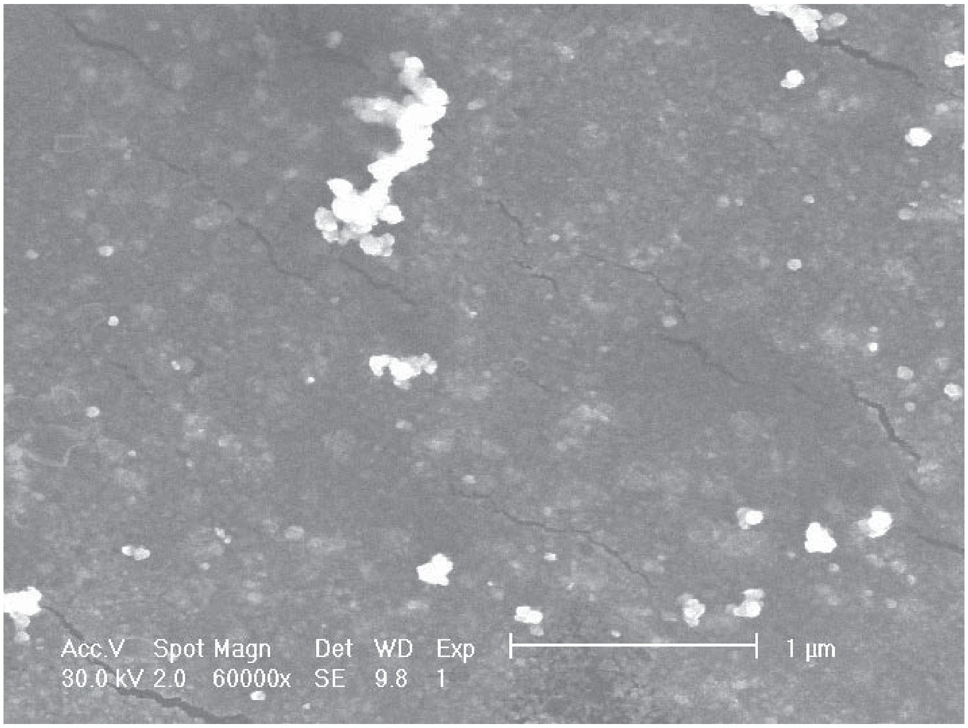

Figure 3.6: Scanning electron micrograph of the same gold-on-graphene composite as Figure 3.5 after transfer of graphene film to silicon.

solution. Graphene-on-copper samples were submersed in a bath of TCA with a gold mass concentration of 1 g/L for 20 seconds. The sample was removed from the TCA bath and was immediately placed in an isopropyl alcohol bath to stop further reduction of residual TCA left on the surface after removal from the bath. The copper foil acted as the reducing agent to create the approximately 30 nm diameter gold nanoparticles on the surface. After the nanoparticle were grown, the transfer process was performed which resulted in transfer of the graphene/nanoparticle composite onto a different substrate, here silicon. The two figures were taken at the same magnification the pre- and post- transferred graphene to show the consistency of the gold nanoparticle morphologies.

It was observed that the transfer process was successful in transferring the graphene with gold nanoparticles on the surface. Before transfer, it was observed that the entire surface of the graphene was decorated in nanoparticles varying in shape from spherical to cubical as shown in Figure 3.5. Also present were conglomerated gold nanostructures of tens to hundreds of smaller nanoparticles such as the one in the bottom left corner of the Figure 3.5. Average nanoparticle size was measured to range from 30 to 50 nm in diameter with the larger sized nanoparticles being the cubical morphologies.

After transfer to the silicon substrate, it was observed that the nanoparticle morphology and distribution were slightly modified. Larger conglomerate nanostructures were still present on the transfer sample as seen in Figure 3.6. However, concentration of smaller, individual nanoparticles decreased. It was presumed this was a result of the weak bond of gold to graphene. Adhesion of the PMMA transfer layer most likely removed some of the gold nanoparticles from the graphene surface.

Chapter 4: Computational Models

This chapter outlines the computational methods used to calculate far-field macroscopic optical properties as well as local microscopic responses of metal nanostructures to incident energy. Incident energies considered included both photon and electron excitation for predicting optical response and electron energy loss. Two primary methods were used in this dissertation to describe these properties. The coupled dipole approximation (CDA) treats each individual nanostructure as a point, polarizable dipole. This approach allows simplification of Maxwell's equations to that of a dipole, which has been solved analytically. Due to the single dipole approximation, this approach is typically only valid for far-field calculations. Similarly, the discrete dipole approximation (DDA) decomposes the volume of an individual nanostructure into a discrete grid of dipoles. The discrete grid must have a dipole separation that is much smaller than the dimensions of the structure. Close proximal locations of the dipoles allows this method to predict near-field properties under both incident photon and electron energies.

4.1 Coupled Dipole Approximation

In the CDA, each nanoparticle is treated as a single, point dipole with a given polarizability. For a set of particles, polarization of the i^{th} particle is proportional to the electric field at that location and is given by

$$\mathbf{P}_i = \alpha_i(\omega)\mathbf{E}_{\text{tot}}(\mathbf{r}_i) \tag{4.1.1}$$

with frequency-dependent proportionality constant defined as polarizability, α, and the total electric field, $\mathbf{E}_{\text{tot}}(\mathbf{r}_i)$, being the sum of the incident field and contributions to all other dipoles in the array. Due to the single-dipole nature of this approximation, near-field interactions are not accurate limiting its validity to particle separations larger than approximately five times the radius [3]. A major discussion of particle polarizability will be discussed in Section 4.2. But first, determination of electric field interactions of the point dipoles will be introduced.

Interactions between plasmonic particles under irradiance can be calculated using this method by summing the dipole radiation from each element in the array. The electric field from a second, j, particle in the set on the i^{th} particle is determined by the equation of a radiating point dipole with [6]

$$\mathbf{E}(\mathbf{r}_{i,j}) = \frac{e^{ikr_{i,j}}}{r_{i,j}^3}\left[(kr_{i,j})^2\left(\hat{\mathbf{r}}_{i,j}\times\mathbf{P}_i\right)\times\hat{\mathbf{r}}_{i,j} + \left[3\hat{\mathbf{r}}_{i,j}\left(\hat{\mathbf{r}}_{i,j}\cdot\mathbf{P}_i\right)-\mathbf{P}_i\right]\left(1-ikr_{i,j}\right)\right] \tag{4.1.2}$$

where $\mathbf{r}_{i,j}$ is the vector pointing from particle i to j and $k = 2\pi\eta/\lambda$ with η the refractive index and λ the vacuum wavelength. The extinction cross section of light extinguished from the array can be calculated using the equation [22, 61],

$$C_{ext} = \frac{4\pi k}{|E_0|^2}\sum_{j=1}^{N}\Im(\mathbf{E}_{\text{inc},j}^{*}\cdot\mathbf{P}_j). \tag{4.1.3}$$

A MATLAB implementation to solve these equations for each particle in a user-defined array by matrix inversion has been written. A finite number of dipole locations is entered and every dipole pair is calculate using superposition to determine the polarization vector, $\mathbf{P}_i$, at each dipole.

A simplification to calculating the electric field contributions from dipoles in the array is to assume an infinite Bravais lattice. This assumption greatly reduces computation and memory requirements since electric field contributions can be calculated once for a ’center’ i^{th} particle and the results are identical for all other particles in the array. Contributions from all other j particles is done by truncation of an infinite sum. This reduces the calculation of Equation 4.1.2 to the retarded dipole sum, S, by [22, 62]

$$S = e^{ikr_{i,j}}\sum_{i\neq j}\left[\frac{(1-ikr_i,j)(3\cos^2\theta_{i,j}-1)}{r_{i,j}^3}+\frac{k^2\sin^2\theta_{i,j}}{r_{i,j}}\right] \tag{4.1.4}$$

where $\theta_{i,j}$ is the angle between the i^{th} and j^{th} particles. Then, extinction cross section from Equation 4.1.3 is similarly reduced to

$$C_{ext} = 4\pi\Im\left(\frac{\alpha}{1-\alpha S}\right). \tag{4.1.5}$$

Utilizing the symmetry of the array, calculation of S can be reduced by summing only over quadrant I. This allows rapid calculation of optical response of nanoparticles to parametric changes of particle size, array spacing, particle composition, dielectric environment. This version of the CDA will henceforth be denoted as the rapid semi-analytic coupled dipole approximation (rsa-CDA).

4.2 Polarizability

Particle polarizability is a measure of the ability of conduction electrons to respond to the incident light. The polarizability for a nanoparticle is dependent on the composition of the particle and surrounding medium as well as the particle morphology. For spheres [63], spheroids [64], and toroids [65] much smaller than the incident wavelength of light, an analytic expression can be found. This expression treats the incident sinusoidal electric field as a rectangular wave and computes the polarizability using an electrostatic approximation. Extensions to this model have been created to account for the finite size effects in a particle. Furthermore, exact expressions have been previously derived for spheres and additional terms have been created to account for higher order electric modes, such as the quadrupole mode.

To start, the quasi static approximation computes polarizability in small particles by treating the incident oscillating electric and magnetic field using electrostatics. For spheres, this gives the expression [63]

$$\alpha_{qs} = R^3 \frac{m^2 - 1}{m^2 + 2} \tag{4.2.1}$$

where R is the particle radius and $m^2 = \epsilon_{\mathrm{Au}}/\epsilon_{\mathrm{medium}}$ is the ratio of dielectric functions inside to outside the nanoparticle. Observing the denominator of Equation 4.2.1, it can be seen that plasmon resonance is only supported on an interface through which the sign of the dielectric function changes signs. This occurs at interfaces such as a metal/dielectric like gold in water or gold in air. The maximum of the Lorentzian resonance profile, denoted as the plasmon wavelength, is where the denominator of Equation 4.2.1 is minimized. This occurs when the real component of m^2 equals -2.The exact value depends on the specific metal in consideration and the medium the particle is embedded in. It is noted that the denominator in Equation 4.2.1 does not contain information about the particle size. This predicts that the plasmon resonance is a fixed value for all particle sizes. However, analytic calculations and experimental results show that a redshifting occurs as particles increase in size. As such, the quasi static approximation is only appropriate for very small particles. For example, this model fails for Au particles as the radius approaches 15 to 20 nm, depending on the embedding medium.

The quasi static approximation has been previously extended to include shape dependence for non-spherical particles. Ellipsoidal particles with smooth surfaces were modeled using the expression [64]

$$\alpha_{qs,l} = \frac{abc}{3}\frac{m^2-1}{1+L_l(m^2-1)} \tag{4.2.2}$$

where L_l is a shape parameter relating damping effects for changes in the particle aspect ratio, a, b, and c are the radii for the x, y, and z axes, respectively, and l denotes the direction of polarization along one of the principle axes of the particle [66]. It is noted that the polarizability is dependent on the polarization of the incident plane wave. Equation 4.2.2 reduces to Equation 4.2.1 when $a = b = c$ giving $L_l = 1/3\ \forall l$.

A special case for Equation 4.2.2 is in the form of oblate spheroids. An oblate spheroid is a sphere that has been squished along the z-axis and is a good approximation for disk shapes typically made with lithographic processes. The size parameter, $L_1 = L_2$, for oblate spheroids with polarization orthogonal to the z-axis is given by [67]

$$L_1 = \frac{g(e)}{2e}\left[\frac{\pi}{2} - tan^{-1}g(e)\right] - \frac{g^2(e)}{2}, \tag{4.2.3}$$

$$e = \left(1-\frac{c^2}{a^2}\right)^{-1/2}, \text{ and } \quad g(e) = \left(\frac{c^2}{a^2-c^2}\right)^{-1/2}. \tag{4.2.4}$$

The term e is the eccentricity of the spheroid and note that $L_1 = L_2$ here. Polarizability for an oblate spheroid is found by insertion of Equations 4.2.3 and 4.2.4 into Equation 4.2.2 for particular a and c values. This model for polarizability will be used in Chapter 5 to characterize effects of particle morphology on plasmon and Fano resonance response.

To account for increasing particle size, the modified long wavelength approximation (MLWA) was previously developed. This modifies the equation for dipole polarization in 4.1.1 to include a radiating term in the electric field [68]. This modifies the polarizability to the form [66, 69]

$$\alpha_{\mathrm{MLWA}} = \frac{1}{(\alpha_{qs,l})^{-1} - \frac{2}{3} i k^3 - \frac{k^2}{R}} \tag{4.2.5}$$

This expression is valid for spheres with radii that limit the particle response to incident light as predominately dipolar in nature. For Au, this limits the MLWA model to particle radii of approximately 80 nm in vacuum. For silver (copper), higher order electric modes appear at smaller (larger) particle radii [3].

An expression for particle polarizability, α, based upon Mie theory has been extended for use in the CDA. An exact dipole polarizability for spherical particles introduced by Doyle [70] was extended to include a quadrupole approximation by treatment of the quadrupolar interactions as dipolar [3]. This expression is given by [19]

$$\alpha_d = \frac{3iR^3}{2x^3} a_1, \qquad \alpha_q = \frac{10iR^3}{3x^3} a_2 \tag{4.2.6}$$

where R is the particle radius, a_i are the Mie coefficients for dipole ($i = 1$) and quadrupole ($i = 2$) modes, and $x = kR$ is a size parameter. Equation 4.2.6 is dependent on the assumption of Mie theory including incident plane wave excitation. Since scattered light propagates in spherical wavefronts, this expression for polarizability is only valid for interacting particles that are spaced at distances greater than approximately five times the radius so that the scattered light can be approximated at planar across the neighboring particle surface. As a result, this model is well suited for far-field interactions described in this dissertation.

Computational methods that use dipole models, such as the coupled and discrete dipole approximations, employ the different polarizability expressions above. For the CDA, single dipole treatment of the particles is best suited for far-field interactions where particle (dipole) separations are larger than particle dimensions. The MLWA or Mie theory formulations are sufficient for the CDA. However, the DDA includes interacting structures with separations that are on the order of or smaller than single entity size separations as well as internal dipoles that are spaced at discretizations of 1 to 10 nm. In this case, more care has to be taken to develop an expression for polarizability that includes effects of close proximal interactions. It is not the intention of this dissertation to review the models for polarizability in DDA. For the interested reader, see the review [71].

4.3 Discrete Dipole Approximation

The discrete dipole approximation is a subset of the volume element method. Instead of a nanoparticle being composed of a single dipole as was the CDA, an individual nanoparticle is broken up into a collection of polarizable dipoles arranged in a cubic lattice. The number of dipoles needed depends on the size of the nanoparticle in relation to the incident wavelength as well as the shape. As a result of the cubic lattice arrangement of the dipole collection, shapes with round or smooth edges require more dipoles. Solving the system of equations for the electric field inside and outside a particle follows the same formalism from the CDA discussed in the previous section. However, the DDA involves dipoles on the order of thousands to tens of thousands for a single entity and requires an increased computational time from a few hours to a few days, depending on the parameters of interest such as wavelength range, particle size, and number of dipoles.

The main difference between the CDA from the previous section and DDA is the expression used for polarizability. The term using Mie theory given in Equation 4.2.6 is insufficient due to the approximations used in Mie theory. For example, Mie theory assumes an incident plane wave. However, the large number of dipoles required for nanoparticles necessitate nanometer to sub-nanometer proximity of dipole locations in the DDA which negates the plane wave assumption.

Discretization of space into a cubic grid allows identification of grid spaces that are to be occupied by a dipole. While increased accuracy is achieved by smaller discretization (i.e. more dipoles), computational time consequently increases. Two DDA implementations will be used in this work. One is the FORTRAN based DDSCAT 7.3 [72, 73, 74] and the other is DDEELS 2.1 [75]. DDA simulations are generally more accurate than CDA, but require much more computation time to perform equivalent simulations. As an example, a single sphere using a point dipole takes seconds to predict optical response in contrast to 80 hours modeling a sphere with 10,000 dipoles. Effects of single structures in layered media (such as graphene) can be assessed with this method as well as coupling of periodic nanoparticle arrangements.

4.3.1 Photon Excitation

Equations for interacting dipoles with incident photon excitation are analogous to the CDA and not repeated here. Simulations with photon excitation were performed using DDSCAT. Input parameters to the open source code include a parameter file with specific choice of polarizability model, target file including the position of all dipoles for the simulation, and source for dielectric values of the metal. This work uses dielectric values from Johnson and Christy [76]. For the target file, a MATLAB program was created to output a file containing dipole locations for disks, ellipses, and rings of user defined dimensions and dipole spacing. For far-field information such as absorption and scattering of incident light, dipole spacings of approximate 5 nm have been shown to be sufficient. However, as a general rule, dipole spacing should be less than approximately one fifth of the particle dimensions and one tenth the wavelength. For near-field calculations, such as local electric fields, smaller discretization of one to three nanometers is needed for converged results.

A typical simulation starts with a discretized structure for far-field simulation of scattering, absorption, and their sum, extinction. The target file is generated for a dipole spacing of three to five nanometers, for which the geometry and plasmon resonance peaks are then calculated. Once the plasmon wavelength is determined for dipole, quadrupole, etc. modes, a new target file is created with the one to three nanometer spacing for the near-field results. The simulation is re-ran at the specific wavelength values of interest to determine to generate local electric field plots at the plasmon resonance locations. The decrease in dipole spacing for the near-field calculation does not cause spectral shifting in the plasmon resonance location since the far-field spectra is already converged [77].

4.3.2 Electron Excitation

Solving the equations for interacting dipoles under electron irradiation has been previously developed with the open source code DDEELS 2.1 [75]. The theoretical description in this section follows the results described in Ref. [75]. An incident electron has an electric field profile that is in stark contrast to on incident photon. Instead of the oscillating electric field, the incident electrons have a time-independent field that is pointed radially inward toward the probe location. Electric fields due to the incident electrons with velocity, v, at specific dipole locations are given by

$$E_{j,x} = \frac{q\omega}{2\pi\epsilon_0 v^2\gamma}\exp\left(i\omega\frac{z_j}{v}\right)\frac{r_x}{r}K_1\left(\frac{\omega r}{\gamma v}\right), \tag{4.3.1}$$

$$E_{j,y} = \frac{q\omega}{2\pi\epsilon_0 v^2\gamma}\exp\left(i\omega\frac{z_j}{v}\right)\frac{r_y}{r}K_1\left(\frac{\omega r}{\gamma v}\right), \tag{4.3.2}$$

$$E_{j,z} = \frac{q\omega}{2\pi\epsilon_0 v^2\gamma}\exp\left(i\omega\frac{z_j}{v}\right)iK_0\left(\frac{\omega r}{\gamma v}\right). \tag{4.3.3}$$

In the above equations, q is the fundamental charge for the electron, v is the electron velocity, ω is the electron radial frequency, impact of the electron beam is denoted $r_i = (x_i, y_i, 0)$, dipole position is $r_j = (x_j, y_j, z_j)$, r is defined by $r = |\mathbf{r_i} - \mathbf{r_j}|$, and $\gamma = \sqrt{1-(v/c)^2}$ is as defined from relativity. Probability of energy loss as a function of ω is given by

$$\Gamma(\omega) = \frac{1}{\pi\hbar^2}\sum_j^N \Im\left(\mathbf{E}_j^* \cdot \mathbf{P}_j\right). \tag{4.3.4}$$

where $\mathbf{P}_j$ is the induced dipole moment for the j^{th} dipole as defined in Equation 4.1.1.

Substrate consideration to account for the SiN membrane has been incorporated in the DDEELS V 2.1 program. While the majority of simulations were performed in vacuum, a select number of simulations were performed with the SiN substrate to determine the overall effect on plasmon resonance. To account for the substrate, the assumption of a semi-infinite model was implemented with the classical image charge technique. The incident, charged electron is mirrored in the substrate with charge q'. Charge for the image is given by

$$q' = \frac{1 - \epsilon_{\text{sub}}}{1 + \epsilon_{\text{sub}}} q, \tag{4.3.5}$$

where ϵ_{sub} is the dielectric function of the substrate. Then, the electric field from the incident electron on a particular dipole is expressed as a superposition of the field from the electron itself as well as its image. Additionally, the total electric field at each dipole is determined as a sum from all other dipoles as with Equation 4.1.2 as well as contributions from the image of each dipole in the substrate. Dipole Polarization vectors for the image dipoles is expressed in a similar fashion to the incident electron image as

$$\mathbf{P}'_j = \frac{1 - \epsilon_{\text{sub}}}{1 + \epsilon_{\text{sub}}} \mathbf{P}_j. \tag{4.3.6}$$

Parameter and target files for the DDEELS is almost identical to the DDSCAT program. Specific inputs, such as incident electron accelerating voltage, polarization model, dipole discretization, and metal dielectric are user defined. Dipole location can be made identical to the DDSCAT program for direct comparison of simulation results for both electron and photon incident energies. Target file generation was done using a MATLAB script similar to the one for DDSCAT. The addition file needed for DDEELS over DDSCAT is a source file defining where the incident electron beam is set. In scanning transmission electron microscopy (STEM), the electron beam is focused to a specific sub-nanometer location. The source file can define a single probe location for obtaining energy loss spectra for varying energy values or a series of locations to obtain a map over the structure at a specific energy loss value. This is similar to the far-field spectra and near-field local field plots calculated using the DDSCAT.

Chapter 5: Far-Field Fano resonance predictions

Nanoparticles organized in a periodic lattice support diffractive coupling resulting in a Fano resonance. This Fano resonance is supported by broadband plasmon oscillation coupled with narrow band diffraction when incident wavelengths match lattice dimensions [78]. Incident wavelength and lattice constant dimensions that produce the Fano resonance have the requirement that wavelength values of the Fano resonance must be greater than the plasmon resonance maxima wavelength [3, 79]. Due to the coupled nature of the Fano resonance, changes to either diffraction or plasmon resonance profiles will shift the energy or amplitude of the resulting Fano resonance. This chapter considers altercations to the embedding medium, lattice dimensions, and particle properties and describes the effect on the predicted Fano resonances.

An example of Fano resonance in a nanoparticle array is shown in Figure 5.1. Single particle extinction of incident light for an 80 nm radius Au nanoparticle using the Mie polarizability model from Equation 4.2.6 (dashed-black) is shown alongside extinction for a 700 nm spaced square lattice of the same particle (solid-red). Excitation wavelengths ranged from 400 to 1,000 nm in increments of 1 nm. The single particle spectra revealed a plasmon peak centered at 560 nm while the lattice displayed a Fano resonance peak at 708 nm. The spectra for the lattice was smoothed using a Savitzky-Golay filter to remove small oscillations for better comparison.

5.1 Refractive Index Effects

The amount of single particle scattering predicted from Mie theory and the computation model in Section 4.2 was observed to be dependent on the medium of the nanoparticles. This change in refractive index modulated the corresponding polarizability of the particles as calculated using Equation 4.2.6. An increase in refractive index caused a redshifting of the polarizability plots of each dielectric material considered. Figure 5.2 displays polarizability plots for an Au nanoparticle with particle radius ranging from 25 to 80 nm and incident wavelengths from 350 to 900 nm, each with 1 nm increments. The color gradient shows the imaginary component of

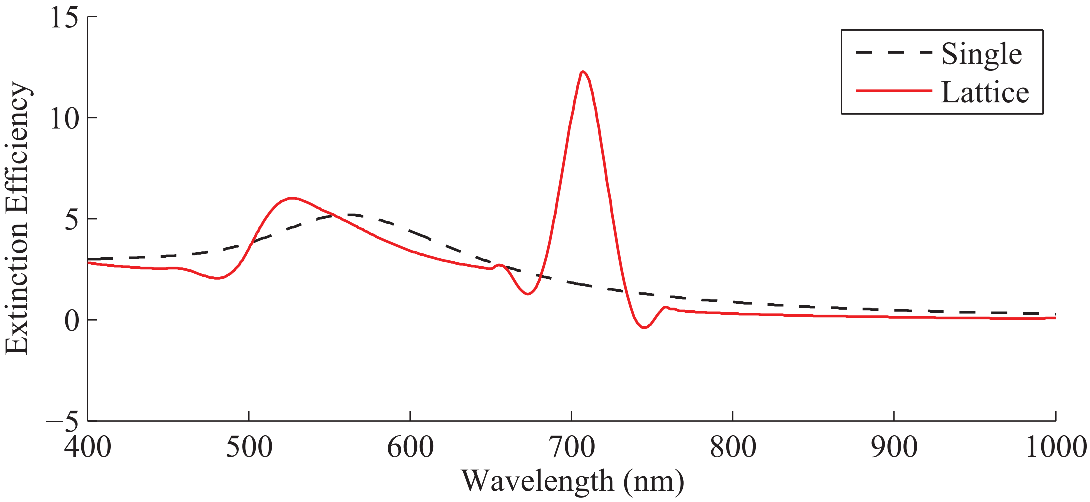

Figure 5.1: Calculated extinction spectra for a single 80 nm radius gold nanoparticle (dashed-black) and a square lattice of 80 nm radius Au nanoparticles with lattice constant 700 nm (solid-red) using the rsa-CDA.

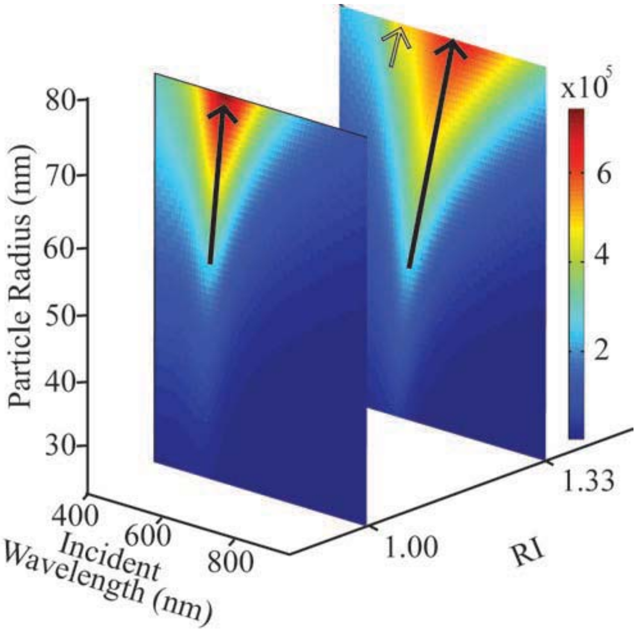

Figure 5.2: Particle Polarizability for an Au nanoparticle with radii from 25 to 80 nm and incident radiation from 400 to 900 nm. The particle is embedded in vacuum (RI=1.00) and water (RI=1.33) for each case. [19]

polarizability which is a function of particle size, incident energy, material dielectric, and medium dielectric (refractive index). The medium RI that the particles were embedded in was set to vacuum (1.00) and water (1.33).

Alterations in the plasmon profile was observed in Figure 5.2 as RI of the embedding media was increased. Plasmon resonance was observed to redshift with higher order electric modes appeared as RI was increased. Plasmon wavelength is the maximum of the shown resonance over the wavelength range for a given particle size. The increased RI redshifted the dipole plasmon mode as well as decreased the limiting radius for particle scattering from 44 to about 35 nm (based upon a maximum polarizability value of 1×10^5). This decrease caused a broadening of the LSPR for a given particle radius as RI increases. Figure 5.2 (b) also shows the quadrupole significance beginning at radii of about 70 nm as opposed to a value of 110 nm as seen for particles embedded in vacuum (data not shown). This is consistent for single particle extinction plots generated by Mie theory (data not shown).

Geometric configurations that produced this extraordinary coupled peak were also affected by the change in local RI. Figure 5.3 displays the 3D plot showing the maximum extinction efficiency for changes in particle radius and lattice constant for various RI values. RI index values used in each simulation were (a) 1.00, (b) 1.05, (c) 1.20, and (e) 1.33. Incident wavelength values used ranged from 400 to 1500 nm in increments of 0.1 nm since the coupled peak was redshifted from the lattice constant by at least $D \times \eta$. The overall diagonal line pattern as seen in the vacuum case remained throughout the increase in RI; however, a narrowing of the parabolas and decreasing particle radius and lattice constant were observed. Note that the range of lattice constants in the x-axis of each plot varied while maintaining a constant scale. The parabola narrowing followed the narrowing tip of the polarizability profile as was seen in Figure 5.2. Furthermore, the minimum particle separation and radius for coupling to occur decreased as RI was increased. This is illistrated in Figure 5.4 for the minimum radius and lattice constant to give a Fano resonance with magnitude of 50 from Figure 5.3. This was caused by the redshift in the LSPR being less than that of the coupled dipole peak. Chapter 6 discusses this shift in detail. Since the coupled dipole

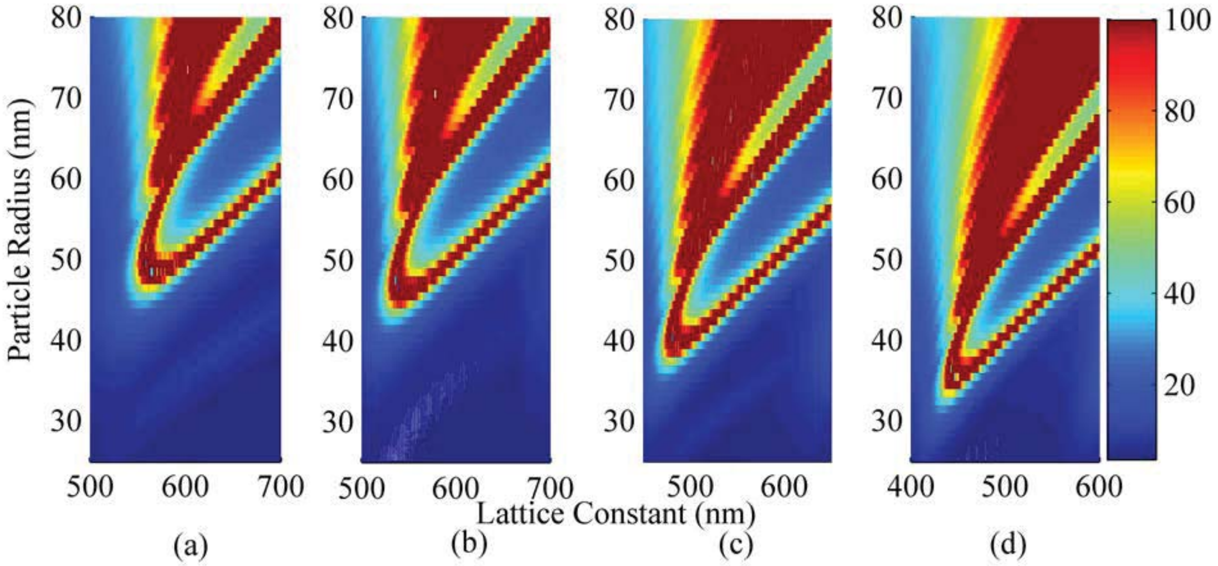

Figure 5.3: 3D plot showing maximum extinction amplitude for a given lattice constant and particle radius for RI values of (a) 1.00, (b) 1.05, (c) 1.20, and (d) 1.33.

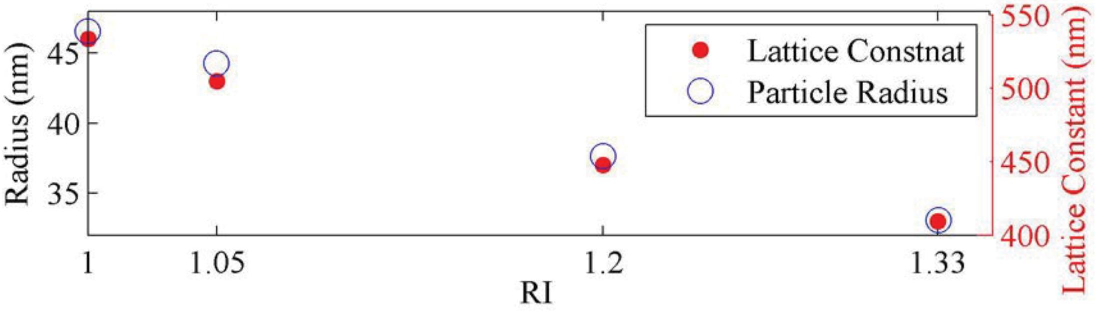

Figure 5.4: Miniumum particle radius (open blue) and lattice constant (closed red) required for Fano resonance as extracted from Figure 5.3.

peak had a greater shift, lower particle spacing were used to obtain a coupled peak in the envelope produced by the individual particle polarizability.

Periodic diagonal lines of isometric values of particle polarizability from the parabola legs were still present when the RI surrounding the particles changed. However, they became less distinct as RI increased. Evaluation of the polarizability value of the lowest diagonal line was done in each environment to determine the effect of RI changes. Polarizability values for the higher diagonal lines can be determined; however, this became difficult as the lines began to blur. Increasing the environment RI surrounding the particles caused the isometric polarizability value

Table 5.1: Polarizability values for diagonal lines in each dielectric, eccentricity, and refractive index changes. All values are to the order of 10^5.

	Zero	First	Second	Third
Au	–	.575±.0541	1.32±.0867	1.92±.0540
Cu	–	.582±.0392	1.41±.0687	1.97±.0422
Ag	.226±.0164	.566±.0468	.974±.0547	1.28±.0863
OAD	–	1.15±.0973	–	2.62±.0800
Au_{MLWA}	–	.588±.0393	1.36±.0732	1.99±.0543

Eccentricity	0	.5	.75	.9
First Diagonal Line	.588±.0393	.592±.0437	.605±.0458	.621±.0219

Refractive Index	1.05	1.10	1.20	1.33
First Diagonal Line	.427±.176	.412±.0372	.383±.0653	.335±.145

for the lowest diagonal line to decrease. Redshifting of the Fano peak location with increasing RI was greater than the redshifting of the LSPR. Uneven shifting of the two peaks gave the decrease in polarizability values. These values and their standard deviation are in the second break of Table 5.1. In general, the standard deviations for the increased RI values were larger than those in vacuum. This was most likely due to the difficulty in evaluating which lattice constant is responsible for the largest peak amplitude. Periodic interruptions made it difficult to consistently choose values along the diagonal line. This inconsistency and line broadening were the apparent reasons for the increased standard deviation.

To evaluate the effects of contributions from different particle modes, the rsa-CDA performed the simulation considering only axial and off axial/diagonal (OAD) particles. Figure 5.5 shows the 3D plot similar to that of Figure 5.3; however, a single RI value of 1.00 was used. Figure 5.5 shows contributions from (a) all, (b) only OAD, and (c) axial particle contributions. From the figure, it was seen that the parabolic shapes when all particles were considered were a result of destructive interference from OAD particles. When only axial particles were considered, no parabolic shapes appeared. However, inclusion of OAD particles created a gap in the lattice geometries that allowed Fano resonance to occur. Reasons for the parabolic line shapes will be explained by examining a simplified model examined in the next section.

Results of the 3D plot were compared to that of the single particle polarizability model,

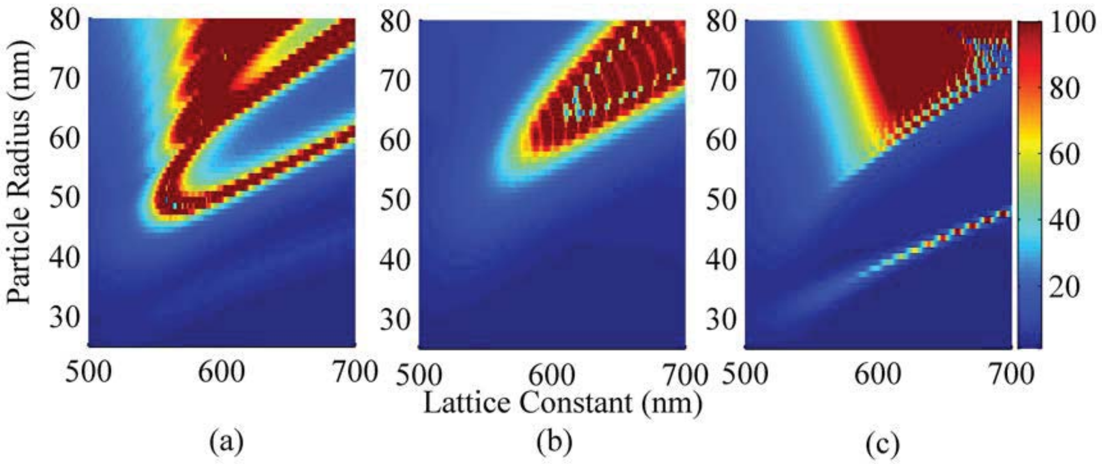

(a) (b) (c)

Figure 5.5: 3D plot showing maximum extinction value for a given array configuration from (a) all, (b) off axial/diagonal (OAD), and (c) axial contributions.

α_{Mie}. Figure 5.6 (a) displays the single particle Mie polarizability for a single homogeneous RI of 1.33 with particle radii from 25 to 80 nm and incident light from 450 to 900 nm. The x-axis of Figure 5.6 (b) shows values of the lattice constant. However, since wavelength contraction has occurred, the Fano resonance appeared at a value of the lattice constant multiplied by the RI of 1.33. Since it has been observed in this dissertation that the coupled peak only occurred in the envelope of large single particle polarizability, the actual location of the coupled peak was more important than the actual lattice constant itself. Notice that the limiting lattice constant for an extraordinary coupled peak (extinction > 50) always gave a coupled peak that was redshifted from the loci of maximum of single particle polarizability, consistent with similar results from the literature [3]. Furthermore, the limiting radius for which the coupled peak occurred decreased from the vacuum case. Consistent with previous results (Section 5.1), a maximum polarizability value for a given particle radius below 10^5 cannot scatter enough light to cause the far-field coupling, as observed in this dissertation. The corresponding limiting radius value of 34 nm was found. Increases in the RI allow smaller particles to possess a larger polarizability leading to the decreasing particle radius limit.

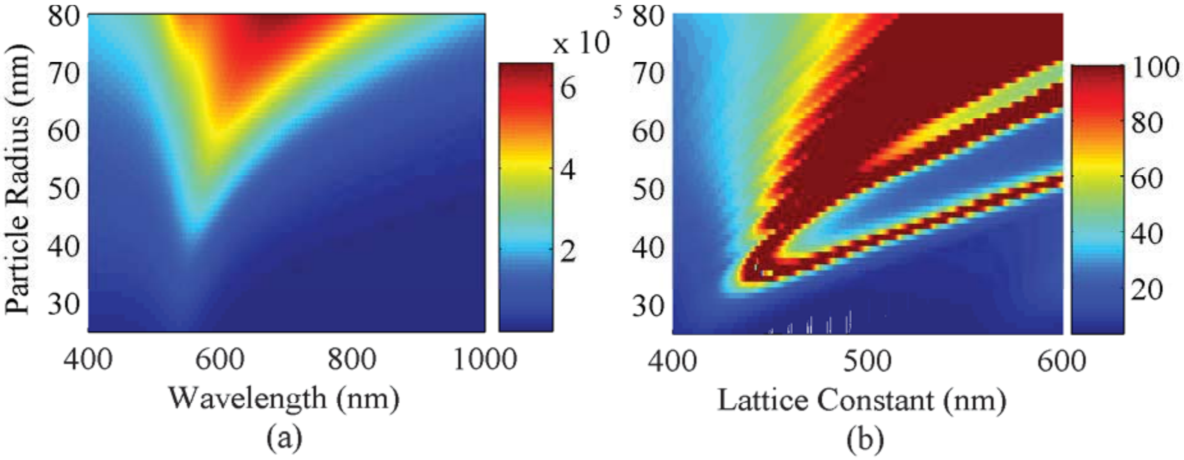

Figure 5.6: (a) Single particle Mie polarizability and (b) square array of particles embedded in water (RI=1.33).

5.2 Phase Overlap

A simplified look at the phase overlap of neighboring particles can help explain not only the periodic interruptions with change in refractive index, but also the isometric polarizability lines. Consider a one dimensional linear chain of Au particles separated at a distance greater than the plasmon wavelength so that the coupled Fano resonance can occur. Separations are consistent so that the nearest neighbor of the center particle is separated by D, the next by $2D$, and so on. For simplicity, assume that the coupled peak location occurs at exactly the particle separation ($\lambda = D$), ignoring the observed redshifting due to coupling. Phase overlap from an arbitrary particle to the center particle is given by e^{ikr}, where $k = 2\pi\eta/\lambda$ is the wavenumber, η is the medium RI, λ is the vacuum wavelength, and r is the separation from the source of the pulse. Retardation effects are ignored since the excitation is orthogonal to the chain and each dipole oscillates at the same rate. Phase overlap from the elements in the chain on the center particle is given by [79]

$$2\sum_{n=1}^{N} \exp\left(i\frac{2\pi\eta}{D}nD\right) = 2\sum_{n=1}^{N} e^{i2n\pi\eta}, \tag{5.2.1}$$

where $2N+1$ is the number of particles in the chain. Note, this illustration assumes each dipole radiates as a plane wave and ignores the amplitude decrease.

Evaluation of Equation 5.2.1 requires knowing the value of the refractive index. In vacuum, the sum is straightforward since $e^{i2n\pi} = 1 \; \forall n$. Therefore, the sum is simply equal to $2N$. However, this becomes complicated when RI increases. Phase amplitude is derived from the real component of Equation 5.2.1, so only consideration of the cosine term is shown here. Invoking Lagrange's trigonometric identity,

$$\sum_{n=1}^{N} \cos nx = \frac{1}{2}\left[\frac{\sin[(N+1/2)x]}{\sin(x/2)} - 1\right], \tag{5.2.2}$$

the real component of the phase overlap can be expressed as

$$2\mathrm{Re}\left(\sum_{n=1}^{N} e^{i2n\pi\eta}\right) = 2\sum_{n=1}^{N} \cos(2n\pi\eta) = \frac{\sin[(2N+1)\pi\eta]}{\sin(\pi\eta)} - 1. \tag{5.2.3}$$

Using the example of $\eta = 1.1$, the phase overlap becomes modular. There are six values that the sum can take, depending on the value of N. That is to say $N \in \mathbb{Z}_5$ uniquely gives all the possible answers to the phase overlap. These values in ascending numerical order are -4.236, -3.3618, -2, 0, 1,618 and 2.236. See the inset of Figure 5.7. Depending on the number of particles in the sum, the contributions from all particles can be constructive or destructive. In the vacuum case, all particles interacted constructively with the center particle. When the RI is increased, the phase overlap has periods of constructive and destructive interference. Adding retardation and attenuation effects gives the retarded dipole sum used to calculate extinction in the CDA formalism. Even this simple example shows how refractive index effects can cause periodic interruptions in the intensity of the coupled peek seen in Figure 5.3.

Small changes in wavelength (or RI) can have a profound impact on a single geometric configuration. To account for distance dependence of the radiative fields, the cosine term in the sum can be multiplied by $1/n$. This normalizes the distance between particles and includes the radiative field behavior of r^{-1}. An analytic expression does not exist for this sum, but its numeric computation in a loop is straightforward. When this term is included in the sum, the phase overlap converges to a specific value. The value of convergence can be either positive or negative giving constructive or destructive net interference. As refractive index increases, small changes in lattice

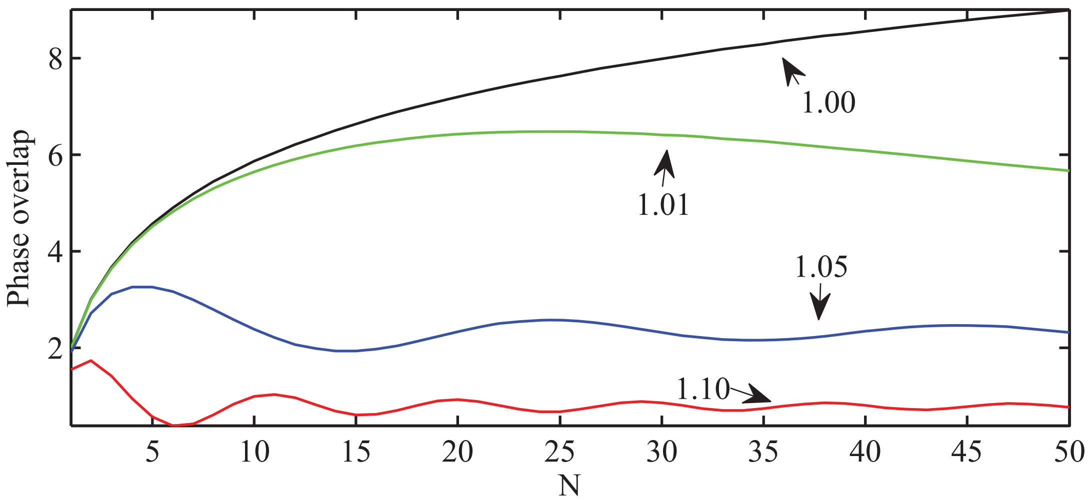

Figure 5.7: Phase overlap for the distant dependent sum of elements in a chain for RI values of 1.00 (black), 1.01 (green), 1.05 (blue), and 1.10 (red). Inset shows non-distant dependent phase overlap for RI of 1.05, 1.10, and 1.33 (purple).

constant gives changes in wavelength of $D\eta$. This increased wavelength change is reflected in the greater periodicity in the interruptions seem with increasing RI values in Figure 5.7.

Figure 5.7 displays the sum of the phase from a chain of NPs. RI values of 1.00 (black), 1.01 (green), 1.05 (blue), and1.10 (red) show how the changing RI can affect the amount of constructive interference on the center particle by a chain of $2N$+1 particles. In the inset, non-distance dependent contributions are shown to show the effect of RI change on the phase of scattered light, even for small changes.

Consideration of the isometric polarizability values uses the same formalism, but with a slight modification. Instead of considering small changes in refractive index, consider non-axial rays added to the solution. Now, the real component of the phase overlap from an arbitrary ray is

$$2\mathrm{Re}\left[\sum_{n=1}^{N}\exp\left(i2n\pi\sqrt{j^2+k^2}\right)\right] = 2\sum_{n=1}^{N}\cos\left(2n\pi\sqrt{j^2+k^2}\right) \tag{5.2.4}$$

$$= \frac{\sin\left[(2N+1)\pi\sqrt{j^2+k^2}\right]}{\sin\left(\pi\sqrt{j^2+k^2}\right)} - 1 \tag{5.2.5}$$

where j and k respectively indicate the x and y integer multiple of the lattice constant the nearest neighbor of the ray is from the ‘center’ particle. Again, this sum is periodic with N. Interpreting this result with the isometric polarizability values requires considering the decay of the scattered light from each node. As particle radius is increased, particles have increased scattering which implies that the scattered light can travel a greater distance before it becomes negligible. As such, increasing particle radius effectively increases the number of particles (N) in the sum from Equation 5.2.5. This also explains why the density of diagonal lines increases as particle radius increases. Consider concentric circles emanating from the ‘center’ particle that go through neighboring particles. The further the circles are from the center, the closer together they become. This allows a sup-linear increase in the number of particles chains that contribute to phase overlap of scattered light on the center particle.

In this work, consideration of phase overlap as a function of incident wavelength revealed spectral oscillations from lattice geometry. Calculated phase overlap from a square lattice of perfect dipoles with a lattice constant of 700 nm is shown in Figure 5.8 (a) for truncated grid sizes of 50, 100 and 150 particles corresponding to arrays of 101x101, 201x201, and 301x301 particles. Oscillations in the phase overlap were observed to be a function of the grid size. Increases in the grid size gave corresponding increases in the frequency of spectral oscillations. To explain this, Figure 5.8 (b) shows phase overlap from particular chains in the lattice for the grid size of 100. Chains are labeled in the figure to correspond to the x and y position of the nearest neighbor to the center particle. Each unique chain shown in the inset gave a peak in the phase overlap in the window of incident wavelengths. For increasing grid size, the number of elements in a given chain as well as the number of unique chains in the lattice increase giving the more frequent oscillations were shown.

5.3 Trends From the Modified Long Wavelength Approximation

5.3.1 Spherical Particles

Analysis for amplitude modulation based upon particle polarizability was performed for the modified long wavelength (MLWA) polarizability model. The analysis was done for the same

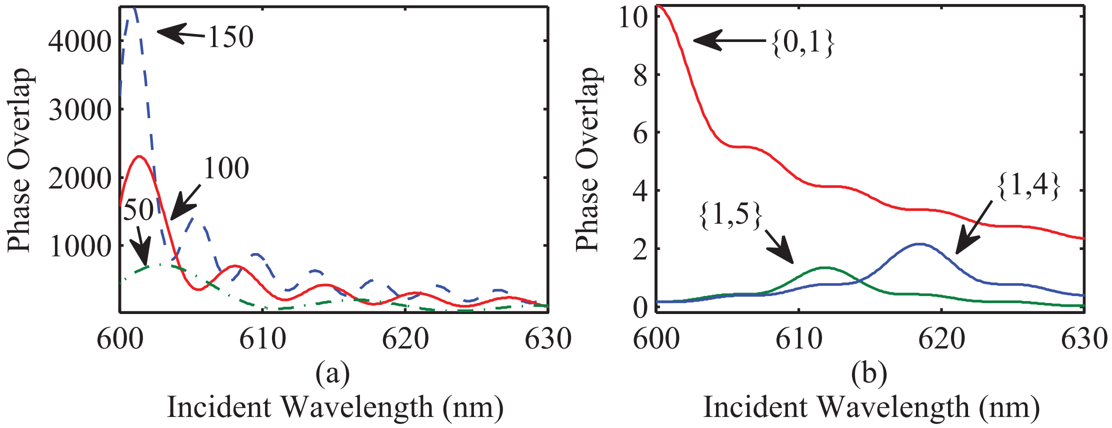

Figure 5.8: Phase overlap for the distant dependent sum of elements in a (a) square lattice of 600 nm as a function of wavelength with varying grid size of 50, 100, and 150. Shown in (b) is phase overlap of specific chains in the lattice. Adapted from [79].

conditions as Figure 5.3 (a). It was seen that the same trends of isometric polarizability values were seen for this model but for slightly different values of polarizability. These values were consistent with the hypothesis that greater and lesser LSPR values would yield average greater and lesser isometric values of polarizability for the diagonal lines in the plot for peak amplitude with varying lattice constant and particle radius. Limiting lattice constant for coupling to occur were observed to be redshifted from the LSPR maximum, as seen previously using α_{Mie}.

Amplitude variation of the coupled peak for various lattice constants and particle radii are shown alongside single particle polarizability in Figure 5.9. In (b), red-colored parabolas indicated lattice dimensions that allowed constructive interference to create amplified electric fields around the particles. Each parabola in (b) had legs that followed a diagonal line with increasing slope with lattice constant. The patterns for the diagonal lines were very similar to those of the Mie polarizability model shown previously in Figure 5.3 (a). However, there were two differences between them. First, the meshpoints through which the diagonal lines of high extinction were not exactly the same for the two polarizability models, especially for larger particle sizes. This was due to the varying values for the polarizability model. The first diagonal line in both figures had a similar shape, but was shifted to smaller radii for the MLWA model. This shift depended on the particle size, 2 nm for a 570 nm spacing and 3 nm for a 740 nm spacing. The second diagonal

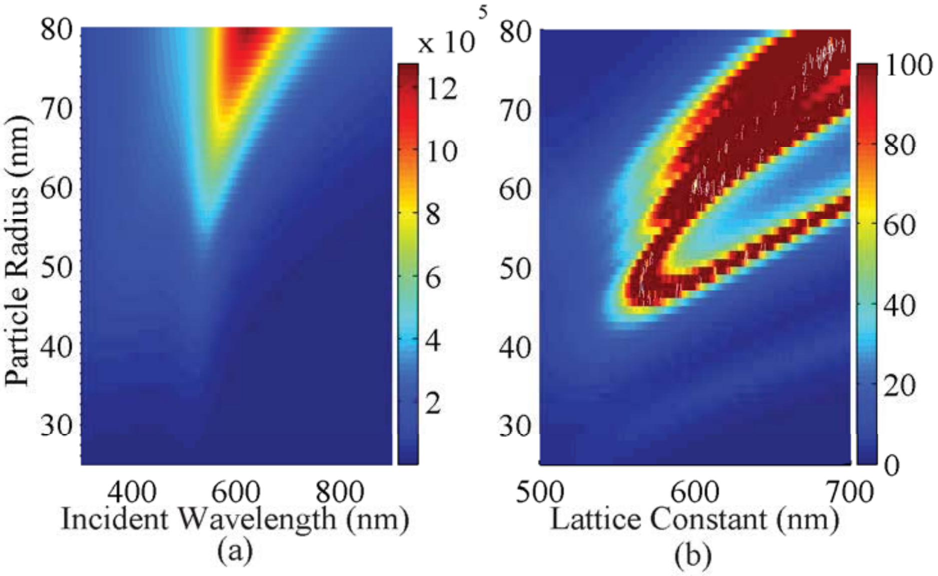

Figure 5.9: Displays (a) Imaginary component for particle polarizability values using the Modified Long Wavelength Approximation, α_{MLWA} from Equation 4.2.5 and (b) extinction amplitude values of the range of incident wavelengths of 300-900 nm for varying particle radius and lattice constant. Each meshpoint is a different array geometry with varying lattice constant and particle radius.

line followed a similar shift ($\sim$3 nm). Above this point, the diagonal lines started to lose their 1:1 correspondence.

Mie and MLWA polarizability models gave varying distributions for the constructive coupling between nanoparticles with radii larger than $\sim$ 60 nm in a infinite array. The Mie polarizability model gave eight isometric polarizability values (four discernable) from the legs of the observed parabolic line shapes that allowed for constructive coupling to occur. The MLWA model blurred isometric values together to produce the same eight diagonal lines, but only two were discernible. This is attributed to the fact that the polarizability values for the MLWA in Figure 5.9 (a) indicated a more broad LSPR peak for these particles sizes as compared to the Mie model. This spreading out of the polarizability values decreased the distance between isometric polarizability causing the said blurring to occur.

Furthermore, minimum lattice constant for a given diagonal line increased more rapidly for the MLWA as particle size increases. This was consistent with the observation that the LSPR redshifts more for the MLWA at larger particle sizes as compared to the Mie model. This increased shift was also consistent with the hypothesis that the coupling between scattered photons and plasmons required a smaller frequency for the scattered light than the LSPR for individual particles. As the LSPR redshifted, so did the required particle separation to achieve coupling between particles. Next, the MLWA model was used to explore the effect of particle shape on the active regions where constructive coupling is allowed.

5.3.2 Oblate Spheroids

Lithographically prepared particles are shaped like cylinders before the annealing process. Even after annealing, the shape could be oblate with the semi-minor axis in the z direction. To account for this, the polarizability for oblate spheroids was used in the rsa-CDA. Simulations were performed for various levels of eccentricity for both single particles and infinite arrays. For reference, the Equations for polarizability are 4.2.2 and 4.2.3 and for eccentricity, Equation 4.2.4. Eccentricity values used for the plots in Figure 5.10 were e = 0.5, 0.75, and 0.9. Comparison with the spherical particle (e = 0) and oblate spheroids with the given eccentricity values for a semi-major axis of 65 nm showed that the increase in e decreased the magnitude of the LSPR peak. A slight blueshift was seen for e increasing to 0.75, which quickly started to redshift for e = 0.9. Even larger eccentricity values approached a flat disk and yielded an LSPR that was redshifted by several hundred nanometers (data not shown). These same eccentricity values were used in calculating the maximum extinction efficiency for a large set of parameter changes.

Geometric configurations that allowed constructive coupling between diffracted photons and the particle plasmons for oblate spheroids was similar to that of perfect spheres using the Mie polarizability. Figure 5.11 shows the value of maximum extinction for incident wavelengths from 400 to 900 nm in 0.1 nm increments using lattice constants ranging from 500 to 750 nm and particle radii from 25 to 80 nm. As eccentricity was increased, the limiting lattice constant and particle radius both increased. For example, using a peak amplitude of 50, the smallest particle radius and lattice constant combination to support the Fano resonance was found to be 44 nm radii spaced at 555 nm in (a) and 48 nm radii spaced at 564 nm in (d). Limiting radii and lattice constants for each

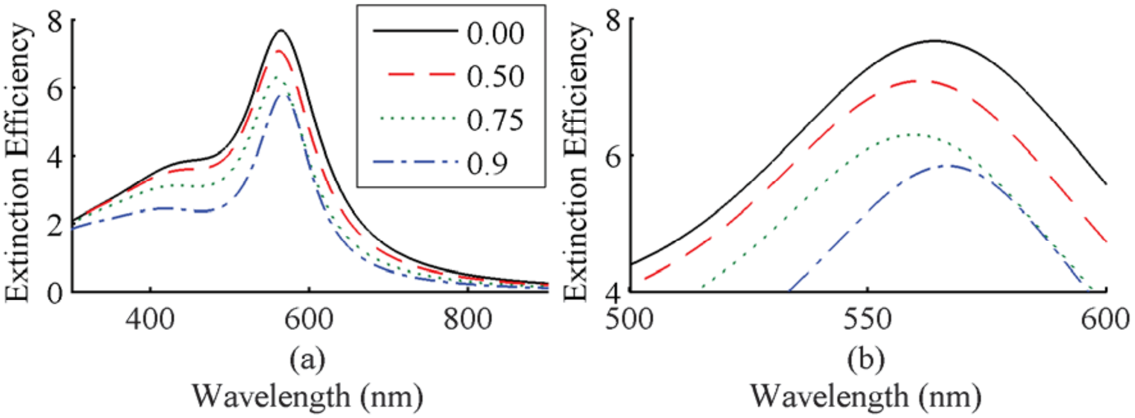

Figure 5.10: Displays (a) the extinction efficienct for a single particle with radius 65 nm using the MLWA polarizability with eccentricity values of 0, 0.5, 0.75, and 0.9. In (b), the same data are shown with a smaller windoe range in wavelength and extinction.

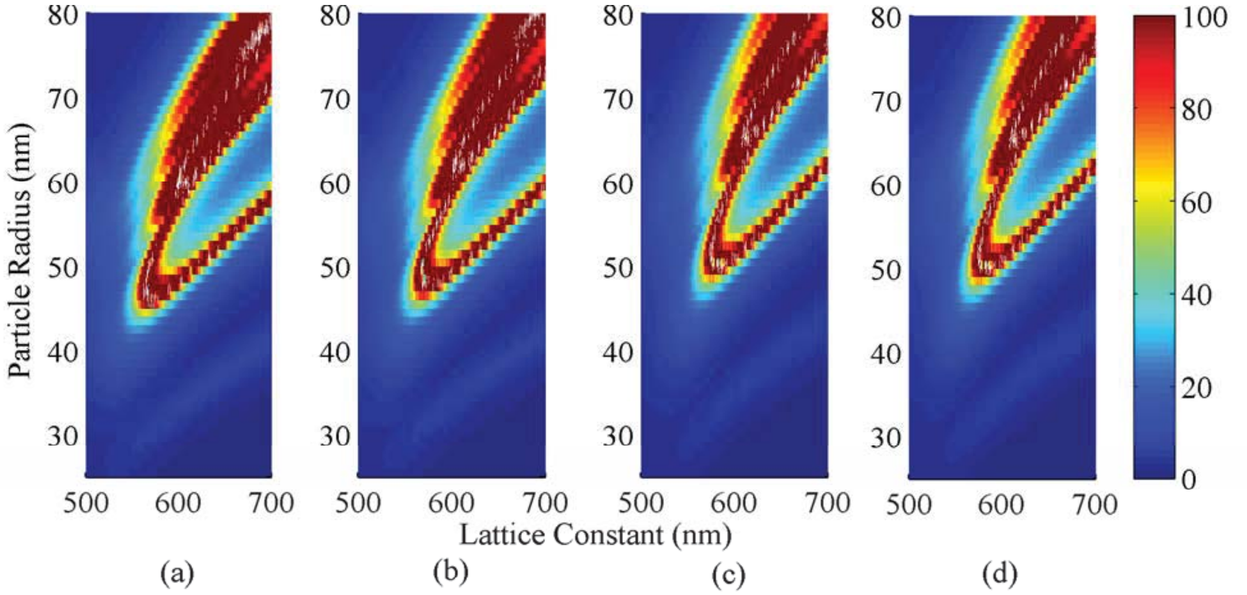

Figure 5.11: Displays the maximum extinction efficiency for a given lattice geometry using the MLWA polarizability with eccentricity values of (a) 0, (b) 0.5, (c) 0.75, and (d) 0.9.

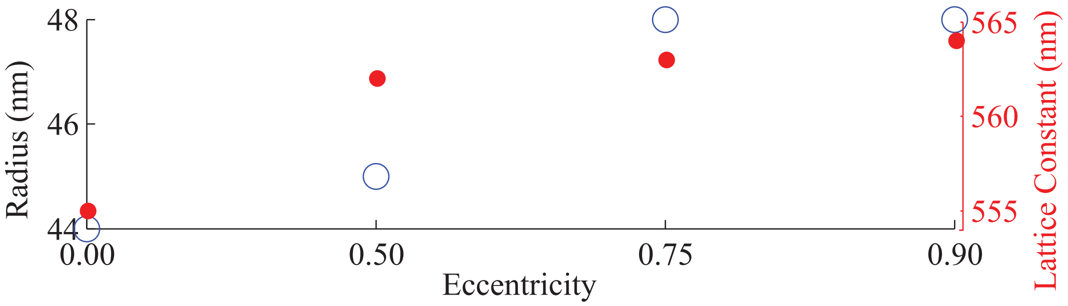

Figure 5.12: Miniumum particle radius (open blue) and lattice constant (closed red) required for Fano resonance as extracted from Figure 5.3

case is illustrated in Figure 5.12. This is consistent with a redshifting polarizability for increased eccentricity. These results are compared against the single particle polarizability plots.

Particle polarizability plots for each eccentricity value is shown in Figure 5.13. Each plot shows the imaginary component of α_{MLWA} for the oblate spheroid of eccentricity (a) 0.0, (b) 0.5, (c) 0.75, and (d) 0.9. Significantly, the value of maximum extinction decreased as eccentricity increased as indicated by the scale bar in each plot. This was consistent with the decrease in LSPR amplitude seen in Figure 5.10. Furthermore, the LSPR resonant wavelength for a 50 nm semi-major axis increased from 533 nm for the (a) to 546 nm in (d). Contrarily, the LSPR resonant wavelength for an 80 nm semi-major axis decreased from 623 nm in (a) to 600 nm in (d). This is translated to Figure 5.11 (a) and (d). Comparison of Figure 5.11 (a) and (d) show that the limiting lattice constant for 50 (80) nm semi-major axis is increased (decreased) as eccentricity went from 0 to 0.9.

It has been shown in this chapter that the behavior of the Fano resonance was consistent independent of the polarizability model used. Peak location only occurred at values that were larger than the single particle LSP wavelength as indicated by comparison of the imaginary component of the particle polarizability with the 3D plot, indicating geometric configurations that allowed constructive coupling to occur. Furthermore, location of the peak was always redshifted from the lattice constant times the refractive index due to coupling effects of the diffracted light and the single particle LSPR. Consideration of specific lattice constants and particle radii that allowed constructive coupling to occur indicated that specific isometric values of particle polarizability

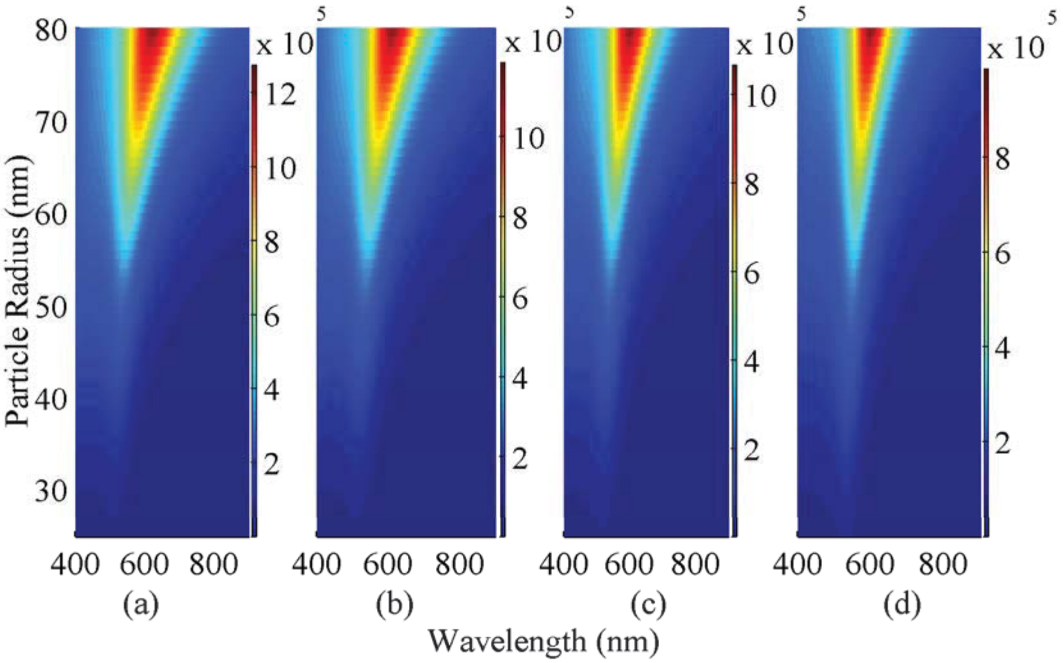

Figure 5.13: Displays the single particle polarizability values of the imaginary component of the MLWA polarizability with eccentricity values of (a) 0, (b) 0.5, (c) 0.75, and (d) 0.9.

yielded the coupled peak. The following chapter uses these results to consider this physical setup as a sensing platform.

Chapter 6: Sensing

6.1 Plasmonic Sensors

Detection of biological molecules is improved by use of plasmon based sensors. These sensors come in the form of propagating surface plasmon-polaritons (SPP) [10, 12, 80, 81, 82] or localized surface plasmon resonance (LSPR) [10, 62, 80, 83, 84, 85] with plasmon excitation from electromagnetic (EM) radiation. Each sensor type has different advantages and disadvantages, but one defining consideration is sensitivity. Sensitivity measures a sensor's ability to detect some analyte. Increased sensitivity for sensors allows the detection smaller quantities of some analyte or the ability to have much smaller systems.

Ability to detect analytes using plasmonic sensors is a result of the modifiable optical properties of the particles. As was seen in Section 5.1, plasmon resonance detectably redshifted as medium refractive index was increased. Additionally, nanoparticles arranged in a lattice supporting Fano resonance were observed to exhibit a redshifting resonance with increased RI. This redshift is two-fold. First, modulated polarizability with changing RI caused shifts in Fano resonance location. Additionally, wavelength contraction within the embedding media scaled the Fano resonance linearly with RI. This section will assess the comparative resonance shifting of plasmon resonance in single particles and Fano resonance in periodic lattices.

A quantitative assessment for sensitivity can be done to compare sensors of different types. Effects of changes in local refractive index (RI), instrument sensitivity, field of view, and active plasmonic area are taken into effect by

$$F = \Delta\lambda_{max}\Delta\eta_m^{-1}A_{xc}^{-1}N_{NP}^{-1}A \tag{6.1.1}$$

where A is the field of view area, N_{NP} is the number of particles contained in A, A_{xc} is the cross sectional area of an individual particle, $\Delta\eta_m$ is the local change in RI, and $\Delta\lambda_{max}$ is the change in resonant peak location [86]. F gives the sensitivity of the array while taking the amount of

Au covering the surface and equipment considerations into account. This dissertation chapter was focused on the theoretical understanding that a simple determination of sensitivity was the change in peak location per change in refractive index unit (RIU).

Surface plasmon sensors have been well characterized and are used widely in the industry. They are generally a thin film of plasmonic material (mostly Au for biological purposes) fabricated on a dielectric substrate. The SPP is excited by collimated broadband light and reflection is measured [87]. Introduction of an antibody allows bonding of some analyte to the sensor surface changing the local RI of the gold film which modifies the propagation wavelength of the SPP. This effect can be spectroscopically measured do determine the presence of the analyte. A Kretschmann geometry is often used to excite the SPP. This involves sending incident light through a prism on the Au surface [88]. Other methods of excitation include gratings, optical fibers, and waveguides [89]. Sensors of this type have been used to assess amounts of specific bacteria in drinking water [87], detect food borne pathogens [90], and analyzing the activity of HIV-1 integrate [91]. SPP sensors are limited by dimension of the sensing probe which requires fluid on the order of microliters to be used as where LSPR sensors are reduce this to the order of nanoliters [62, 92].

Localized surface plasmon sensors work in a similar nature to SPP sensors but use nanoparticles instead of thin films. The plasmon resonance wavelength of the nanoparticles depends on shape, size, proximity, composition, and arrangement [3, 66, 93, 94, 95]. These parameters can be changed to modulate the LSP wavelength to various values in the visible range. For this reason, Au nanoparticles suspended in solution give a reddish tint, depending on particle size and concentration. The LSP is typically excited by orthogonal incident EM radiation [3], but fiber optic excitation has also been demonstrated [92]. Transmission spectra is taken to determine the peak shift when the analyte is introduced in to system, which changes the local RI around the nanoapricles [84]. LSP sensors have been successfully used to detect the biomarker for Alzheimer's [84], brain cell activity [85], and DNA [62].

Specific particle arrangements have been used for different cases. Random assemblies of nanoparticles allow collective coupling of particles based upon their separation to adjust the

LSPR location, λ_{max}. However, a higher level of EM extinction through coherent coupling can be achieved through ordered arrays, including hexagonal (for rotational symmetry) [84], square [3, 62], and others such as dimers [96]. In particular, square arrays of nanoparticles have been well characterized and produce an extraordinary coupled peak caused by the coupling of scattered EM radiation of neighboring particles with the LSP of other particles [3]. To assess the sensitivity of this coupled peak to changes in local RI, an effective RI model was used.

6.2 Model for Refractive Index Surrounding Particles

Sensing using the two-dimensional (2D) square nanoparticle arrays have an increased sensitivity over LSPR based sensors. This increased sensitivity is due to the spectral response of the coupled diffraction peak that occurs at values near the lattice constant times the refractive index of the media. Formalism of the simulations performed in this dissertation (see Chapter 4 for details) assumed a homogeneous background. In reality, the fabricated array has particles that were located at an interface between two different materials. For optical transmission experiments, the arrays were situated on an indium tin oxide (ITO) coated glass slide. There were different models to account for this difference, however, the one best suited for the rapid semi-analytic coupled dipole approximation (rsa-CDA) was termed the effective refractive index (EFI) model.

The EFI model (described in [97]) replaces the inhomogeneous media with a homogeneous one with an RI that is averaged based upon the thickness of a given RI layer. In particular, this ERI is expressed by

$$\eta_{\text{eff}} = \begin{cases} \frac{1}{2}[\eta_1 + \frac{h}{\lambda}\eta_2 + (1 - \frac{h}{\lambda})\eta_3], & h \leq \lambda \\ \frac{1}{2}(\eta_1 + \eta_2), & h > \lambda \end{cases} \tag{6.2.1}$$

where η_i is the i^{th} media and h is the thickness of the second, sandwich media. In the case of the ordered on ITO coated glass, $i = 1$ is the background media that is changed by the experimenters, $i = 2$ is the ITO, and $i = 3$ is the substrate on which the particles reside. Figure 6.1 shows the nanoparticle array sitting on the ITO covered substrate. Each medium, $\eta_{1,2,3}$, are shown in the figure. For the purposes of this work, the substrate ($i = 3$) used wavelength dependent RI

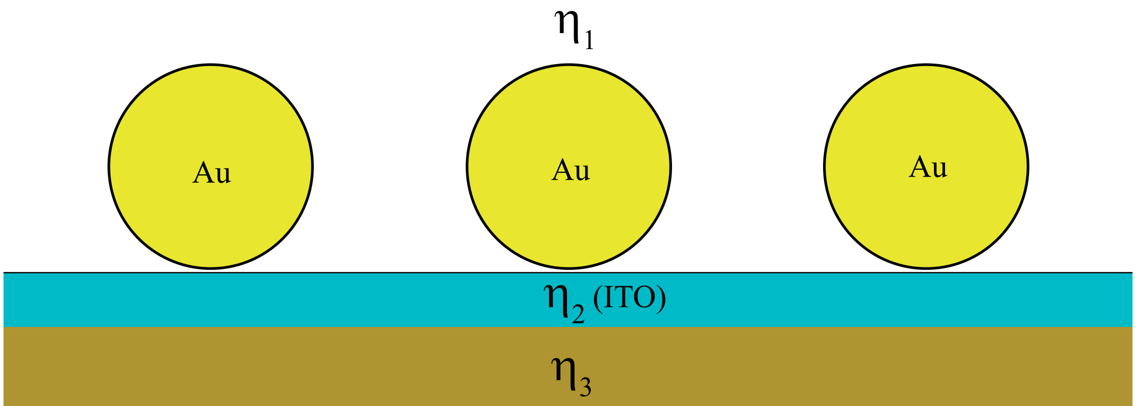

Figure 6.1: Array of Au nanoparticles sitting on an ITO covered substrate.

Table 6.1: Effective RI values

η_1	1.00	1.10	1.20	1.30	1.33
η_{eff}	1.28	1.33	1.38	1.43	1.44

values for silicon dioxide ($Si0_2$) as published in the Handbook of Optics [98]. The middle layer in this case is indium tin oxide (ITO) which has a complex valued RI obtained from the SOPRA database [99]. Plots for changes in the media RI were obtained by adjusting the RI values of the top layer ($i = 1$). Values for the media used ranged from vacuum (1.00) to that of water (1.33). The effective RI, η_{eff}, was calculated and used in the rsa-CDA which allowed the results to fall in other's experimental regimes.

The RI values for SiO_2 are plotted in Figure 6.2. SiO_2 only has a real component. In the incident wavelengths of interest, the RI of SiO_2 was relatively constant, decreasing nearly linearly from 1.549 at 500 nm and 1.535 at 1000 nm. ITO refractive index used a static value of 1.90 since it ws essentially constant throughout the wavelengths of interest. Values for the effective refractive index for the background media with varying RI values of 1.00, 1.10, 1.20, 1.30, and 1.33 are given in Table 6.1. Since the substrate refractive index is wavelength dependent, a single wavelength value of 600 nm was used to calculate the values of η_{eff} in the table.

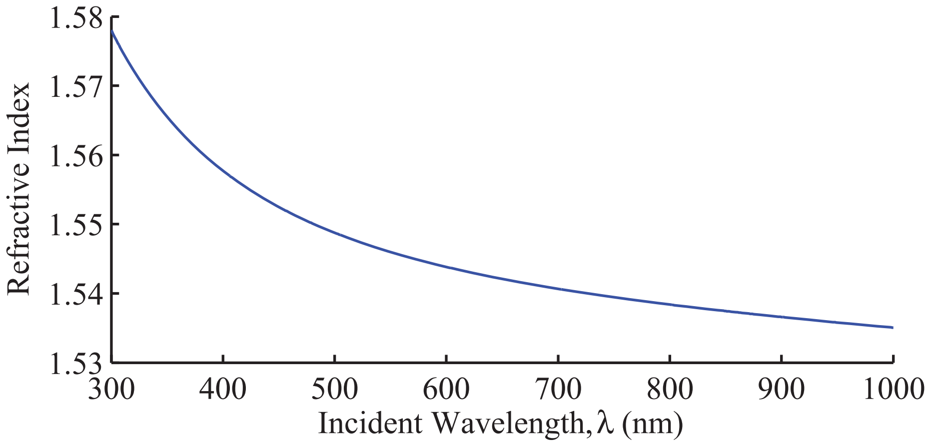

Figure 6.2: Wavelength dependent refractive index values for SiO_2.

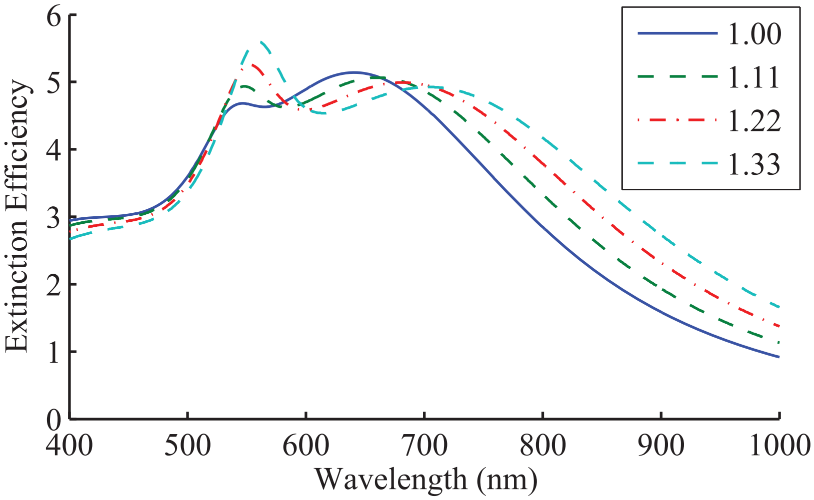

Figure 6.3: Plots single particle extinction spectra for an 80 nm radius particle using the effective RI model. Background RI values are indicated in the figure.

6.3 Array Sensitivity to Refractive Index Changes

6.3.1 Peak Location

This model for refractive index as described in the previous section was used in the rsa-CDA to generate results of changes in the peak location with respect to changes in RI. Simulations were run to determine the value of peak shift when the background medium refractive index, η_3, changes. Figure 6.3 displays the localized surface plasmon resonance (LSPR) peak for a single Au particle of 80 nm radius surrounded by the homogeneous medium with RI of η_{eff}. Values for

Table 6.2: Single Particle LSPR Peak Features

η_1	Mode	Peak Location (nm)	Peak Width (nm)	Peak Amplitude	Ratio
1.00	Quadrupole	546	-	4.681	0
	Dipole	641	83	5.141	0
1.11	Quadrupole	548	27	4.936	.07
	Dipole	660	85	5.066	.22
1.22	Quadrupole	553	33	5.254	.21
	Dipole	682	91	4.926	.45
1.33	Quadrupole	560	38	5.600	.37
	Dipole	704	97	4.926	.65

the background RI (η_1) were 1.00 (solid), 1.11 (dash), 1.22 (dot), and 1.33 (dash-dot). There were two distinct peaks in each spectra: Quadrupole and dipole. Both the quadrupole and dipole peaks redshifted as the background RI was increased. The quadrupole mode became more dominant and increased in amplitude while the dipole mode slightly decreased in amplitude. The quadrupole peak was maximum at 546 nm for vacuum background RI and increased to 560 nm for that of water (1.33). Similarly, the dipole peak shifted from 641 nm to 704 nm as background RI changed from vacuum to water. Significantly, the plasmon resonance range also increased for larger background RI values. The tail end of the dipole peak broadened to larger wavelengths (from ~800-950 nm) while the front of the quadrupole peak remained relatively constant at ~500 nm. This implied that a larger range of lattice constants induce a significant coupled dipole peak in the square array. The values of peak shift and amplitude variation for each refractive index can be found in Table 6.2. Peak location, width, and amplitude for various background RI values are shown in Table 6.2 in order to evaluate the individual particle's ability to detect changes in the environment surrounding it. The 'Peak Width' column is the peak's full width at half max (FWHM) and the 'Ratio' column is the ratio of the shift in peak location to its FWHM. Spectra for the quadrupole peak with $\eta_1 = 1.00$ was too small to yield a significant FWHM. This gave a simple comparison in the sensitivity between different physical setups [93]. Shifting calculations were performed using η_1=1.00 as the reference peak. FWHM calculations used the minimum of the dip between the quadrupole and dipole peaks.

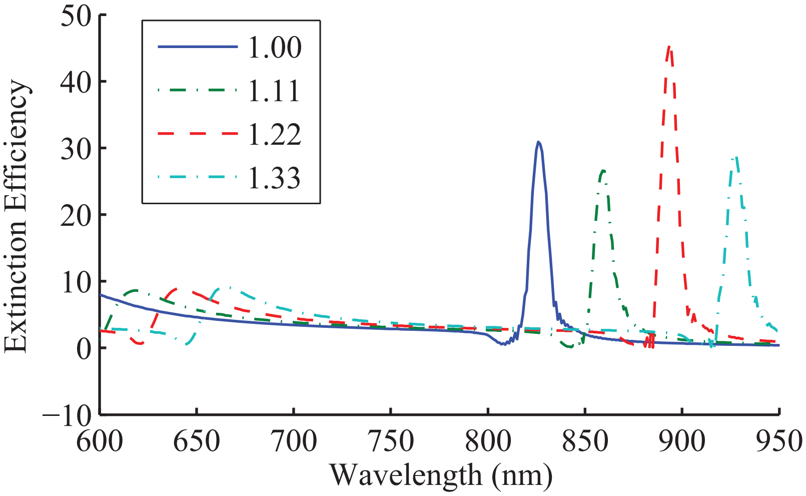

Figure 6.4: Extinction spectra for an infinite square array of 80 nm radius particles with a lattice constant of 630 nm for various background RI index values.

Figure 6.4 shows the coupled dipole peak of an array of 80 nm radius particles arranged in a square lattice with lattice constant of 630 nm. The same background RI values were used as in the single particle case, 1.00 (solid), 1.11 (dash), 1.22 (dot), and 1.33 (dash-dot). Locations of each coupled peak occurred near values of the lattice constant multiplied by the effective RI. As an example, the peak location of the 1.00 background RI gave an effective RI of 1.28. Multiplying this value with the lattice constant of 630 nm gave a value of 806.4 nm which was about 20 nm less than peak location at 826 nm. However, Figure 6.4 did indicate a drop in extinction to ∼0 just prior to the coupled peak. This drop in extinction occurred at an incident wavelength of 806 nm. This fact, along with the redshift of the coupled peak location from this divergence point was consistent with results previous works in the literature [3]. Table 6.3 gives values of the coupled dipole peak width and location for each background RI change. Column descriptions in Table 6.3 are the same as Table 6.2. In addition, the column 'η_{eff} @ Peak Location' gives the effective refractive index at the value of the coupled peak. Since the substrate RI was wavelength dependent, a single wavelength was chosen. It was also interesting to note that the peak amplitude was periodic with changing RI, which was consistent with results from Section 5.1.

Using the 'Ratio' column of Tables 6.2 and 6.3, a comparison of the sensitivities between the two systems was done. The smallest RI change was used in the comparison to improve consis-

Table 6.3: Array's Coupled Dipole Peak Features

η_1	η_{eff} @ Peak Location	Peak Location (nm)	Peak Width (nm)	Peak Amplitude	Ratio
1.00	1.27	826	9	30.91	0
1.11	1.33	859	9	26.58	3.67
1.22	1.38	894	9	46.12	7.56
1.33	1.44	927	10	29.25	10.10

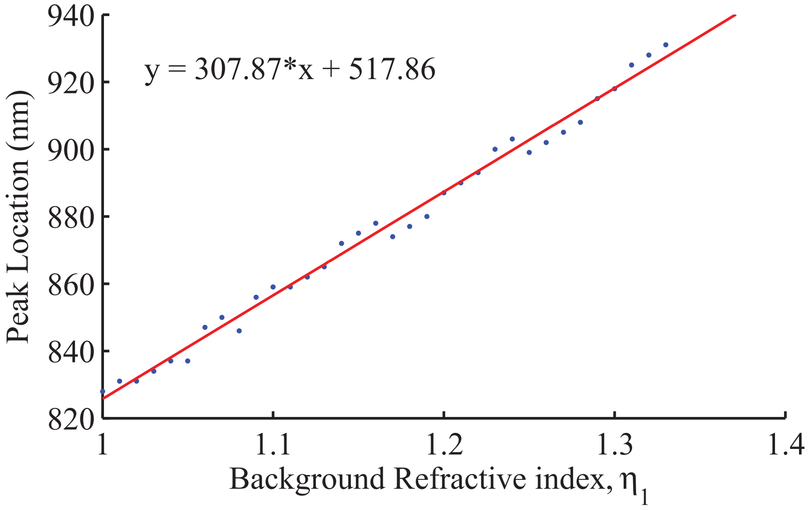

Figure 6.5: Coupled dipole peak location for an infinite square array of 80 nm radius particles with a lattice constant of 630 nm with varying background RI.

tency with real physical sensing platforms. Single particle data gave quadrupole and dipole peaks that shifted with the change in background RI from 1.00 to 1.11. Ratios of peak shift to FWHM for the quadrupole and dipole peaks were 0.07 and 0.22 respectively. Here, the dipole peak, though more broad, gave a higher sensitivity for detecting RI changes at this particular particle radius. The square array yielded a ratio of 3.76 for the same background RI change. This produced an increase in the sensitivity by nearly 17 times that of the single particle dipole peak. In general, this implies that periodic nanostructured platforms which produce a diffraction peak have a high sensitivity than those based upon the LSPR.

Simulations were run at smaller RI increments to determine the array's sensitivity to such changes. Figure 6.5 displays the change of the coupled peak location with respect to background RI. Background RI was used as the independent variable as opposed to the effective RI since the only variable the experimenter could change with regard to RI is the background (unless of course one chose a different substrate). Several RI values were used in the simulation to more accurately determine trends in the peak location. Background RI values varied from 1.00 to 1.33 by increments of 0.01. Dots in the Figure indicate simulated results of peak location at each background RI and the line is the linear fit with its equation indicated in the Figure. Sensitivity was determined by a measure of the slope of the RI vs. Peak location plot. Here, the slope was found to be 307.9 nm/RIU. Periodic changes from the dots being above and below the line were consistent with the results of Section 5.2. Data were collected from un-smoothed plots which contained oscillations due to contributions from off axial/diagonal (OAD) particles. Near the peak maximum, these oscillations changed slightly in magnitude which shifted the peak wavelength between oscillations. However, the shift was only by a few nanometers.

Sensitivity given in Figure 6.5 was less than comparable geometries. For example, a periodic structure of close packed chains gave values of 966.7 nm/RIU [100]. However, the sensitivity used in that case was calculated from a straight RI rather than the background RI as used in this chapter. Furthermore, a larger spacing was used in [100], which led to larger shifts. Using the same RI model and lattice constant of 1000 nm, the infinite square array for 80 nm radius particles gave a sensitivity of 848.5 nm/RIU (data not shown). Though not done here, this can be maximized for particle radius and lattice constant. The disadvantage to using such large spacings is the peak amplitude is reduced by more than 50% in many cases. Furthermore, real physical systems have a substrate, so the effective RI model is a better approximation of experimental sensitivities.

Particle polarizability was generated with the inclusion of the substrate using the effective RI. Figure 6.6 shows the polarizabilities for Au particles of radii 25 to 80 nm and incident wavelengths from 400 to 1000 nm. Background RI values used in the effective RI model were (a) 1.00 and (b) 1.33. In both cases, the dipole resonance was dominant. Furthermore, the quadrupole mode became important at larger particle sizes, especially for the 1.33 RI case. Figure 6.6 shows the quadrupole mode at approximately 550 nm in (a) and 562 nm in (b). Redshifting of the dipole peak also occurred from 569 nm in (a) to 599 in (b) using a 50 nm radius. Minimum particle radius

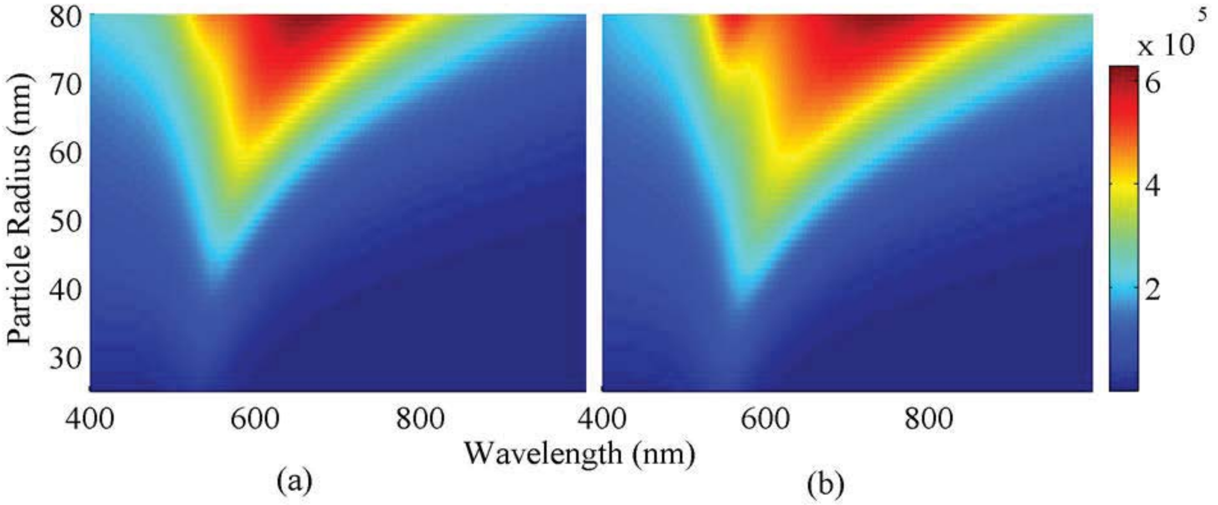

Figure 6.6: Single particle polarizability for Au using the effective RI model with background RI values of (a) 1.00 and (b) 1.33.

for coupling to occur (polarizability of 10^5) drops from 35 nm in (a) to 32 in (b). Polarizability plots gave insight to the coupling of particles in the array as discussed in Section 6.3.2.

Specific particle sizes and spacings led to a higher extinction peak and thus have applications for higher sensitivity. Figure 6.7 shows a surface plot of the infinite array with changing particle radius and lattice constant using the η_{eff} for the medium the particles were embedded in with a background RI of 1.00. Particle radii ranged from 25 to 80 nm and the lattice constant varied from 400 to 700 nm. As before, maximum extinction efficiency was truncated at 100. Similar to Section 5.1, the minimum value for lattice constant was below the LSRP since the peak location was shifted to a value near the lattice constant times the RI. Diagonal lines following the contour of polarizability (Figure 6.6 (a)) were seen in the Figure, consistent with the results of Chapter 5.

6.3.2 Intensity Changes

Another way to calculate sensitivity is the change in intensity of the spectra at a given wavelength. This was advantageous for a narrow high intensity peak as seen with the coupled dipole peak in square arrays of nanoparticles. Figure 6.8 shows spectra for a small change (0.05) in background RI for (a) a single particle and (b) an infinite array. The particle size and separation were the same as in the previous section (80 nm radius and 630 nm spacing). Background RI

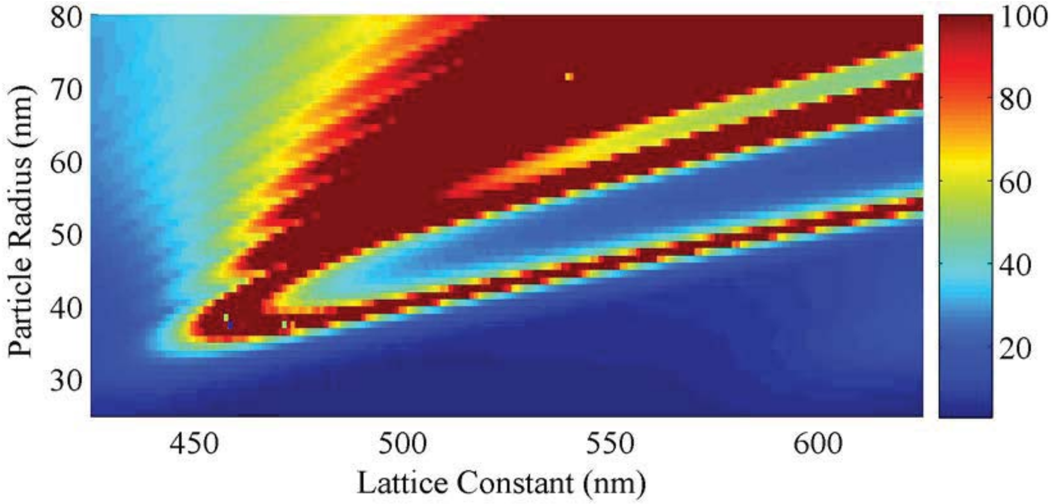

Figure 6.7: 3D plot showing the maximum value of extinction efficiency for a given array using the effective RI model and the background RI of 1.00.

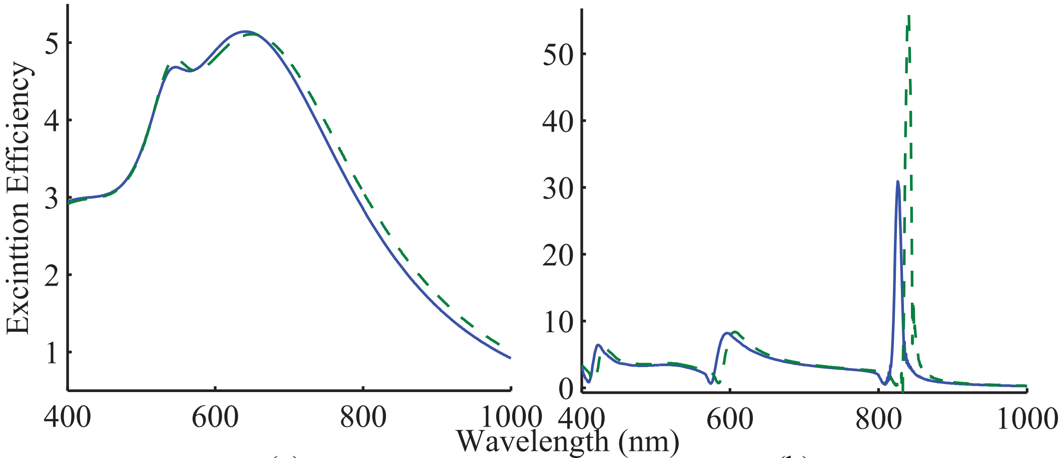

(a)

(b)

Figure 6.8: Extinction efficiency for (a) single particle and (b) infinite square array using background RI values of 1.00 and 1.05. An 80 nm particle radius for both and a 630 nm lattice constant for the array were used.

Table 6.4: Single Particle LSPR and Infinite Array Peak Features

η_3	Mode	Peak Location (nm)	Peak Width (nm)	Peak Amplitude	Peak Amplitude @ RI=1.00
1.00	Quadrupole	546	-	4.68	-
	Dipole	641	83	5.14	-
1.05	Quadrupole	546	21	4.79	4.79
	Dipole	651	83	5.11	5.10
1.00	Coupled Peak	826	9	30.91	-
1.05	Coupled Peak	840	8	56.22	0.45

values were changed from 1.00 (solid) to 1.05 (dash). From the figure, it was apparent that the single particle extinction for each quadrupole and dipole peaks had only minor changes. In fact, the quadrupole peak occurred at the same wavelength for each RI value. Contrary to that, the array's coupled dipole peak had a comparably larger shift in location as well as a much larger drop in extinction amplitude. Table 6.4 shows values for peak location, FWHM, and amplitude as in the previous section's tables. In addition, the last column of Table 6.4 gives the extinction amplitude of the increased background RI at the wavelength where RI=1.00 was a maximum. This gave the change in peak intensity at a given wavelength as the background RI increases. The table is broken horizontally into two sections. The top section shows the single particle case and the bottom section shows the infinite array.

The infinite array gave a much larger drop in intensity compared to the single particle case. This intensity drop gave an overall greater sensitivity of ordered arrays using the coupled peak. The extinction efficiency dropped from 30.91 to 0.45 as the background RI changed from 1.00 to 1.05. This equated to a decrease of 30.46 or 98.5% of the peak. The single particle case had a drop of 0.05 in dipole extinction or 1% of the peak, which is easily lost in the noise of the equipment. The large drop in extinction of the array was due to both the larger shift in peak location and smaller FWHM as compared to the plasmon peaks.

6.4 Nanoring Particles

Limited plasmon resonance windows for spheroidal nanoparticles necessitated more complex shapes with more control and expansive plasmon wavelengths. Plasmon resonance of spheroidal particles with primarily dipolar resonance were predicted in Chapter 5 to be limited to approximately 540 to 650 nm. Further redshifted resonances were able to be achieved, but with quadrupolar activity present and particle dimensions larger than 200 nm. To overcome these size and resonance window limitations, non-spheroidal nanoring morphologies were considered.

Nanorings support two dipole plasmon resonances that are excited with incident, polarized light which shift correspondingly different with changing ring geometry. These two modes are denoted at anti-symmetric and symmetric [101]. The first, anti-symmetric mode occurs when the two opposite walls along the direction of polarization contain separate dipoles. Each dipole has a dipole moment pointed in the same direction as the incident electric polarized electric field. The symmetric mode occurs when one wall has a net negative charge and the opposite has a net positive charge, while maintaining charge neutrality. The dipole moment of the symmetric mode also points along the direction of incident polarization.

Plasmon resonance of Au nanorings was calculated using the discrete dipole approximation. A point dipole approach was not utilized for determination of single particle plasmon properties since an analytic polarizability only exists for quasi static toroids. Nanorings add an additional degree of freedom with particle dimensions in the thickness of the ring wall. It has been shown that plasmon resonance wavelength is dependent on the aspect ratio of the wall diagonal length to the inner radius as shown in Figure 6.9. The figure shows the energy location of plasmon resonance as found in the literature and as determined for this work. In the literature, techniques for simulating nanoring resonance included finite difference time domain (FDTD) [102, 103, 104], boundary element method (BEM) [101], finite element method (FEM) [105], and various methods for tori [65, 106, 107]. Also in the figure are results from DDA for this work published in Ref. [77].

From Figure 6.9, it was observed that the plasmon resonance tended to blue shift with

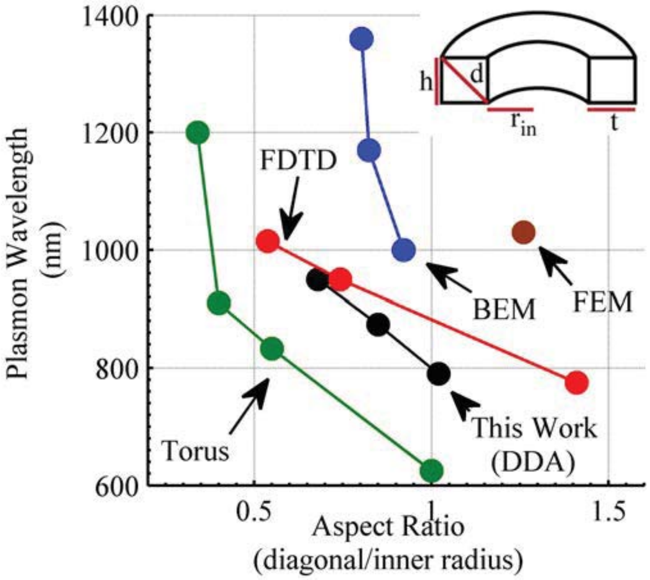

Figure 6.9: Trends of plasmon resonance in nanorings as a function of aspect ratio using different computation techniques including finite difference time domain (red), boundary element method (blue), and finite element method (brown). Also shown is various computational methods for torus shaped particles (green) and results from this work using the discrete dipole approximation (black) [77].

increasing aspect ratio. This observation was consistent regardless of the computation method used. It should be noted that the plasmon resonance of the BEM and FEM works were given for nanorings with inclusion of the substrate. This explained the apparent of redshift of the reported plasmon resonance values for these two methods in the figure. Blue shifts of the plasmon mode occurred as a result of interactions between the inner and outer ring wall. Plasmon resonance shifting can be explained by considering a perfect disk.

A nanodisk in the quasi static limit has a single plasmon resonance associated with the dipole mode. If a small hole is punctured in the center of the disk a hybridization occurs between the symmetric and anti-symmetric modes which occur at virtually the same resonance. As the punctured hole increases in size, the anti-symmetric mode does not shift. However, the symmetric mode begins to redshift due to resistance in electron oscillation from the new charges at the center. The limit of plasmon resonance as the wall thickness becomes zero (i.e. aspect ratio goes to zero) is infinity [77]. However, this is limited in reality by quantum mechanics and the mean free path of electrons in the ring wall.

Chapter 7: Fabrication of Samples

Predicted simulation results for far-field coupling of diffractive photons with near-field plasmons were given in Chapters 5 and 6. The resulting Fano resonance from the broad plasmon and narrow diffracted photon was shown to be dependent on both lattice parameters and particle composition and morphology. Comparison of predictions with experimental spectra have been done to show macroscopic agreement [108]. In this dissertation, individual nanostructures were created to consider morphological effects on broad band plasmon resonance and the effects of inclusion of graphene as a substrate to plasmon oscillation. First, this chapter discusses fabrication of nanostructures used in experiments assess local plasmon resonance and effect of the conductive graphene substrate.

Metallic nanostructures can be fabricated using a variety of methods. This chapter describes the method used to fabricate ordered arrays of gold (Au) nanoparticles with a focus on the techniques used to create the samples situated on 50 nm thick silicon nitride (SiN) membranes. Some methods of nanoparticle fabrication include electron beam lithography (EBL), nano imprint lithography (NIL), dip pen lithography (DPL) nanosphere lithography (NSL), and several others. The patterns created for this work were done using EBL and thermal evaporation was used to metalize the substrate due to the fragility of the required substrate. Nanostructures were created on commercially purchased transmission electron microscope (TEM) grids (Ted Pella, Inc.) consisting of 50 nm thick silica nitride (SiN) membranes supported by 200 micron thick silicon TEM supports for characterization using electron energy loss spectroscopy (EELS). Each TEM grid had nine square windows with 100 micron edges as shown in Figure 7.1. It can be seen that each window has a degree of error in regard to exact length and width dimensions. Lithographed patterns were drawn in the windows for the electron transparency important in TEM characterization.

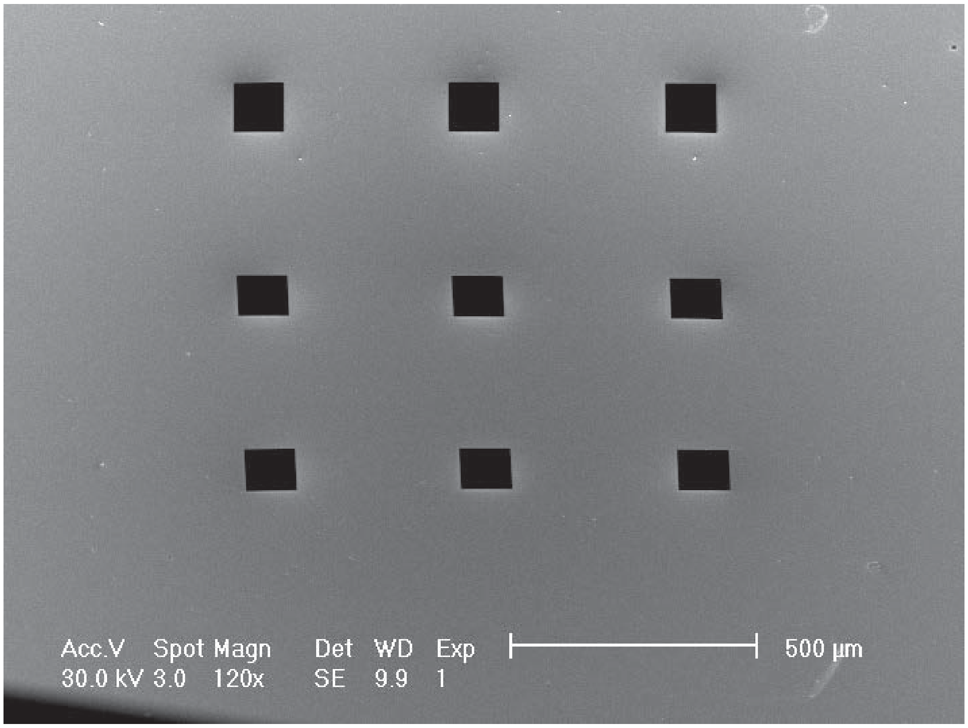

Figure 7.1: Scanning electron micrograph of purchased TEM grid with nine 100 micron square 50 nm thick SiN membrane windows.

7.1 Nanoparticle Arrays

7.1.1 Lithographic Patterning

Electron beam lithography (EBL) is a common technique that is used to pattern a resist for creating nanostructures. Figure 7.2 shows a schematic for the entire EBL process including graphene transfer (steps (a) through (d)) and lithography with a graphene layer (steps (e) through (j)). Lithography was also performed without the graphene layer by ignoring steps (a) through (d).

For EBL a uniform electron resist is first spin cast onto a pre-cleaned substrate (f). In this work, The TEM grid was pre-cleaned using sequential one minute acetone, methanol, and isopropyl alcohol bath followed by a deionized water rinse. Then, the sample was carefully dried with a slow nitrogen stream and a 2% 495k atomic molecular weight (amu) polymethyl methacrylate (PPMA) diluted in anisole was used as the resist. A spin speed of 4000 rpm was chosen giving a resist thickness of about 80-100 nm. Other resists such as ZEP and 950 k PMMA were tested

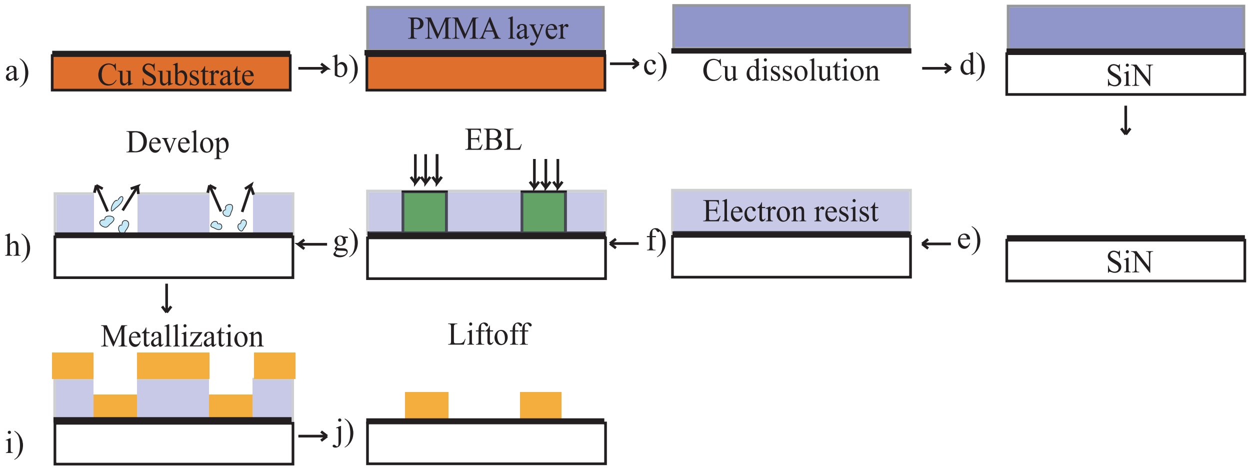

Figure 7.2: Schematic showing graphene transfer (a-d) for electron beam lithography on SiN membranes (e-j).

but proved problematic in the liftoff stage. Once a suitable resist was determined no changes were made due to the dependence of electron beam parameters for lithography on the type and thickness of chosen resist.

After spin casting, the resist was cured on a hotplate at 200° C for two minutes. The sample was then ready for electron exposure, which was done using a nano pattern generation system (NPGS) in a Phillips XL 40 scanning electron microscope (SEM) (g). The pattern for electron exposure was defined in a computer aided design (CAD) program. The program allowed user defined patterns, line types, area types, number of passes, and electron dose. As an example, a circle could be drawn with only the circumference exposed. Or, the same circle could be drawn with concentric circles inside to the center or the entire center could be exposed leaving a disk. This is one way in which rings and disks can be drawn and was how this work created the different shapes.

The incident electron beam breaks apart the polymeric bonds in the resist which was later washed away using a developer. For PMMA, the developer was a 1:3 mixture of isopropyl alcohol (IPA) to methyl isobutyl ketone (MIBK). The sample was put in a bath of the developing solution for 40 seconds and immediately placed in IPA to stop further development (h). Underdevelopment can lead to poorly defined lines and structures that may not reach the substrate. A pattern that is not fully developed to the substrate cannot be used as a mask for metallization. Over developing can lead to thicker lines with a greater variation in the size of structures. Dose of the electron beam that is required required to break the bonds in the resist depends on the resist composition, resist thickness, and underlying substrate. Then, the sample was metalized (i) and liftoff was performed (j) to remove the sacrificial PMMA leaving the gold nanostructures. Specific consideration of metallization and liftoff are given in Sections 7.1.4 and 7.1.5.

Electron dose is defined as the amount of charge that is incident on the surface of the resist. The three types of electron dose allowed are area, line, and point with units for the dose types being nC/cm^2, nC/cm, and nC, respectively. To determine dose, the beam current must be measured in the SEM prior to exposure. A Faraday couple internal to the SEM and an external volt meter were used to measure the current before each run. The exact current can display small changes from day to day depending on wall current to the SEM and quality of the electron gun. Specified dose was delivered to the substrate by changing the dwell time of the beam on the surface. In other words, the speed that the beam draws patterns was modified based upon the current measurements to deliver consistent dose for different samples.

The NPGS allowed user defined patterns to be created which then controlled the beam shift to draw the patterns on the sample. In the SEM, three conditions effect quality of the lithographed patterns, beam optimization, beam energy, and electron dose. First, optimization of the electron beam included both focus and astigmatism. The sample was attached to a lithography stage that was brought to the optimal focal plane for the microscope. This height for the Phillips XL 40 was 10 mm. Stigmators were then adjusted to control the circularity of the beam. Astigmatism in the beam causes uneven line thicknesses for horizontal and vertical directions. A gold standard was situated on the stage and used to optimize beam conditions. Second, high tension beam energy controlled the amount of scattering after the electrons contacted the surface of the PMMA. This created an undercut in the resist and limited the minimum achievable line width. Beam accelerating voltage was set to the microscope maximum of 30 kV. Third, electron dose was set by changing the amount of time the beam remained in a given location. Each resist type, resist thickness, and substrate combination require a different minimum dose in order to have successful removal of the exposed resist to the surface of the substrate during the development stage. Increasing dose past this value acted to control the desired thickness and size of the drawn patterns.

7.1.2 Lithography on TEM grids

Electron beam lithography has been a known and developed process for many years. The difficulty of this work was performing EBL on the particular chosen substrate. The TEM grid was only 3 mm in diameter and contained windows of only 50 nm thick SiN. This combination made it impossible to place the grid directly on the vacuum chuck to perform the spin coating step. This was overcome using a square centimeter diced silicon chip as a carrier for the TEM grid. Typically, carbon tape would be used to adhere the TEM grid to the carrier chip. However, this created an uneven surface resulting in a non-uniform resist layer and fractured the TEM grid or SiN windows when removing the sample from the carrier chip. The carbon tape was replaced by an intermediate layer of PMMA that was spin cast onto the bare silicon chip at 1000 rpm. The TEM grid was then placed on the coated silicon chip and cured. The main advantage of this process was that the TEM grid was easily removed with the liftoff stage where the sacrificial PMMA was dissolved. Due to the small size of the TEM grid, edge effects from spinning were evident. As a result, even this method proved difficult in creating a uniform PMMA layer.

Disks, rings, oligomers, and rods were drawn using EBL on PMMA coated SiN windows. Differing dose parameters were done to determine substrate effects on line thickness for the combination of PMMA on SiN windows. Figure 7.3 shows rings drawn with outer diameter of approximately 1090 nm and inner diameter 820 nm giving a line thickness of 135 nm. Electron dose for these rings was set to 5.2 nC/cm. This value was larger than most substrates since the SiN is transparent to fast moving electrons. Equivalent lineshapes with EBL done on the same PMMA layer situated on a copper substrate required 0.7 nC/cm. These rings in the figure were near the side of the SiN window, which was be determined by the contrast change of the last column of rings

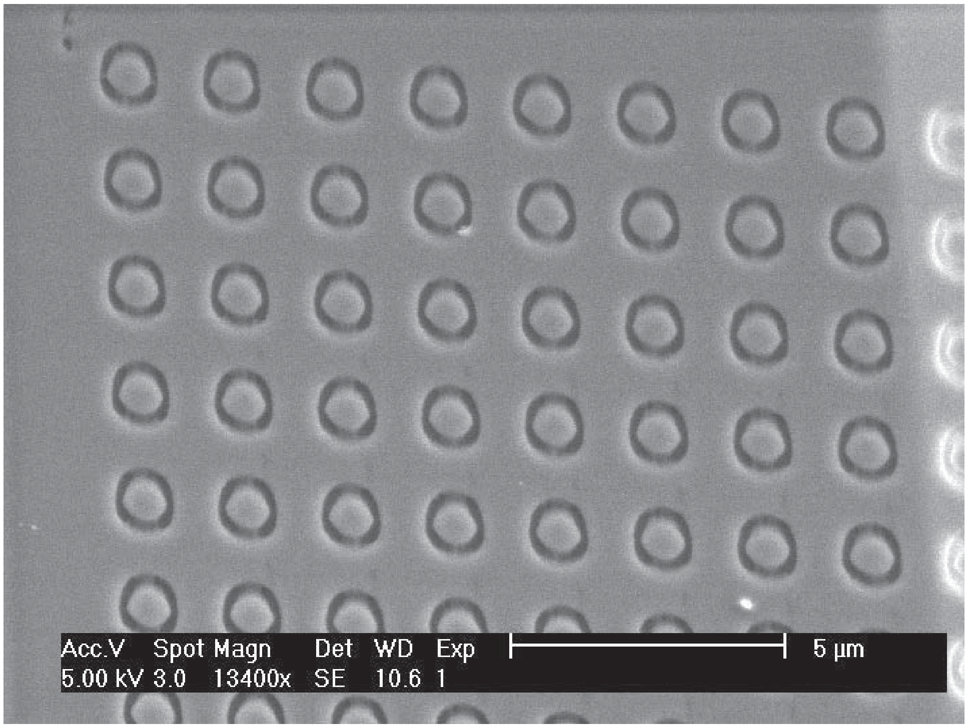

Figure 7.3: Scanning electron micrograph of ring structure patterned using EBL.

on the right of the image. Only patterns drawn on the window could be examined in the TEM. It appeared by the image that some of the rings were not quite complete. The very top and bottom of some rings did not appear to be fully developed. This was most likely caused by two factors. First, the non-uniform PMMA layer made exact dose requirements difficult to determine. Second, slight astigmatism in the beam seems to have had a larger horizontal cross section than vertical.

Different types of oligomer structures with varying dose and slight astigmatism can give differing structures as seen in Figure 7.4. In the figure, four different particle types are seen: disks (upper left), disks with vertical points (lower left), disconnected semicircles (upper right), and separate oligomer particles (lower right). Each particle type could be analyzed using EELS in the TEM to consider effect of shape and size on plasmon energy resonance to manipulate the optical properties of metal nanostructures. Dimensions of any individual nanoelement was between 65 and 650 nm. Each individual element was separated with a center-to-center distance of 1,000 nm, so interactions with neighboring particles were not expected. However, interactions between the disconnected semicircles were expected due to near-field interactions. Near-field coupling is the

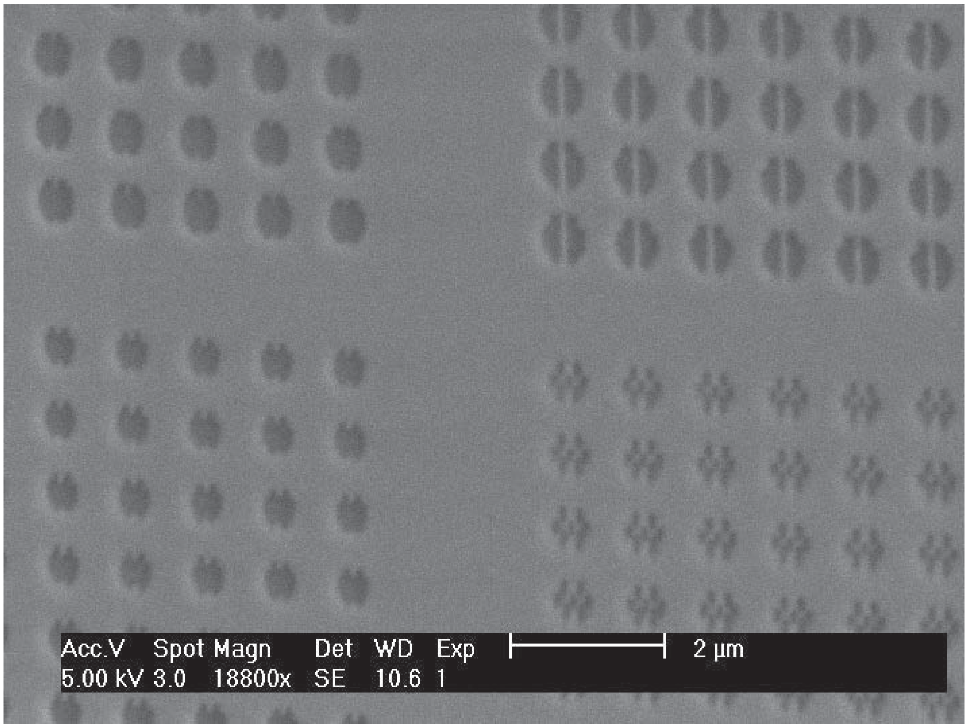

Figure 7.4: Scanning electron micrograph of various oligomer structures patterned using EBL.

source of exciting multipolar modes through Fano resonance [109].

7.1.3 Electroless Gold Plating

Growth of colloidal nanostructures often uses the reduction of Au solution mostly found in the form of gold tetrachloro aurate (TCA) ($H[AuCl_4]$) [110]. One particular reduction method is electroless (EL) Au plating. EL Au plating is a bottom-up method that uses a series of steps to treat and presensitize a substrate with various solutions so that a uniform Au layer can be deposited [111]. A glass or quartz substrate is presensitized by immersion in trifluoride acid to etch the surface and remove defects. The surface is cleaned and rinsed with distilled, deionized, degassed (DDD) water then dried with N_2 gas. The substrate is immersed in a tin (Sn^{2+}) solution which binds to the surface in order to allow absorption of catalyst particles. Adhesion of silver (Ag) catalyst to the Sn^{2+} film is done by immersion in a Ag solution for 2 minutes. Au is deposited on the surface by galvanic displacement of the Ag by either immersion [111] or a continuous flow [112] setup.

For this work, electroless plating was performed in fewer steps utilizing the CVD grown graphene on copper. The copper acted as the reducing agent for the TCA which allowed the solution to be placed in direct contact with the as-grown graphene on copper to produce nanoparticles. This process was performed on purchased the CVD graphene on copper to decorate the graphene with approximately 30 to 50 nm diameter nanoparticles as discussed previously in Section 3.4 in regards to assessing graphene transfer quality. While this process was not used for electron energy loss spectroscopy analysis or for creating lithographed structures, it is the focus of future work. If lithographed nanostructures can be fabricated directly on the graphene on copper system, it can be transferred to any arbitrary substrate using methods described in Section 3.4.

7.1.4 Evaporation

The method of metallization of patterned resists utilized in this work was metal evaporation. A solid metal was heated in a carbon crucible using a directed electron beam (e-beam) or in a metal boat through which a current was passed to heat the metal source (thermal) in a high vacuum environment of $\sim 10^{-5}$ Torr. Once the metal reached a particular temperature, it began to evaporate radially from the source. The sample to be metalized was attached to a chuck facing the metal source positioned vertically. A blinker was moved between the source and sample for nanometer thickness precision.

Au nanostructures evaporated on the SiN TEM grids for this work were fabricated using thermal evaporation in an Edwards Auto 306T. Electron beam (e-beam) evaporation was initially tried, however, liftoff was not observed and down equipment time made use of e-beam evaporation implausible for completion of this dissertation. Since Au has a low surface energy, an adhesion layer of 2 nm thick chromium was deposited before 8 and 15 nm of Au, depending on the sample. Each sample was positioned exactly above the source and rotated to give more uniform deposition of the metal film. Temperature of the sample was monitored with an internal thermocouple since overheating of the PMMA causes over-curing, making it impossible to remove the sacrificial resist without damaging the nanostructures. It was observed in transmission electron microscopy that structures were not perfectly uniform with several differing crystal orientations observed.

7.1.5 Liftoff

Once the sample was metalized, the sacrificial PMMA was removed leaving the patterned Au structures behind. Typically, ultrasonication of the sample in acetone is sufficient to remove the residual PMMA. However, the 50 nm thick SiN membrane was too fragile to perform sonication. Instead, the sample was immersed in an PG Remover bath for five days with slight, periodic agitation of the beaker. During this time, a pipette was used intermittently to generate air bubbles on the surface of the sample to help release the residual resist layer. A directed stream of PG Remover or Nitrogen gas could not be incident on the sample owing to the fragility of the SiN windows. This two-step process was repeated until no visible PMMA layer was observed on the grid. Even with this more gentle method compared to sonication, it was typical to have two to four of the nine total windows break.

Results of metallization and liftoff are shown for three cases: rings, oligomers, and defect areas. Each figure shows the ability to obtain nanoparticle structures on the surface and what types of defects are likely to occur. First, Figure 7.5 shows three nanoring arrays with outer diameters of $\sim$1,000, $\sim$550, and $\sim$700 nm with a wall thickness of $\sim$125 nm for all rings. Results showed that it was possible to fabricate these rings on the SiN window for TEM analysis. Three defects occurred in some rings shown in the figure. First, some rings showed PMMA resist remaining inside the center of the ring. While this was unintentional, it provides the opportunity for future work to explore the change in plasmon resonance when the center is filled. Such structures are predicted to provide an improved sensing platform due to concentrated light in the center of the rings from plasmon oscillation. Second, some of the larger rings at the top of the left array were incomplete. However, this provides the opportunity to consider near-field interactions between two adjacent curved nanorods for future work. Third, it was observed in the center array with the smallest diameter rings that one of the rings was partially missing. It was presumed that part of the ring was removed during the liftoff step.

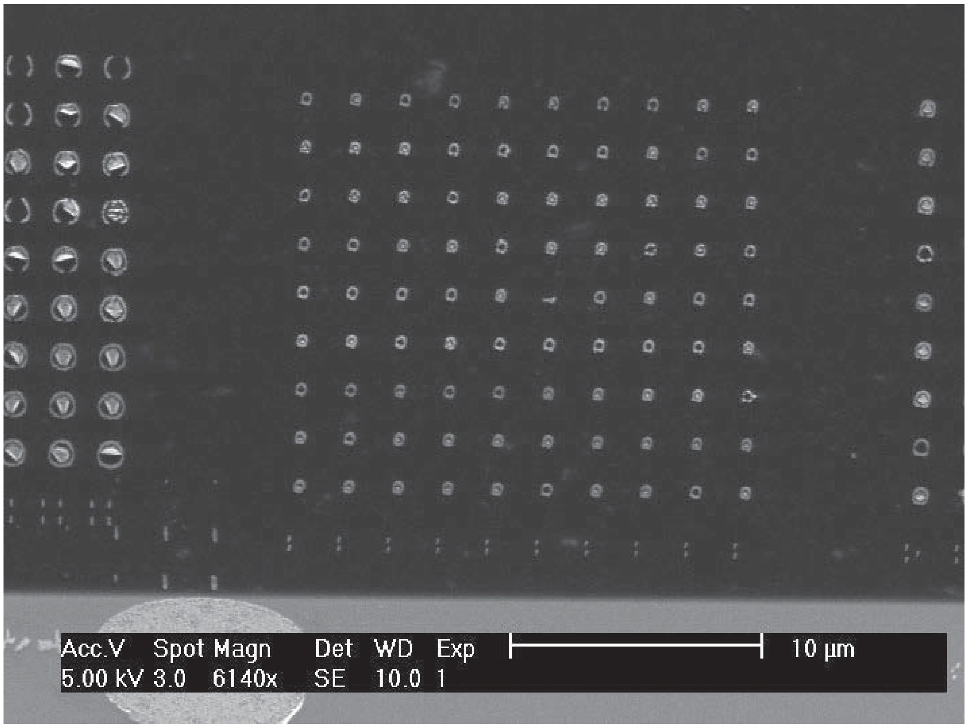

Figure 7.5: Scanning electron micrograph of Au rings on SiN membrane.

The second liftoff example is of oligomers shown in Figure 7.6. This arrangement is a hexamer, a collection of six 50-65 nm radius nanodisks in the shape of a hollow hexagon. Two liftoff defects appeared in this image as well. First, there were some missing nanoparticles. This was caused by the evaporated Au sticking to the PMMA layer as it is removed from the surface of the SiN TEM window during the liftoff step. However, this allows for future work in examination of the effect of plasmon resonance of these hexamer structures when certain particles are missing. Second, there was some residual PMMA remaining on the surface. In the figure, this residual PMMA was located primarily in the upper left hand corner. Due to the inhomogeneous nature of this defect, it provided no addition experimentation and rendered the area around this defect unsuitable for EELS. It was presumed that the data would be too difficult to interpret consistently. Various other oligomer structures were fabricated as well on this sample (data not shown).

The third and final liftoff example shows where PMMA failed to be removed from the surface as shown in Figure 7.7. Two defects were observed on this window. First, the PMMA layer failed to be entirely removed from this portion of the sample. It was seen the the PMMA had

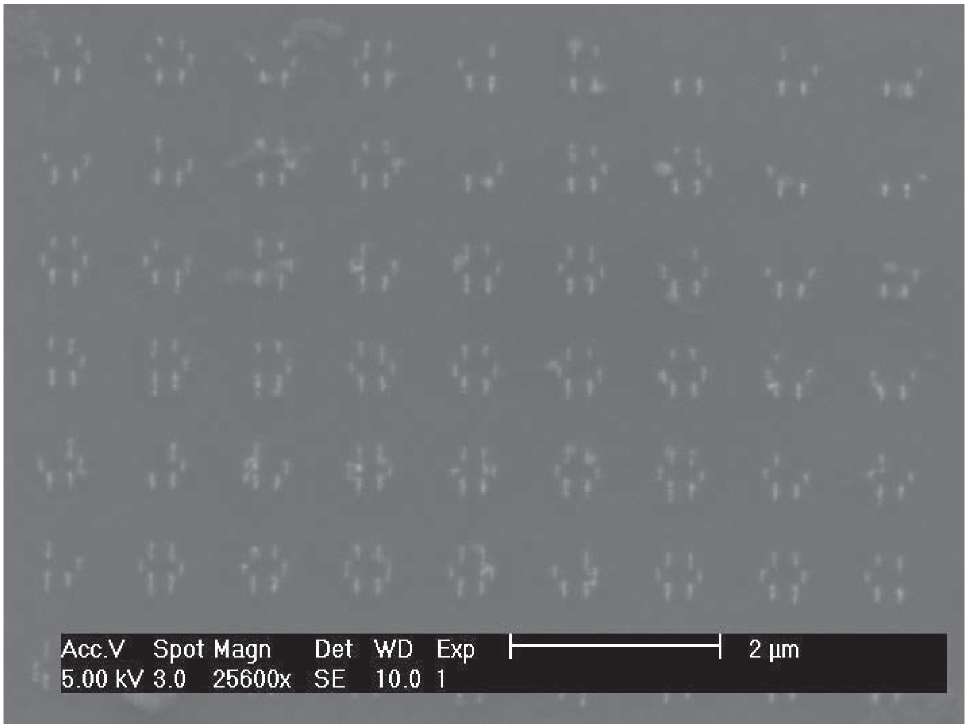

Figure 7.6: Scanning electron micrograph of Au hexamers on SiN membrane.

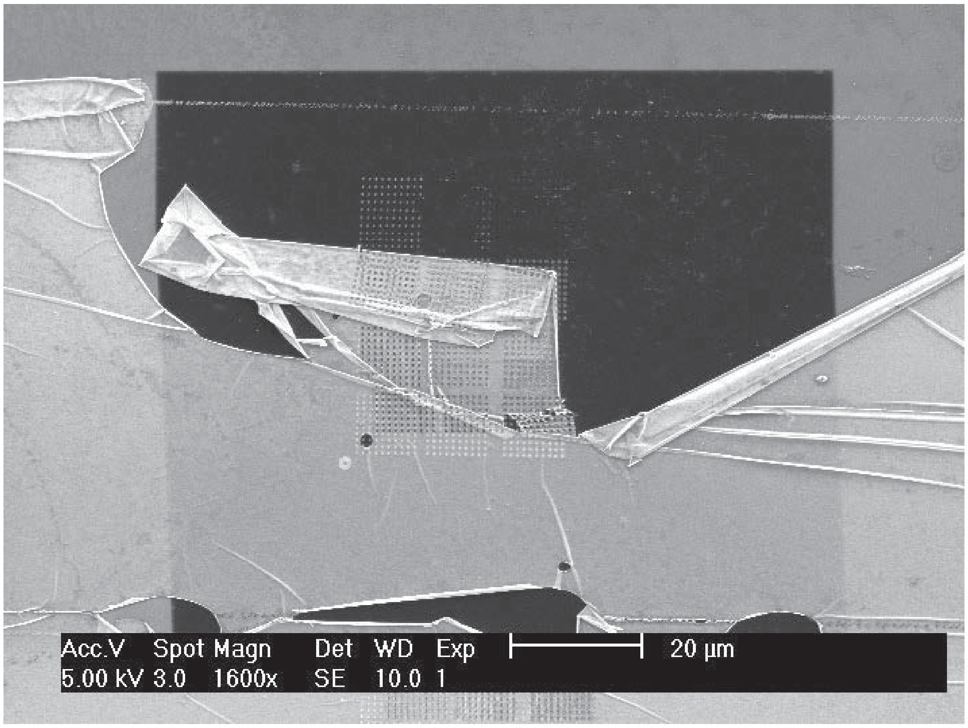

Figure 7.7: Scanning electron micrograph of residual PMMA not fully removed with missing nanostructures.

shifted from its original pattern from the mismatched holed in the PMMA to the Au nanoparticles underneath. Second, it was observed that where the PMMA was successfully removed, so were many of the underlying nanoparticles. Even though many particles were removed, there was still a region on this window where EELS could be performed on the remaining particles where the PMMA successfully lifted off. Sonication of the sample would have removed this PMMA, but would have broken the windows and rendered the sample useless.

Each of the images shown in this section are examples of the structures that were created using electron beam lithography on SiN membranes for examination in transmission electron microscopy. Sphere, disks, microstructures, rods, triangles, and various other morphologies could be examined as their potential as nanoantenna. The following two sections shows show results for purchased graphene and fabricated nanostructures that were created on top of graphene that was transferred onto a SiN TEM membrane.

7.2 Graphene

Fabrication of graphene consists of various methods including exfoliation and chemical vapor deposition (CVD) as outlined in Section 3.3. Graphene grown on 25 micron thick copper foil using CVD was purchased from the Graphene Supermarket. Transfer of purchased graphene was done in accordance with Section 3.4. Figure 7.8 shows a scanning electron micrograph of as-received graphene on copper. Individual atoms forming the hexagonal lattice could not be resolved in SEM, but grain boundaries from different points of catalytic growth in the graphene were distinguished. Also evident in the micrograph were the horizontally oriented copper grains of the foil.

Before the as-received graphene on copper could be used, it went through a cleaning process to remove surface contaminants. As the sample ages, adventitious carbon as well as organic compounds from the air collect on the surface. An acetone, methanol, and isopropyl wash from a squirt bottle stream was performed before any other step. The micrograph in Figure 7.8 shows as purchased graphene after it went through the described wash cycle. Pre-washed samples contained

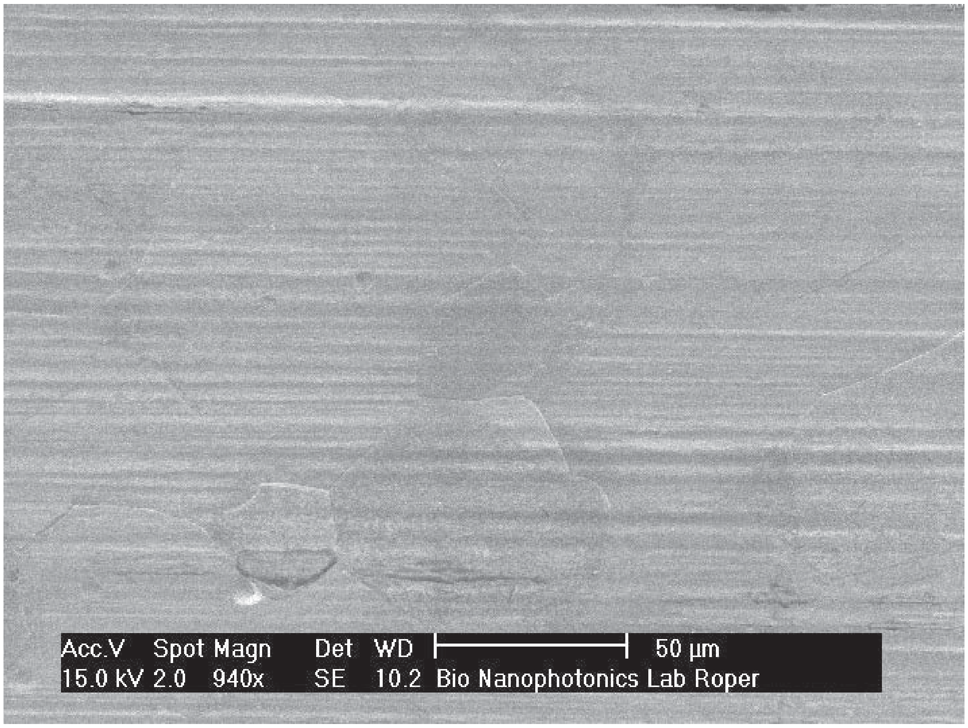

Figure 7.8: Scanning electron micrograph of purchased, CVD grown graphene on copper.

clearly seen irregularities and impurities of small particulates and a non-uniform surface (data not shown).

7.3 Composite

In order to perform EELS on the nanostructures with a graphene substrate, methods of graphene transfer and nanoparticle fabrication were combined together. First, a monolayer of graphene was transferred to the TEM grid between the cleaning and PMMA spin coating steps. Then, the normative, unchanged process for electron beam lithography as described previously was performed. This resulted in a graphene monolayer between the SiN membrane and the Au nanostructures. Observed imperfections in the transfer process madeit possible to directly compare side-by-side structures on the same sample with graphene present and not present below the nanoparticle. Near-field plasmonic mapping using EELS for the graphene/Au nanostructures could then be compared to the mapping without graphene to assess the underlying differences.

Regular and elliptical disks were fabricated for comparison between graphene and non-graphene interacting nanostructures. Disks were chosen since nanorings possesses a strong plasmon shift when small changes in ring dimensions are altered. This makes direct attribution of graphene effects difficult when comparing between two different rings. Furthermore, EELS on lithographed, silver nanodisks has been performed in the literature making comparison with previous work possible [113].

Two disk geometries are shown in Figure 7.9 as examples of fabricated structures. Following the procedure given earlier in the chapter, a graphene substrate was present in certain lithographed samples. Fabricated on top of the graphene were disks with 2 nm of chromium and 15 nm of gold. Imperfections in the transfer process gave cracks and regions where no graphene was transferred. This allowed examination of disks with and without a graphene substrate generated using the exact same fabrication conditions to be examined. Figure 7.9 shows round nanodisks with diameter of $\sim$215 nm. The light gray region shows where graphene was successfully transferred to the SiN membrane and darker regions show bare SiN. It was seen that neighboring nanoparticles could be characterized and compared to ascertain the effects of graphene on the underlying plasmon resonance.

It was observed in Figure 7.9 that nanoparticles on top of the graphene appeared with a brighter contrast than the particles on the bare SiN membrane. Contrast in scanning electron microscopy was a result of relative amounts of secondary electron scattering that was picked up by the biased detector. It was unclear what the source of the increased brightness was of the particles on graphene compared to those off graphene. One possible explanation is that secondary electrons ejected from the gold nanostructures on the graphene had excess electron transport to the structures through the graphene giving additional electrons available for secondary electron emission.

Scanning electron micrograph of fabricated elliptical disks are shown Figure 7.10. These disks have dimensions of approximately 540 and 230 nm for long and short diameters. Similar to the previous figure for disks, the lighter area at the top corresponded to a graphene substrate on the SiN and the darker region on the bottom is bare SiN. Another feature in this image was on the left where a brighter material is seen. This was the PMMA superstrate that was not entirely removed

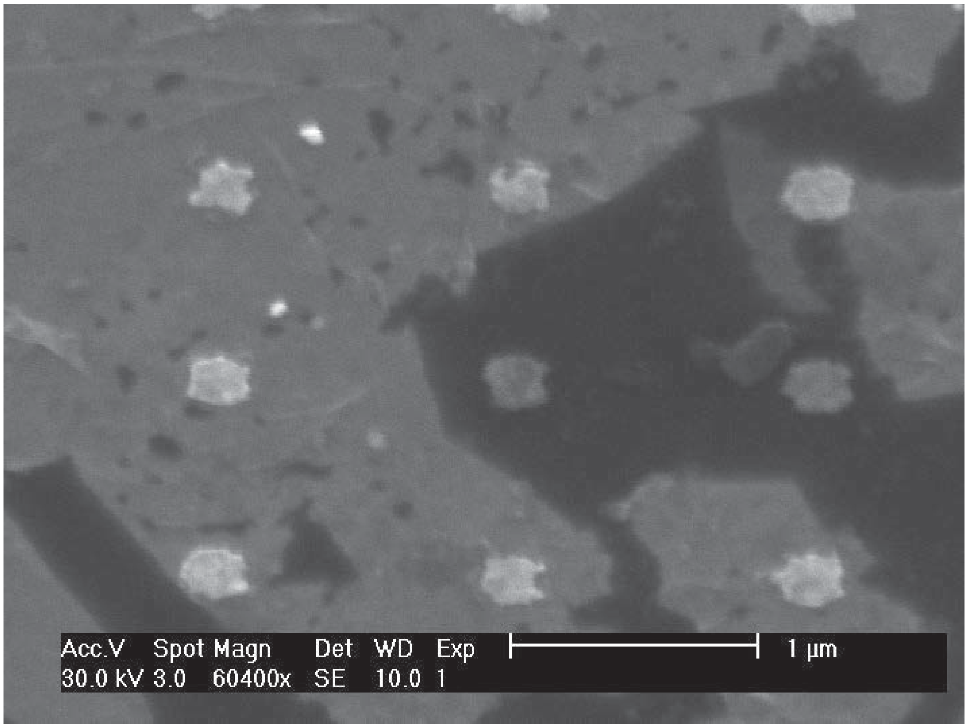

Figure 7.9: Scanning electron micrograph of disks on graphene on silicon nitride (bright substrate) and bare silicon nitride (dark substrate).

during the liftoff stage. Due to the local nature of EELS experimentation, it was not expected that this defect had an effect on on the corresponding EELS data that was generated from these shapes. As was seen in the previous figure, particles on the graphene appeared to have a brighter contrast than the ones located on the bare SiN.

A scanning transmission electron micrograph (STEM) of one of the ellipses on graphene from Figure 7.10 is shown in Figure 7.11. Measurements of the ellipse were taken and are shown in the figure. Uniformity of the ellipse was observed to be sufficient for interpretation of acquired EELS spectra. Resolution of the micrograph allowed determination of differing grains in the atomic structure of the particle. Owing to the difficulty of obtaining atomic resolution with STEM and the contrast difference between the metal and substrate, it was not possible to resolve individual carbon atoms in the graphene which were present on the substrate.

Transmission electron microscopy was performed on the samples for higher resolution imaging. Figure 7.12 shows sub-nanometer resolution capability of the TEM with resolved atomic

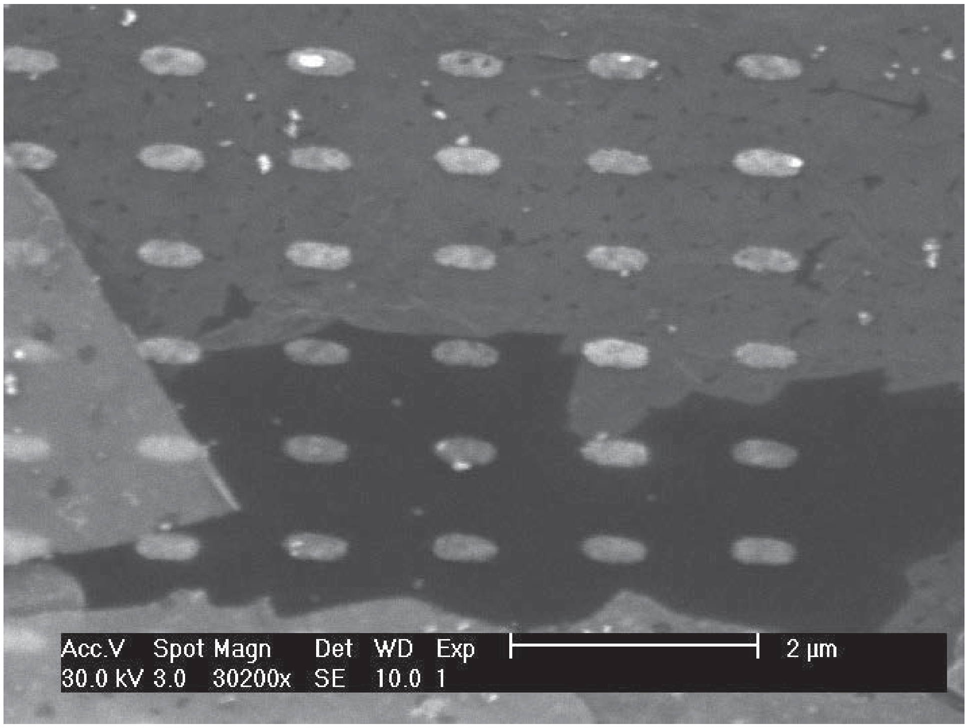

Figure 7.10: Scanning electron micrograph of elliptical disks on graphene on silicon nitride (bright substrate) and bare silicon nitride (dark substrate).

Figure 7.11: Scanning electron micrograph of elliptical disks on graphene on silicon nitride (bright substrate) and bare silicon nitride (dark substrate).

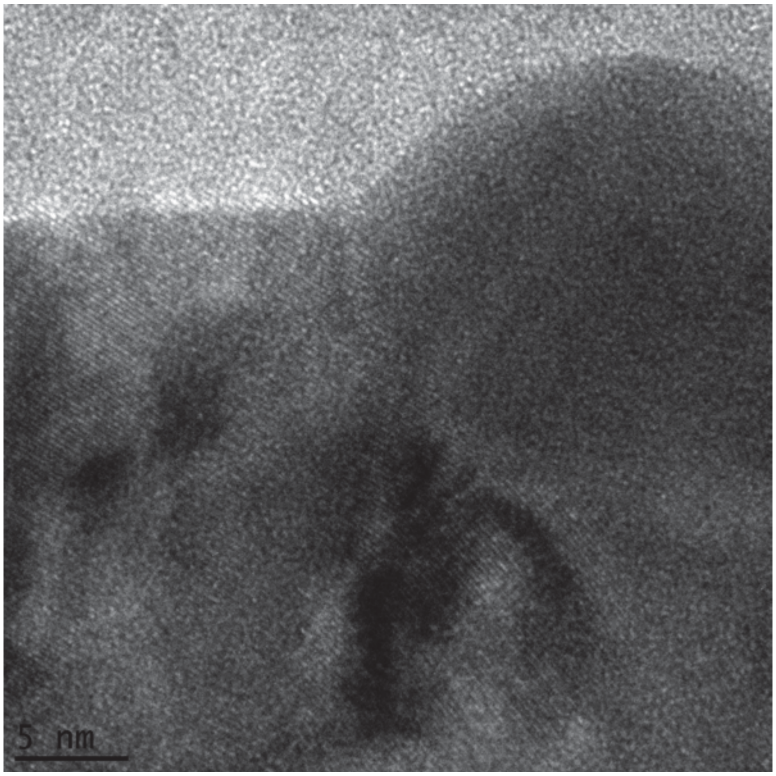

Figure 7.12: Atomic resolution transmission electron micrograph of gold disk (darker contrast) on silicon nitride (brighter contrast).

planes on the gold. Darker contrast on the bottom portion of the micrograph was gold while the brighter contrast op the top portion was the SiN membrane. It can be observed that the gold structures were semi crystalline with at least two orientations shown in the figure. Grain boundaries in the fabricated structures were expected to give some discrepancies between experimental and simulated data due to uneven height and slight variations in dielectric properties across grains. Additionally, it was difficult the resolve graphene atoms in addition to the gold. This was a result of interference of the 50 nm thick SiN substrate under the sub-nanometer thick graphene layer. However, micrographs of the region between gold particles revealed discernible atomic grains in certain areas (data not shown).

7.4 Alternative Approach

An alternative approach to creating reproducible nanostructures is Nanoimprint lithography (NIL). NIL is a technique that allows high resolution nanostructures to be fabricated with a high degree of repeatability. This process is likened to stamp that creates an image by first pressing the stamp in ink followed by pressing the stamp on a surface top create the image on the stamp. A master stamp in NIL is created by a conventional lithographic technique, such as electron beam lithography. The stamp contains a periodic pattern that is copied using a thermoplastic or thermocuring polymer. The polymer, once cured or solidified, contains a negative of the pattern contained on the master stamp. The polymer can be used in a variety of ways, including usage as a stamp itself, used as a sacrificial polymer for metallization and liftoff, as a mask for selective etching, etc. While this process shows great promise for mass producing patterns of large size and great quality, use of this method was not appropriate for this work owing to the fragility of the 50 nm thick SiN membrane windows used.

Chapter 8: Characterization

Characterization of the samples included techniques to determine graphene and nanoparticle quality as well as their spectroscopic response to electrons. Methods of verifying quality of graphene were x-ray photoelectron spectroscopy (XPS) as well as scanning and transmission electron micrographs. Near-field mapping of plasmon modes was done using electron energy loss spectroscopy (EELS). Morphology of structures was confirmed with scanning (SEM) and transmission (TEM) electron microscopies. The SEM used in this work was a Phillips XL40 from FEI located in Dr. Keith Roper's lab. The TEM used was a Tecnai G2 F20-TWIN from FEI located in the Materials Characterization Laboratory at the Nano Institute. The XPS equipment was a VersaProbe from PHI using a kα x-ray from an aluminum source located in the Materials Characterization lab in the Nano Institute.

8.1 X-Ray Photoelectron Spectroscopy

X-ray photoelectron spectroscopy (XPS) is a characterization technique that fingerprints the elements on the surface of a sample. X-rays are guided toward the sample at a specific, known energy value that is larger than the work function of materials. This allows electrons in the sample to absorb energy from the incident X-ray and become ejected from the sample. The net energy ejected electron is the X-ray energy minus the work function of the material. Ejected electrons are then collected and separated using a curved capacitor and intensity plots of the number of electrons containing a specific amount of energy is given. The peaks in the resulting plot are analyzed and the peak location gives an indication of the work function, and consequently the composition of the sample.

To accurately and consistently interpret the spectra, a few items must be considered. First, each spectra must be calibrated. This is typically done using the carbon peak. Every sample will have a small amount of carbon contamination from the air. The entire spectra is shifted to match the carbon peak to the known value. Second, this is a surface characterization technique. Information

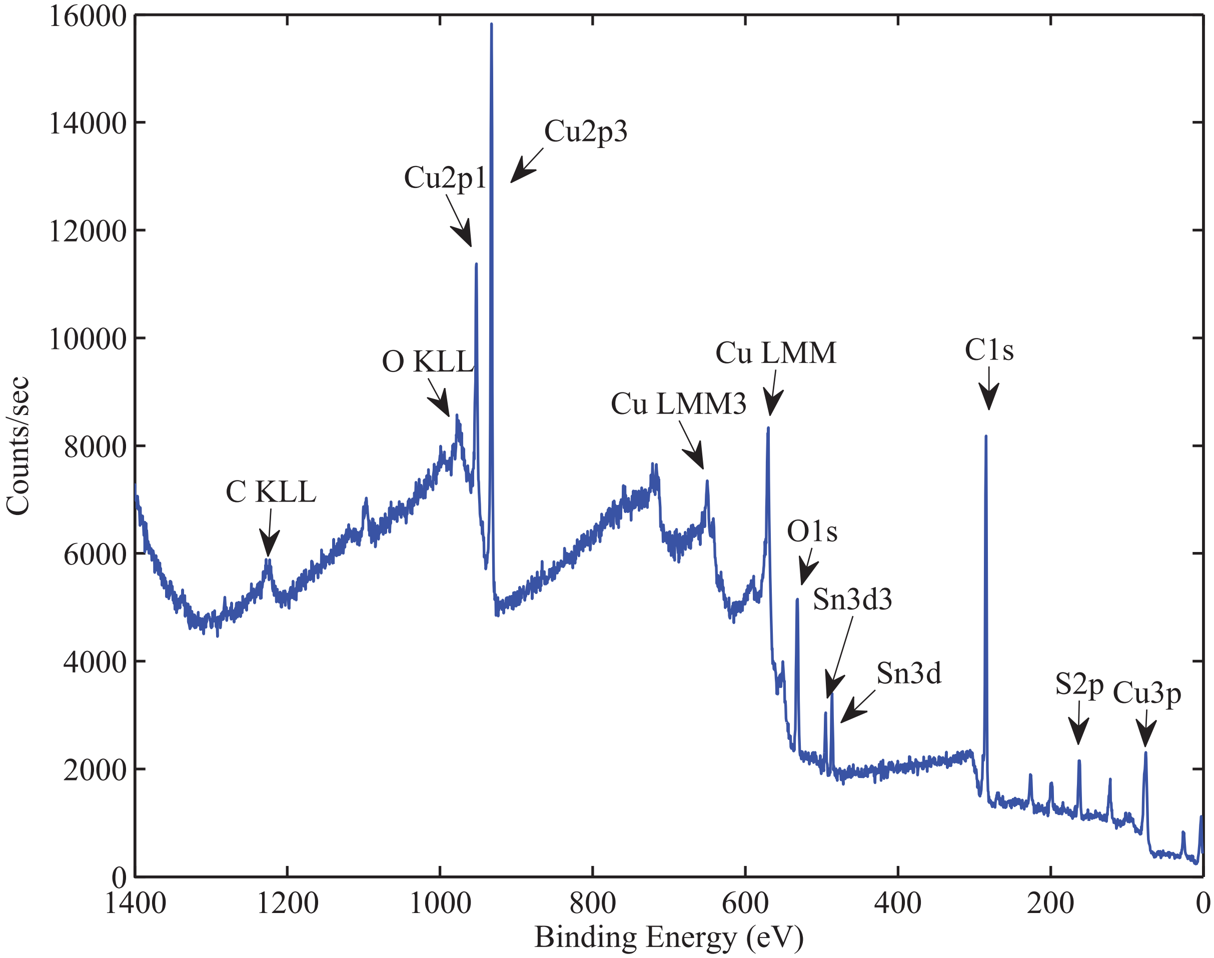

Figure 8.1: X-ray photoelectron spectroscopy of purchased, CVD grown graphene on copper.

can only be obtained up to about a 4 nm depth into the sample. Third, the work function of a material is dependent on the type of bond the atom experiences. As a result, small shifts in peak location and changes in the width of the peak give information about both chemical composition and bonds in the sample.

X-ray photoelectron spectroscopy was performed on the purchased chemical vapor deposition (CVD) graphene on copper sample to determine the purity of the received sample. The spectral intensity plot is given in Figure 8.1. Analysis revealed six major elements on the surface of the graphene on copper sample. First, carbon (C) and copper (Cu) were observed. Several peaks for different electron energy levels for Cu and C were present confirming their presence. Additionally, oxygen (O) was observed. This was expected due to oxidation of the carbon on the surface. Each of these three materials were expected to be seen in the XPS analysis.

Three addition elements were present in the sample which were not expected: Sulfur, chlorine, and tin. Since no information is known about the exact CVD system used to grow the purchased graphene, it could not be fully determined what the source of these materials are. It is presumed that these are defects from residual chemicals in the CVD system. From Figure 8.1, the relative percentage of each element was calculated for for sulfur, chlorine, and tin to be 6%, 2%, and 1%, respectively, revealing relatively low amounts of these three elements.

It was difficult to confirm the existence of graphene purely from XPS analysis since all samples exposed to air will have carbon contamination on the surface. XPS was used in conjunction with other techniques to identify both existence and quality of the received graphene films. XPS allowed determination of foreign species on the graphene surface. Based upon the analysis, it was determined that contamination of the graphene was not sufficient to pose a problem in the analysis of graphene-nanostructure interactions.

8.2 Electron Energy Loss Spectroscopy

8.2.1 Introduction

Electron microscopy allows multiple characterization techniques of the sample. These techniques include secondary and backscattered electron detectors to obtain morphology and basic material differences by contrast comparisons. Composition can be compared by considering the image contrast using the same electrons. Emitted electrons, called Auger electrons, and x-rays can be used for spectroscopic elemental analysis. Furthermore, light emitted by swift electrons can be captured giving spatial resolution of the optical emission of nanostructures using a technique called cathodoluminescence. Finally, transmitted electrons can be collected and an energy loss spectrum of the transmitted electrons is measured in a technique call electron energy loss spectroscopy (EELS). The latter technique requires the use of a scanning transmission electron microscope (STEM). In STEM, a sub-nanometer electron beam is used as the probe and is rastered over the sample. A high angle annular dark field (HAADF) image is captured from scattered elec-

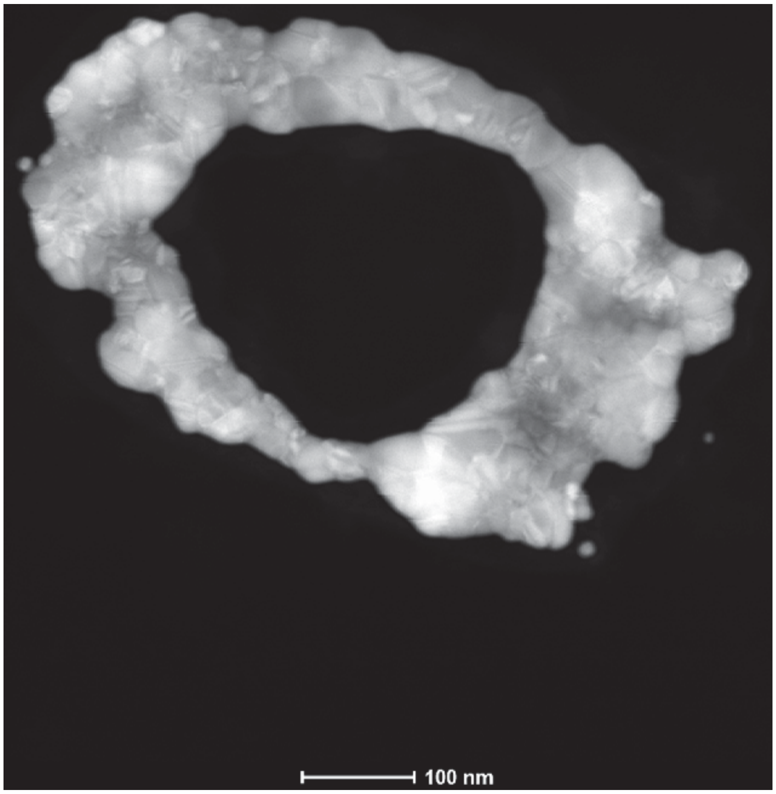

Figure 8.2: HAADF image captured using Scanning transmission electron microscopy of Au ring on SiN membrane.

trons with STEM. This HAADF image is used to guide the electron probe to specific locations on the sample. Figure 8.2 shows an example of a HAADF nanoring image captured using STEM.

EELS was used to glean information about band structure and plasmons with a spatial resolution of the nanostructure on the order of nanometers. Electrons were projected towards the sample at 120 kV. As the electron passed through or near the structures, a measurable amount of energy was transferred away from the incident electrons. The transmitted electrons were collected at the end and their energies were measured using a monochromator giving an energy loss spectrum with up to 0.05 eV resolution. For the interested reader, a review of these characterization techniques and others used in electron microscopy not discussed here can be found at [8].

EELS has been performed on a variety of nanostructures giving a spatial mapping of the energy loss around and within a single entity. These experiments have included dispersed nanoparticles including spheres [114] and triangles [115] grown using chemical synthesis, as well as a few lithographed structures such as disks [113] and bow tie antennae [116, 117]. Single entity plasmon resonance for these structures can be examined as spectra with the energy loss probability as a function of energy loss as well as mapping of plasmon modes in the structure. However, care has to be taken when interpreting the experimental results.

A few different suggestions have been made in the literature for the physical interpretation of EELS spectra as obtained in a scanning transmission electron microscope. One explanation is that the EELS spectra corresponds directly to the electromagnetic (or photonic) local density of states (LDOS) [118]. The photonic local density of states is expressed by

$$\rho_{\hat{\mathbf{n}}}(\mathbf{r},\omega) = \frac{-2\omega}{\pi}\Im(\hat{\mathbf{n}} \cdot G(\mathbf{r},\mathbf{r},\omega) \cdot \hat{\mathbf{n}}) \tag{8.2.1}$$

with $\hat{\mathbf{n}}$ being a specific unit vector and G being the electric Green tensor for Maxwell's equations. The photonic LDOS defines the combination of all eigenstates of the system, such as electric dipole, quadrupole etc. However, it was shown a year later that the EELS spectra does not quantitatively correspond to the photonic LDOS [119]. The latter showed that while qualitative agreement between EELS and LDOS can be made, there is no direct correlation between the two. The fundamental differentiation between the EELS and LDOS maps is due the different excitation source. Electrons interact with plasmons differently than photons due to the differing field distribution from each.

Electron energy loss spectroscopy does give an indication that the excitation of surface plasmons can be probed and optical properties evaluated. Several reports give agreement between plasmon excitation using electrons and photons by considering modal decomposition. Dipole, quadrupole, hexapole, etc. electric modes can be excited with both sources and compared together.

However, 'dark' modes can also be excited with incident electrons that photons couple weakly to. These modes are so-called 'dark' since they have a net zero dipole moment. These modes can be seen in a variety of situations as discussed below. In nanodisks, these 'dark' modes have been denoted as breathing modes [113]. This effect has been explored theoretically and computationally using Fano resonances to excite ’dark’ modes using incident photons. Broad ’bright’ modes, such as dipolar, are excited with an incident light source which decays into the narrow ’dark’ modes such as quadrupolar. This coupling interaction creates a Fano resonance in certain structures using near-field coupling to excite modes not previously seen using photonic excitement [19, 120].

8.2.2 Computational Model

Electron oscillation in arbitrary nanoparticle architectures under electron beam irradiation has been performed using a variety of computational electrodynamic methods. These methods include boundary element method (BEM), finite element method (FEM), and discrete dipole approximation (DDA). Each of these methods have particular advantages and best uses. For example, BEM allows calculation of induced charge distribution while the DDA allows exact physical modeling of fabricated structures. This dissertation utilizes the DDA to predict nanometer resolution electron energy loss distribution in nanoparticle excitation due to the ease of implementation of an electron source, availability of an open source code, and compatibility with computational methods used for optical excitations in this dissertation.

Modeling of the electron interactions with matter through EELS was done in two ways. First, a perfect shape most closely resembling the structure was modeled. This method allowed determination of specific excitation modes due to symmetry in the structure, comparison to previous studies in the literature, and comparison to other light excitation methods. Second, the exact dimensions of the fabricated structure was converted into a cubic grid of dipoles for DDA simulation. In this case, the fabricated structures experimental spectra could more closely be compared to computational methods.

To begin, shapes were simulated without fabrication imperfections to understand decomposition of results. A perfect disk, ellipse, and ring shaped nanoparticles were simulated to better understand electron energy loss spectra and experimental data. Disks were simulated to compare with results from the literature while the ellipse and ring simulations were performed for compari-

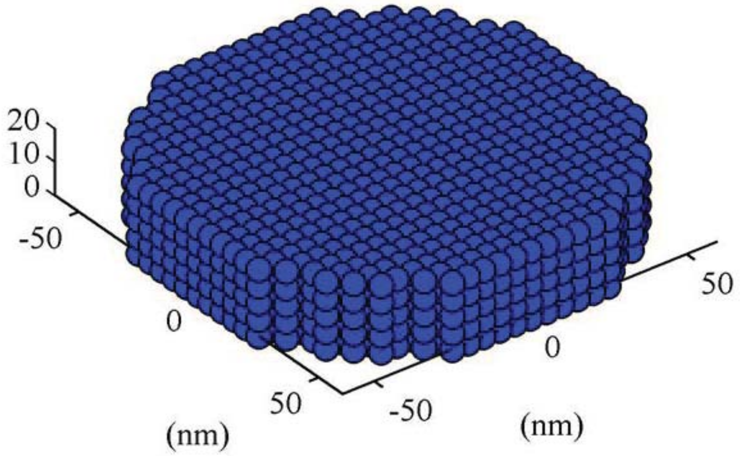

Figure 8.3: Dipole discretization of nanodisk of 60 nm radius, 20 nm thickness, and a 5 nm dipole spacing.

son to the work done for this dissertation (see Fig. 8.3).

8.2.2.1 Disk

A perfect disk with a radius of 60 nm was discretized into dipoles with an inter-dipole spacing of 5 nm was simulated. Varying thicknesses were simulated by changing the number of dipole layers from a single layer to five layers with the largest thickness of 20 nm shown in Figure 8.3. This inter-dipole spacing corresponds to approximately $\lambda/100$ and was chosen to balance computation time and memory expense with converged results.

Electron energy loss spectra was taken at three discrete points on the disk, shown in Figure 8.4. Spectra were calculated at loss intensities from 1.142 to 4.1 eV incremented by 0.0305 eV. The figure shows loss in units of energy (eV) and wavelength (nm) for convenience. Due to the rotational symmetry of the disk about the z axis, i.e. along the axis of incident electrons, the discretized points were independent of the polar (θ) coordinate. To prevent divergent results, incident electron points had to be chosen to correspond to grid points centered between simulated dipole locations. The three incident electron points in nanometers were at (2.5, 2.5), (2.5, 32.5), and (2.5, 57.5) corresponding to the center (blue), half radius (red), and edge (green), respectively.

Two resonant modes were observed in the loss spectra taken at the three specific impact

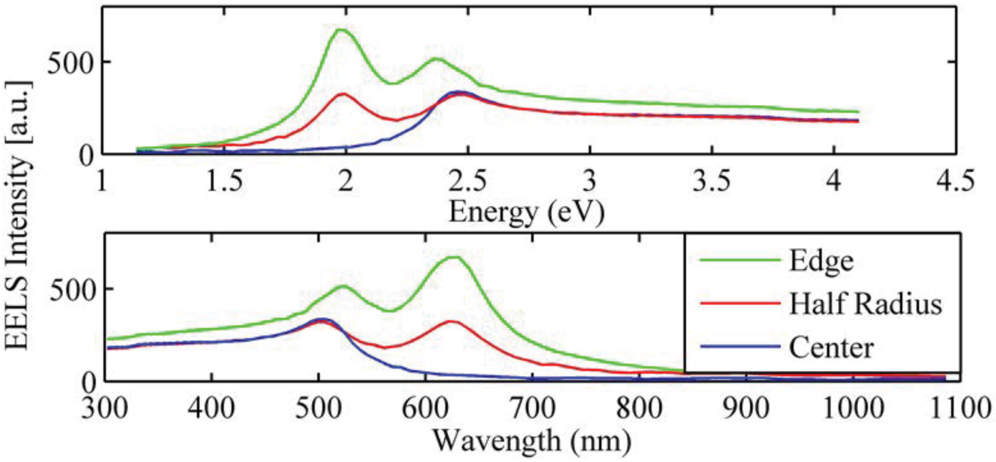

Figure 8.4: Electron energy loss spectra for three specific points on the disk. The spectra correspond to an incident electron beam at the center (blue), half the radius (red), and the edge (green) of the ring.

points from Figure 8.4. The first mode occurred at 1.996 eV (631 nm) for the edge (green) and half radius (red). This mode corresponded to the dipole plasmon mode that is excited when the same particle is irradiated with light of the same energy [113]. A report for disks of similar dimensions (radius of 65 nm and thickness of 33 nm) indicated an optical resonance at approximately 610 nm [121]. The second resonance mode was found to be centered at 2.38 eV (521 nm) for the edge (green) and 2.453 eV (506 nm) for the half radius (red) and center (blue).

To determine the spatial distribution of the calculated modes, a mapping was performed at each of the two loss peaks. To generate the maps, the electron beam was taken across every half-grid point over the surface and 10 nm beyond the disk edge. It was observed that simulated mappings were dependent on the incident beam location. Electrons incident exactly on simulated dipole locations gave divergent results. To compensate for this effect, electron incident locations were chosen at locations corresponding to half dipole spacings. At each incident electron point, the loss intensity was calculated at the specific energy value corresponding to a given plasmon mode. Results of the simulations are shown in Figure 8.5 for a loss of (a) 1.996 eV and (b) 2.453 eV.

Results revealed that the lowest energy mode in (a) corresponded to an excitation along the edge of the ring. An incident electron beam on the edge of the disk caused a buildup of positive charge around the impact point. This in turn caused a negative charge buildup on the opposite side

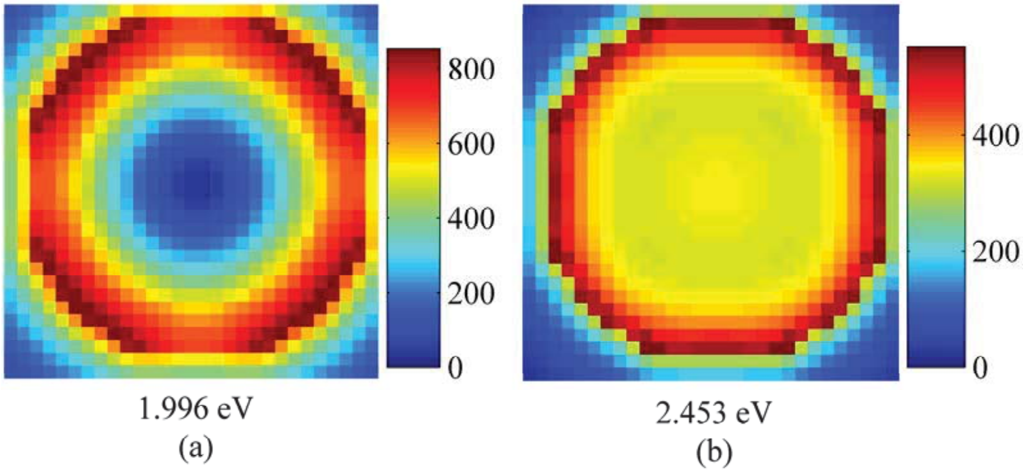

Figure 8.5: Electron energy loss mapping at two specific loss values of (a) 1.996 and (b) 2.435 eV.

of the disk. This charge distribution was that of a dipole induced on the disk. This excitation mode is also observed in disks illuminated with polarized photons. Modes that can be excited with light have been denoted as 'bright' modes in the literature [113].

The highest energy mode in (b) displays an edge excitation, but also corresponds to a center resonance mode. This type of excitation has been called a 'dark' or 'breathing' mode due to the inability of an incident light wave to couple efficiently and cause the plasmon oscillation [113]. Coulombic interactions between the incident electrons in the center of the disk and the nanostructure created a charge distribution with negative charge along the entire edge and positive in the center for the breathing mode with the electron beam positioned at the center of the disk. Such a distribution is not possible with incident photons. However, it has been shown that these dark modes can be excited by incident photons with a system of non-contacting nanostructures. An excited 'bright' mode, such as a dipole excitation, can decay and excite a 'dark' mode in a neighboring particle [109].

Disk thickness changes were also considered to ascertain the effect of nanostructure dimensions on plasmon resonance with electron excitation. For consistency, disk radius and inter-dipole spacing remained the same with only the z dimension varying. Due to the discretization scheme of 5 nm, thicknesses of 20, 15, 10, 5, and 0 nm (single dipole layer) were considered. Two observations were made when disk thickness was changed. First, a blue-shifting of the resonance

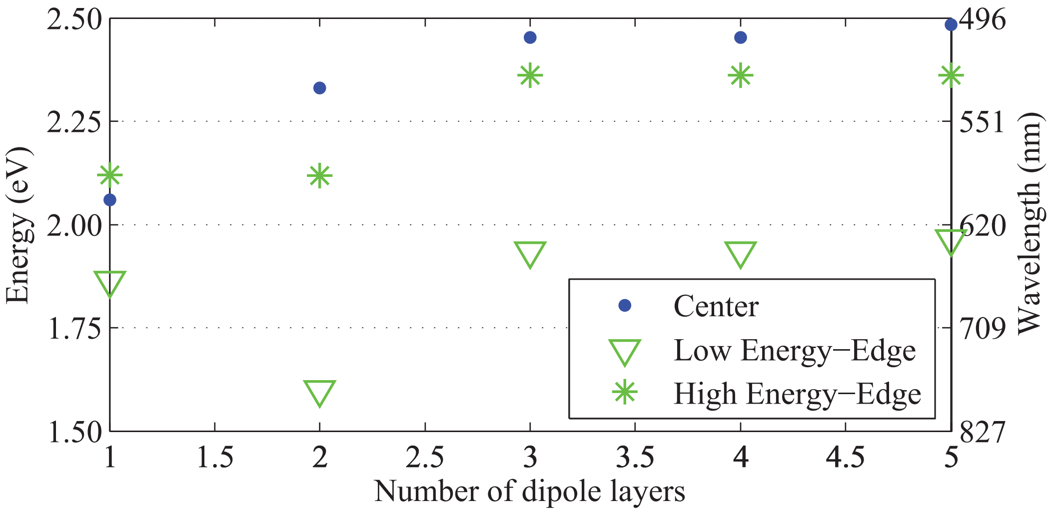

Figure 8.6: Plot illustrating shifting of plasmon mode energy (left y-axis) and wavelength (right y-axis) as a function of the number of dipole layers (x-axis) for the height of the disk. Plot shows the resonance mode for the center impact point (blue-circle), the highest energy edge impact point (greed-star), and the lowest energy edge impact point (green-triangle).

energy was seen as thickness (number of dipole layers) was increased. Second, artifacts due to discretization become more evident in EELS mappings at thinner disks with fewer dipole layers.

Spectral shifting of the resonance modes for increasing disk thickness are shown in Figure 8.6. The two resonance modes observed in Figure 8.4 were shown to generally blue shift as the number of dipole layers in the height discretization is increased. Each dipole layer was spaced 5 nm apart giving thicknesses for the disk of 0, 5, 10, 15, and 20 nm for the 1, 2, 3, 4, and 5 dipole layers, respectively. The dipole plasmon mode excited near the edge of the disk (green-dotted) was observed to initially redshift, but then blueshift with successive dipole layers. The higher energy mode appearing between 2 and 2.5 eV are shown for both the edge impact point (green-solid) and center impact point (blue-solid). This mode, having a zero net dipole moment, can only be excited with incident photons using Fano resonances.

The effect of discretization on the spatial EELS maps is illustrated in Figure 8.7 for a 60 nm radius disk with a single dipole thickness. The breathing, ’dark’ mode excited in the center of the disk was more clearly shown for the single dipole thick ring shown in (b) for a loss energy of 2.06 eV. However, the dipole plasmon mode excited at the edge (shown in the mapping in (a)

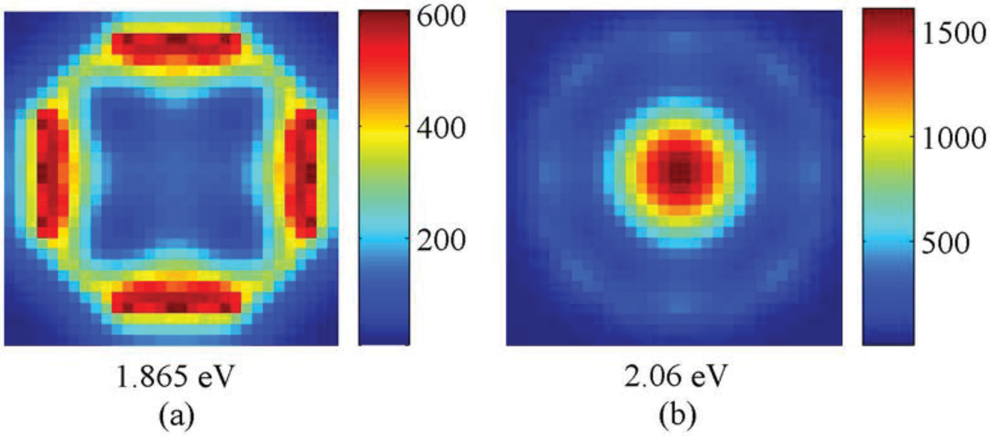

1.865 eV
(a)

2.06 eV
(b)

Figure 8.7: Electron energy loss mapping for a single dipole thick ring of 60 nm radius at two specific loss values of (a) 1.865 and (b) 2.06 eV.

with loss energy of 1.865) indicated non-symmetry in the results. This was due to the square grid discretization of a circular shape. The dipoles on the horizontal and vertical edges gave a smooth, straight edge while the diagonal edges had a staircase profile. A finer discretization with decreased dipole spacing could help with aliasing, but would require larger computational and memory costs. A balance between computation costs and converged spectra was used to give consistent results with simulations that could be completed on the available hardware.

The disk simulated in this section indicated that the EELS calculations was consistent with response with both optical and electron excitation reported in the literature. ’Bright’ dipole plasmon resonance and a ’dark’ plasmon breathing mode were predicted using the discrete dipole approximation. More complex morphologies were considered next to determine how plasmon modes shift and spatial distribution of the excited modes. Corresponding data helped to elucidate how nanostructures ccould be designed to produce spectral response to incident light. This would allow manipulation of optical properties at a surface for lithographed structures or for bulk material with dispersed nanomaterials.

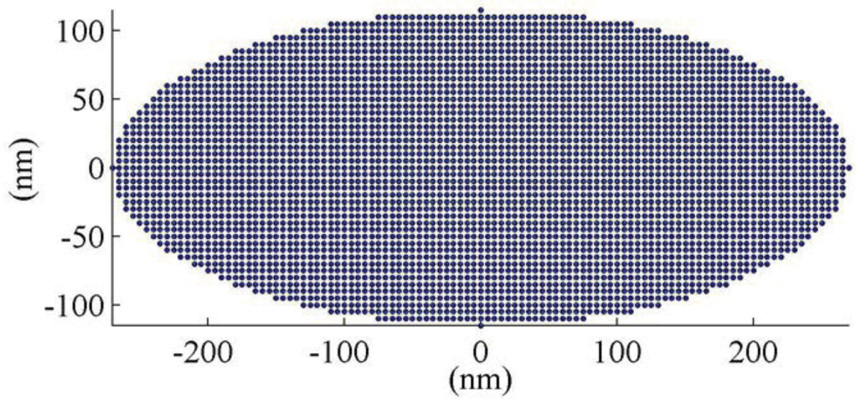

Figure 8.8: Discretization of an ellipse with horizontal (x-axis) radius of 270 nm and vertical (y-axis) radius of 115 nm with dipole spacing of 5 nm.

8.2.2.2 Ellipse

An ellipse with semi major (horizontal) and minor (vertical) radii of 270 and 115 nm, respectively, was discretized using dipoles with a 5 nm spacing and a height with a single dipole thickness as shown in Figure 8.8. Even though the discretization was only a single dipole layer thick, the ratio of radius to dipole spacing was sufficient to avoid artifacts from the grid. Due to the decreased symmetry of the ellipse compared to the disk, four points were chosen as impact points to obtain the EELS intensity plot to determine the locations of excitation modes.

Energy loss spectra for the ellipse at four specific impact points is shown in Figure 8.9. Chosen impact points included the center (blue), half-radius for the x-axis (red), half-radius for the y-axis (green), and the x-axis edge (pink). Loss energies simulated for each impact point ranged from 1 to 3.1 eV in 0.0105 eV increments. Spectra showed several resonance peaks located at energies of 1.00, 1.20, 1.425, 1.55, 1.68 1.855, and 2.08 eV. To ascertain spatial distribution of how each mode was distributed across the elliptical particle, EELS mappings were done at each energy listed above.

Energy Mappings across the spatial region of the ellipse wer performed at (a) 1.00, (b) 1.20, (c) 1.425, (d) 1.55, (e) 1.68 (f) 1.855, and (g) 2.08 eV energy loss values as shown in Figure 8.10. Each energy value corresponded to the observed plasmon modes in the full loss spectra from Figure 8.9. Three types of plasmon modes were observed from the spatial mappings. These

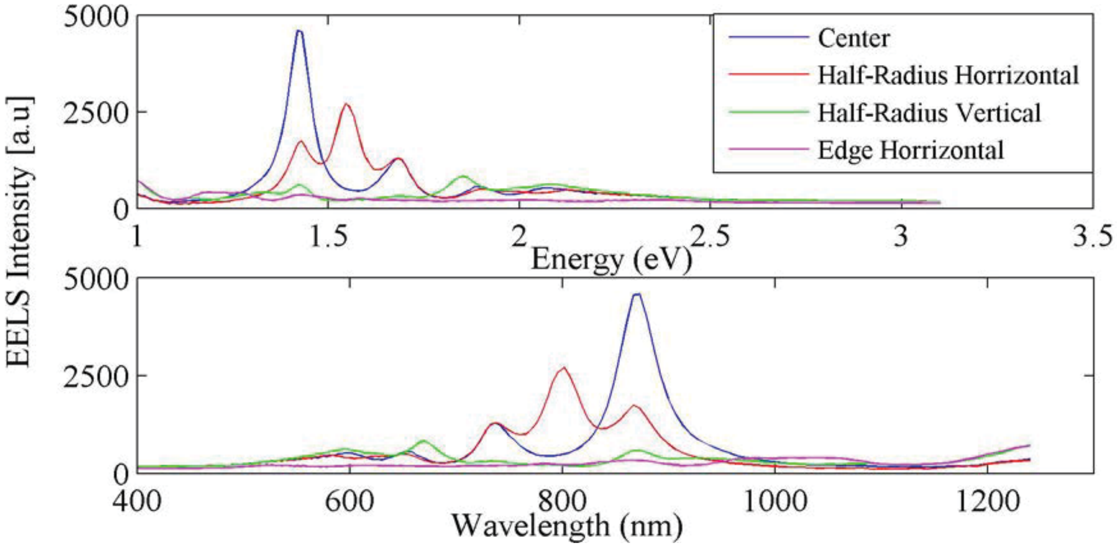

Figure 8.9: Energy loss spectra for the perfect ellipse showing four impact points including the center (blue), half-radius for the x-axis (red), half-radius for the y-axis (green), and the x-axis edge (pink).

included ’bright’ mode, ’dark’ mode, and hybrid modes. ’Bright’ modes included (a) and (b) and corresponded to modes easily excited by incident photons. The ’dark’ mode included (c), had a net zero dipole moment, and did not have a corresponding photon excitation. The hybrid modes ((d) through (g)) were not ’dark’ by definition such that they did possess a net dipole moment, but would not couple well to incident photons.

8.2.2.3 Ring

A ring with an inner radius of 60 nm, wall thickness of 20 nm, and a height of 25 nm (6 dipole layers) was discretized using dipoles with a 5 nm spacing as shown in Figure 8.11. Three impact points were chosen to obtain the EELS intensity spectra due to the symmetry of the ring. Two points were chosen along the x-axis in the center and outside edge of the ring wall while the third point was chosen at the center of the wall along the diagonal. The third point was chosen to determine how much the discretization scheme effected the loss spectra.

Results of the loss spectra from the three indicated impact points are shown in Figure 8.12. Loss energies ranged from 1.124 to 4.10 eV in increments of 0.0415 eV. Three resonance modes were observed in each of the impact points. These modes were found to be at energies

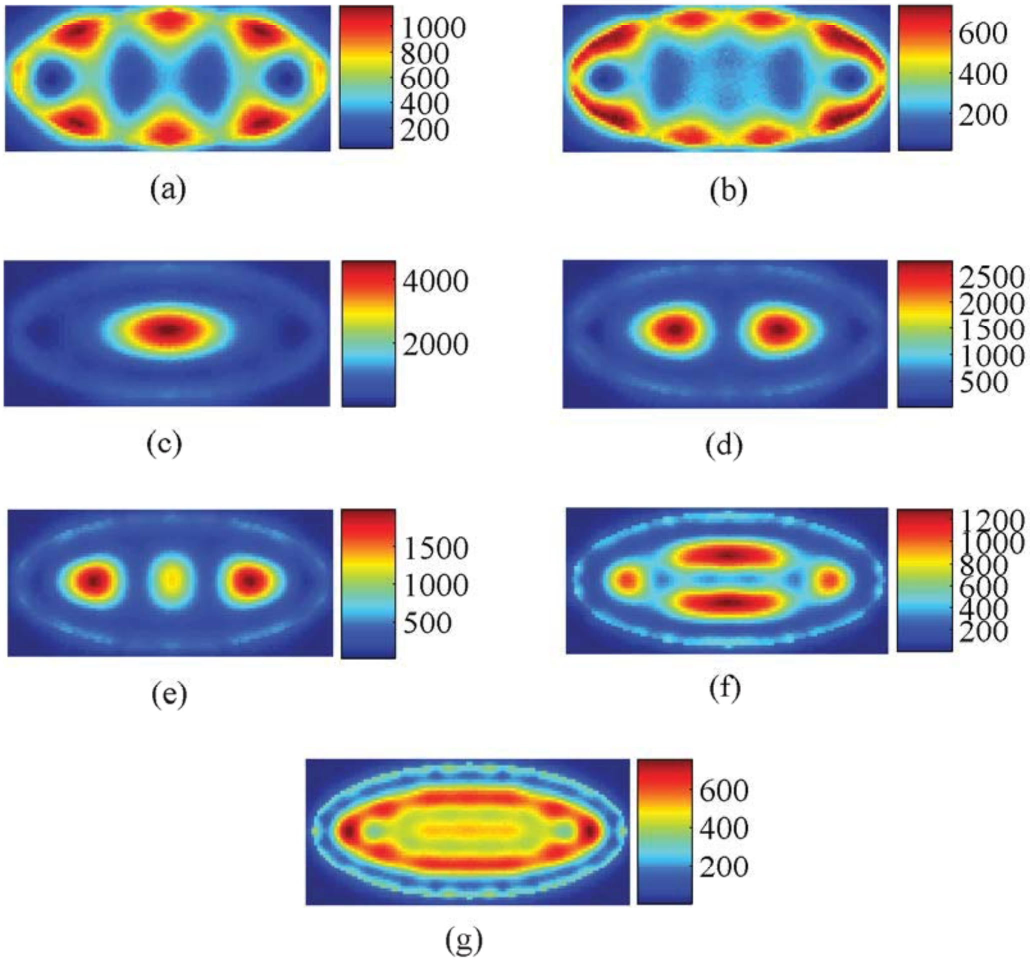

(a) (b) (c) (d) (e) (f) (g)

Figure 8.10: Simulated EELS mappings over the entire ellipse at specific energy loss values of (a) 1.00, (b) 1.20, (c) 1.425, (d) 1.55, (e) 1.68 (f) 1.855, and (g) 2.08 eV.

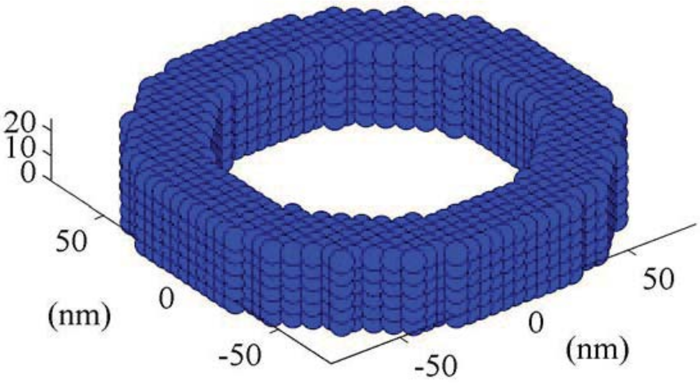

Figure 8.11: Discretization of an ring with inner radius of 60 nm, wall thickness of 20 nm, height of 25 nm with dipole spacing of 5 nm.

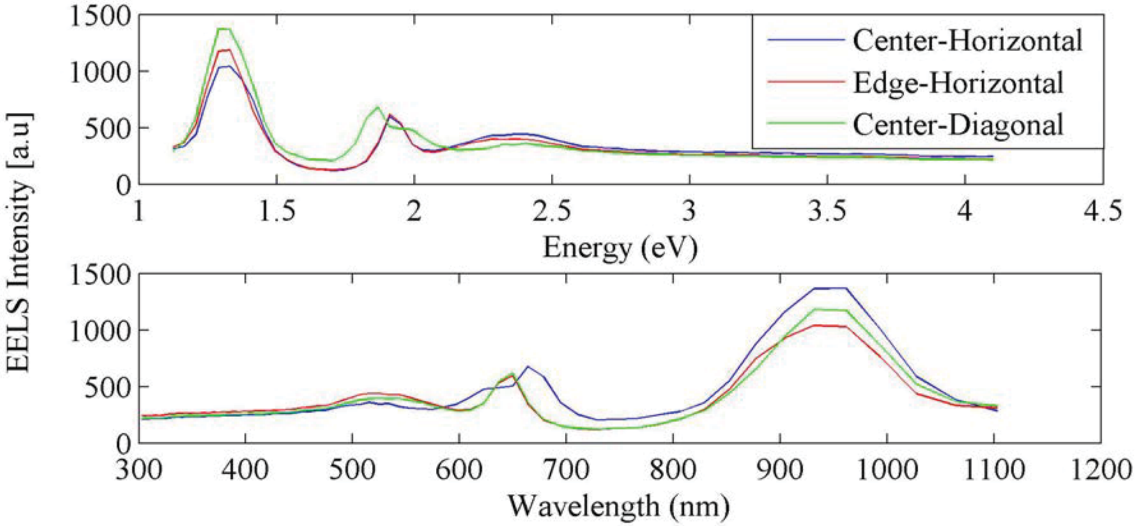

Figure 8.12: Electron energy loss spectra for the nanoring at three impact points. These points correspond to the center of the wall along the x-axis (blue), the outside edge of the wall along the x-axis (red), and the center of the wall along the line x=y (green).

(wavelengths) of 1.30 (954), approximately 1.90 (653), and 2.36 eV (525 nm). The middle energy resonance had two different energy values for the electron trajectory in the center of the wall for the horizontal (blue) and diagonal locations (green). The value of 1.90 eV was chosen between the two modal values of 1.87 and 1.91 eV for the green and blue spectra, respectively. Each of the three observed modes were chosen to calculate the spatial mapping for a specific energy loss value.

Spatial mapping for the three resonance modes located at (a) 1.30, (b) 1.90, and (c) 2.36 eV are shown in Figure 8.13. It has been well documented that nanorings of a similar size produce two plasmon resonance modes when excited by incident, polarized photons [77]. These two modes result from two different charge distributions in the dipole scheme on the ring walls. The first is the lower energy resonance called the anti-symmetric mode where each wall of the ring has a dipole with dipole moment pointed along the direction of polarization. The second is the higher energy resonance called the symmetric mode where the positive charge and negative charge separate onto opposite walls with a dipole moment pointing in the direction of the incident polarization. It has been observed for rings in the quasistatic approximation, that is much, much smaller than the incident wavelength of light, that an increased aspect ratio (wall diagonal to inner radius) results

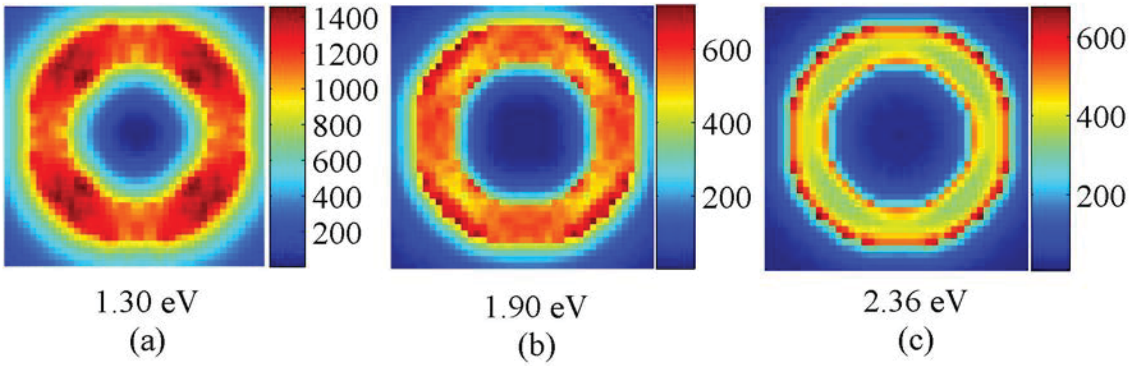

Figure 8.13: Electron energy loss mapping across the entire spatial region of the ring at specific energy values of (a) 1.30, (b) 1.90, and (c) 2.36 eV.

in blue shifting of the symmetric resonance mode [122]. However, the anti-symmetric mode does not significantly shift with changing ring dimensions.

Based upon experimental and theoretical treatment of optically excited rings, two of the modes observed in Figure 8.12 were accounted for. According to [122], the anti-symmetric mode appears at approximately 2.4 eV (517 nm), which is 0.04 eV larger than the mode predicted in this work with electron excitation. This mode corresponded to (c) in Figure 8.13. Considering the spatial mapping in (c), the energy lost from the incident electrons appeared to be concentrated at the inner and outer edges of the ring wall. Given the incident electrons were negatively charged, without loss of generality this would induce a positive charge on the outer wall giving a negative charge on the inner wall. This charge distribution was analogous to the anti-symmetric mode excited by an incident photon.

Similarly, a recent report of symmetric plasmon mode location indicates that a ring with an aspect ratio of 0.534, as simulated in this section, would have a resonance at approximately 1.24 eV (1000 nm) [77]. This value was 0.06 eV smaller than the predicted EELS resonance in this work for (a) in Figure 8.13. The spatial distribution of (a) indicated energy loss was concentrated along the interior of the ring wall. Excitation at a specific point on the ring would induce a positive charge distribution around the point of impact leaving a negative distribution on the opposing wall. This distribution was consistent with the symmetric plasmon mode induced with incident photons of the same energy.

The third mode in Figure 8.13 (b) was not observed with photon excitation. This indicated it was a 'dark' or breathing mode that does not couple well to photons. The spatial distribution in (b) appeared equally distributed along the wall thickness. This indicated each wall would possess a positive charge in the center of the wall with negative charge at the inner and outer wall edges. Again, such a charge distribution is not possible with incident photons.

MATLAB was used to extract the cubic grid of dipoles for the exact fabricated structure. The HAADF image obtained using scanning transmission electron microscopy (STEM) as was shown in Figure 8.2 was saved as a tiff image. The image was imported into MATLAB which converted the image to a 1024x1024 matrix with each pixel given a value from 0 to 255 based on the intensity of the gray scale image. Then, each pixel that had a magnitude larger than 50 was assigned as a dipole. Interdipole spacing was changed by skipping a set amount of dipoles each time. Figure 8.14 shows associated discretization of the actual fabricated nanoring. In this case, each pixel was 0.694 nm. Inter dipole spacing was set to 5.55 nm by selecting every eighth pixel. Identified in the dipole discretization figure are three specific points on the ring interior where the simulated electron beam was incident for the EELS calculation.

Spectra for energy loss was calculated for three specific impact points in the ring interior. Spectra was calculated with an incident electron beam accelerated with 120 kV and the intensity of electrons that lose a specific amount of energy is shown in Figure 8.15. Each colored line in the spectra corresponded to a different impact point indicated by the colored dot in Figure 8.14. Loss spectra were calculated for energies from 1.15 to 4.1 eV in 0.0305 eV increments. These energies corresponded to wavelengths from 1,086 to 302 nm. The spectra indicated one major resonance peak for points 1 and 3 situated in the middle of the thicker ring sides. The spectra from the second incident point located in the center of one of the smaller wall thicknesses gave two resonance peaks. To understand the near-field response of the ring to these incident electron energy losses, a mapping of electron energy loss intensity at specific energy values was done over the entire surface of the ring.

Energy mappings at the specific energy values of (a) 2.00 eV and (b) 2.37 eV are shown in

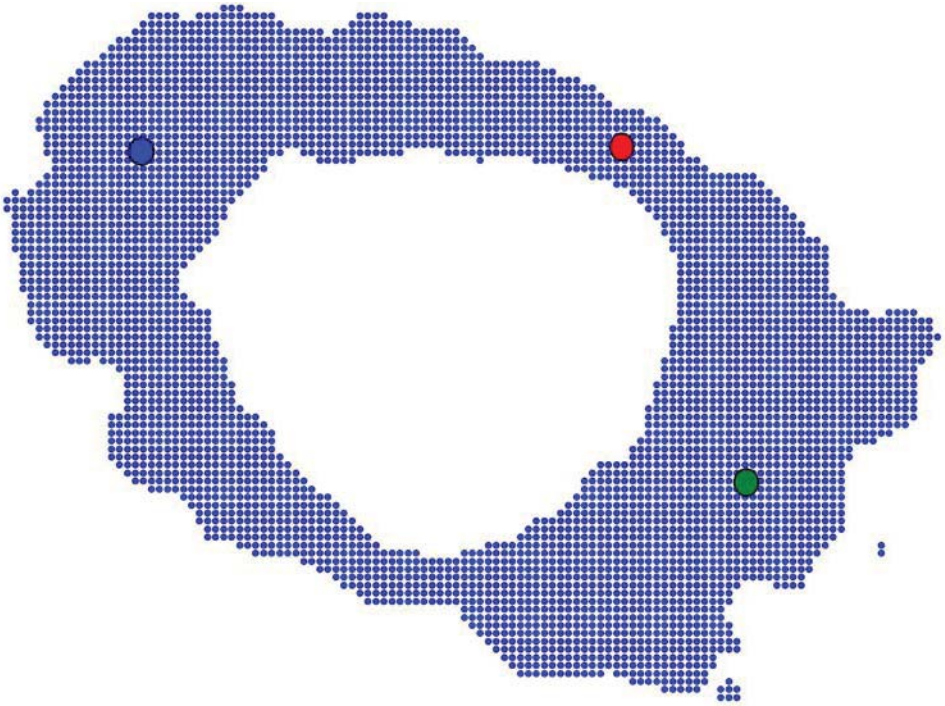

Figure 8.14: Dipole discretization of nanoring from the HAADF image.

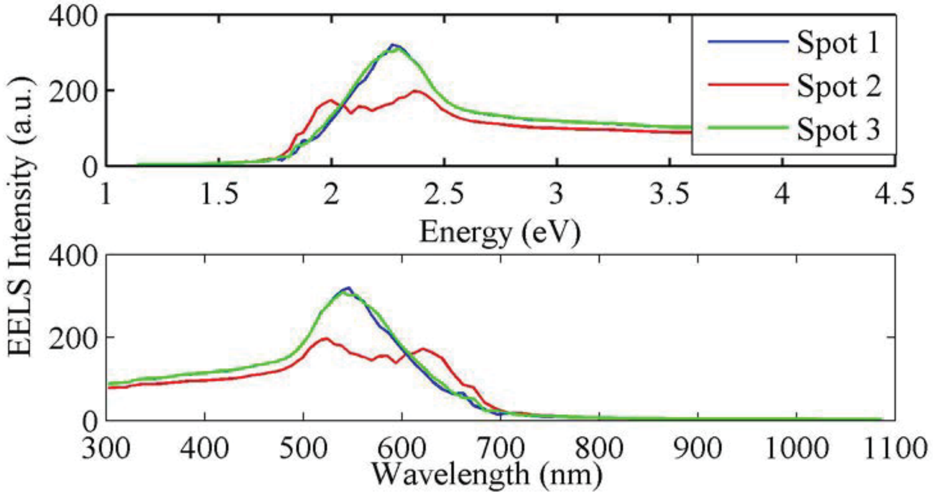

Figure 8.15: Electron energy loss spectra from three select point on the nanoring. Specific points are identified in Figure 8.14 with the respective colored dots.

Figure 8.16. Intensity of energy loss was given by the color gradient with a scale from 0 to 340. These two images indicated where on the structure incident electrons lose energy through plasmon absorption by the ring. In (a), the thicker ring wall exhibited increased loss intensity along the outer edge of the walls while the thinner ring walls showed an increased loss in the center of the wall. In (b), the opposite was true where the thicker (thinner) wall showed an increased loss along the center (edge) of the wall.

To understand what each mode corresponded to, consider first excitation with a photon source. Since the diameter of the ring along the long axis was approximately 600 nm, the size of the ring was appreciable to the wavelength corresponding to the plasmon energy. As a result, quasi static approximations for energy shifting of plasmons modes became more complicated. Dynamic depolarization from phase retardation across the ring and spontaneous emission of light from excited electron hole pairs causes addition spectral shifting in photon excited plasmon modes. As a result, it is presumed that the increased loss intensity for incident electrons along the edge of the ring corresponds to ’bright’, dipolar plasmon excitation associated with photon excitation. In contrast, the excitation in the center seen in (b) was associated with ’dark’ plasmon modes. Due to the relatively large size of the ring wall, it was not suspected that symmetric and anti-symmetric modes were observed as was seen previously with perfect rings.

8.2.3 Experimental Results

Electron energy loss spectroscopy (EELS) was obtained using a Tecnai G2 F20-TWIN (TF20) scanning transmission electron microscope (STEM) from FEI located in the Materials Characterization Laboratory at the Nano Institute. The TEM was equipped with a GATAN monochromator to separate transmitted electrons of varying energy levels with 0.05 eV resolution for EELS analysis. Incident electron energy was set by the accelerating voltage of 120 kV in the TEM. The detector determined the intensity of transmitted electrons that lost a particular amount of energy that was absorbed by the nanostructure through, or by which they passed. The entire spectra of energy loss was determined at a specific point on or near the sample and the beam was scanned in

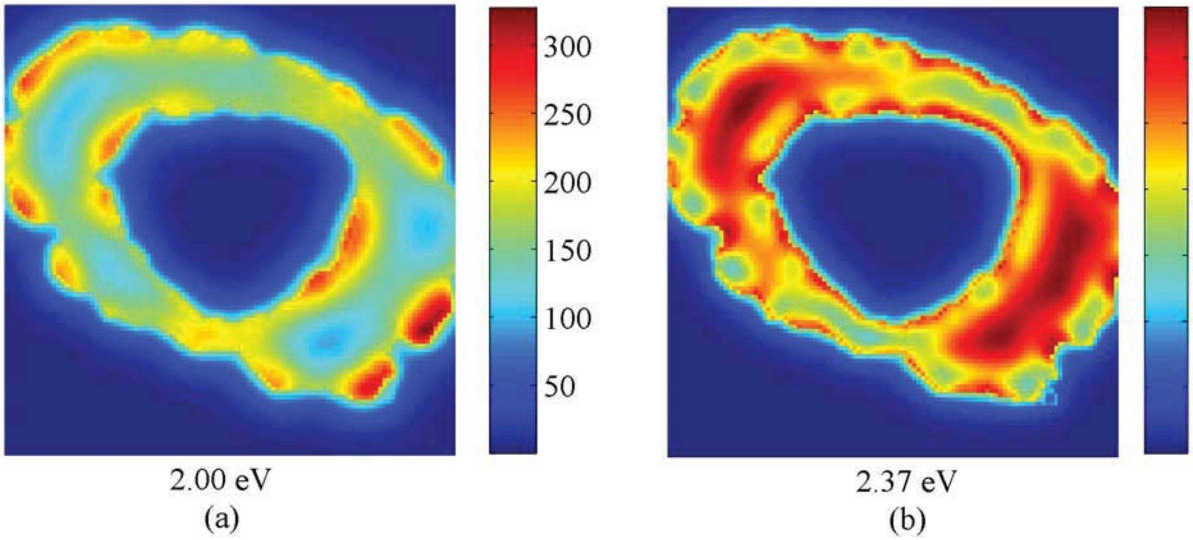

Figure 8.16: Electron energy loss spectra mapping from two specific energy values over the entire surface of the ring.

lines or areas to obtain spectra at any desired location or combination of locations on the sample. This allows mappings to be done at specific energy values to obtain sub-nanometer resolution of specific plasmon modes supported on the structure.

One issue when performing EELS was that carbon buildup occurred on the substrate when incident electron beams STEM were focused on a single point for an extended period of time. This carbon collection was a result of adventitious carbon on the surface from the air. The focused beam caused a buildup of this carbon and obscured results over time. It was observed that carbon buildup would occur within approximately 5 seconds after the beam location was chosen. This quickly dropped loss intensity by half and resulted in noisy EELS spectra that was difficult to interpret. To reduce the carbon buildup, the sample was treated with an oxygen plasma for 18 seconds. After plasma treatment, the sample was placed in the TEM for EELS measurements and it was observed that no discernible intensity drop in the spectra occurred during the collection of data.

Obtaining resonance peaks in experimental data can be obscured for energy below 5 eV due to the inherent zero loss peak (ZLP). The zero loss peak is caused by inelastic scattering of

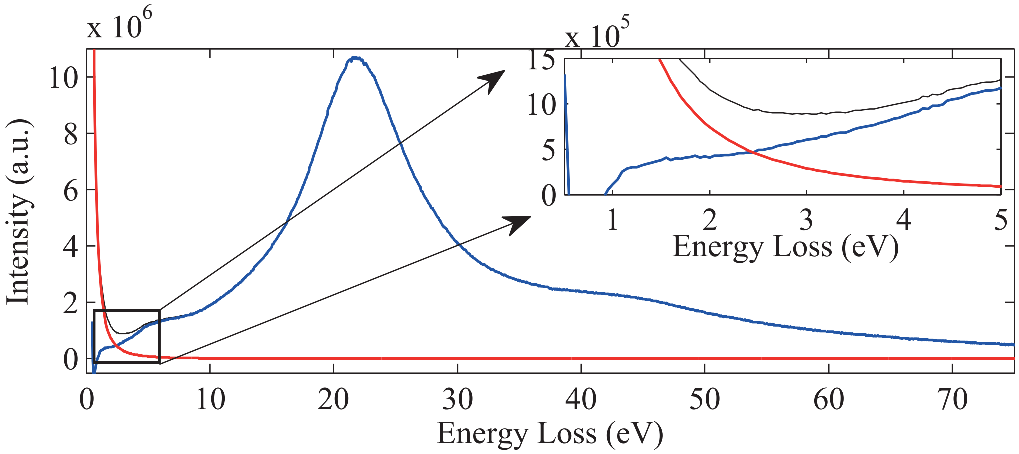

Figure 8.17: Electron energy loss spectroscopy of the 50 nm thick SiN membrane. Shown is the full spectra (black), the zero loss background fit (red), and the extracted spectra with the background subtracted (blue). Inset shows region of interest for plasmonic activity below 5 eV.

the incident electrons and small, random losses of energy. The ZLP is observed even when no substrate is present and the electrons have no interactions with materials between the gun and the detector. Bandwidth of the ZLP extends into the region of interest for this work. In order to extract information about the observed plasmon resonances between 1 and 5 eV, the background spectra was subtracted. The difficulty in this process was that the magnitude of the ZLP can be more than 100,000 times larger than the plasmon peaks.

Energy loss spectra of the silicon nitride substrate is shown in Figure 8.17. Three main peaks were seen in the spectra located at 0, 5, and 22 eV. The zero loss peak located at 0 eV was the narrowest peak with a full width at half max (FWHM) of 0.95 eV. The difference in intensity between the zero loss peak at 0.5 eV and at the base 3 eV was 1.8×10^7 which was a 95.3% reduction in amplitude. This peak was present in all measured EELS spectra, regardless of the substrate. The second was observed at 5 eV as a shoulder on the lower energy leg of the 22 eV peak. This 5 eV (248 nm) peak corresponded to the band gap of SiN. This peak was high enough energy that it was not expected to convolute plasmon resonances. It is not clear what the exact contribution to the third peak at 22 eV was, but calcium and sodium give EELS peaks at 25 eV and 31 eV, respectively. This peak was not observed to obscure measured plasmon resonances.

Extraction of spectra and fitting of the background was done during post-processing using a variety of models. These include the reflected tail, power law, and polynomial fits. These models fit a function to the ZLP and subtract the fitted function from the entire spectra. The chosen model for the background ZLP was the built in power law fit. This choice gave the most consistent deconvolution of the background spectra. This is illustrated in Figure 8.17 with raw spectra (black), background fit (red), and extracted spectra (blue).

Line and area scans were taken over a portion or the entire nanostructure to probe how resonance shifted across different locations on the structure. Thermal drift of the stage can cause the structure to shift tens of nanometers after the image has been captured. As a result, choice of electron probe impact point could be completely off the sample if care was not taken when taking data. For line and area scans, a drift corrected profile was taken. After every five probe locations had acquired loss spectra, the scanning mode was activated to re-image the sample and correct for any drift that occurred.

Analysis of the line and area scans did not reveal extractable data due to experimental and sample considerations. For example, external factors were observed to cause shifts in the resulting spectra which obscured location of observed resonances. Small interferences such as the opening and closing of magnetically locking doors, loud voices, and spikes in wall power can cause shifting of 2 or less eV in the spectra. These small shifts can make the entire data void since a single background model for the zero loss peak is used. Observed shifts in acquired spectra revealed a destruction of the spectral features in most of the collected data.

Additionally, thickness variations in the sample made creation of surface maps problematic. Spatial intensity mappings are made by the maximum loss intensity observed in a particular energy window. When the beam was moved over the sample with a variation of thickness, a large reduction in intensity was observed. For example, EELS spectra collected in the center of a feature as opposed to the edge of the feature resulted in a drop in overall intensity by an order of magnitude. The large drop of intensity was also observed to make noise in the spectra more prevalent. Since energy location of a resonance is more telling of plasmonic behavior than intensity, single collected spectral locations with independent background models was preferred over collecting area maps.

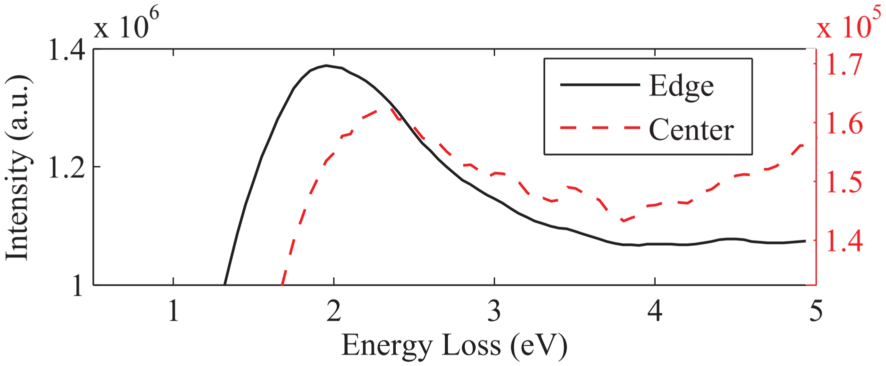

Figure 8.18: Extracted EELS spectra from a 75 nm diameter disk with impact points of the electron probe at the center (red-dotted) and edge (balck-solid).

8.2.3.1 Disk

Energy loss spectra was for an imperfect disk with a diameter of approximately 75 nm (as shown in Figure 8.18). This observed disk was not located at a position where lithography was performed indicating the gold deposited after liftoff. This indicated the structure was most like more spherical than disk shaped. Energy loss was taken at the edge and center of the disk corresponding to ’bright’ and ’dark’ modes, respectively. Spectra for the disk is shown for the edge (black-solid) and center (red-dashed) of the disk with the zero loss peak subtracted from the resulting spectra. Spectra are shown using a double y-axis to easily compare energy locations, since peak amplitude differences do not allow both plots to be on the same axis. It was observed that a single resonance peak was seen for each spectra with resonance maximum located at 2.35 (527 nm) and 1.95 eV (636 nm) for the center and edge impact points, respectively. This trend was consistent with disks with the center, ’breathing’ mode being a higher energy than the edge ’bright’ mode, the latter of which was also excited by incident photons [113].

A slightly elliptical disk shown in Figure 8.19 (with horizontal radius and vertical radii of 137 and 175 nm with a 2 nm Cr layer and 15 nm of Au on top) was examined with an incident electron probe in multiple locations using EELS to determine spatial modes that were supported on the surface. Figure 8.19 shows the disk with four impact point where EELS data were collected. These points corresponded to the center (1), half the radius (2), the edge (3) and on the substrate

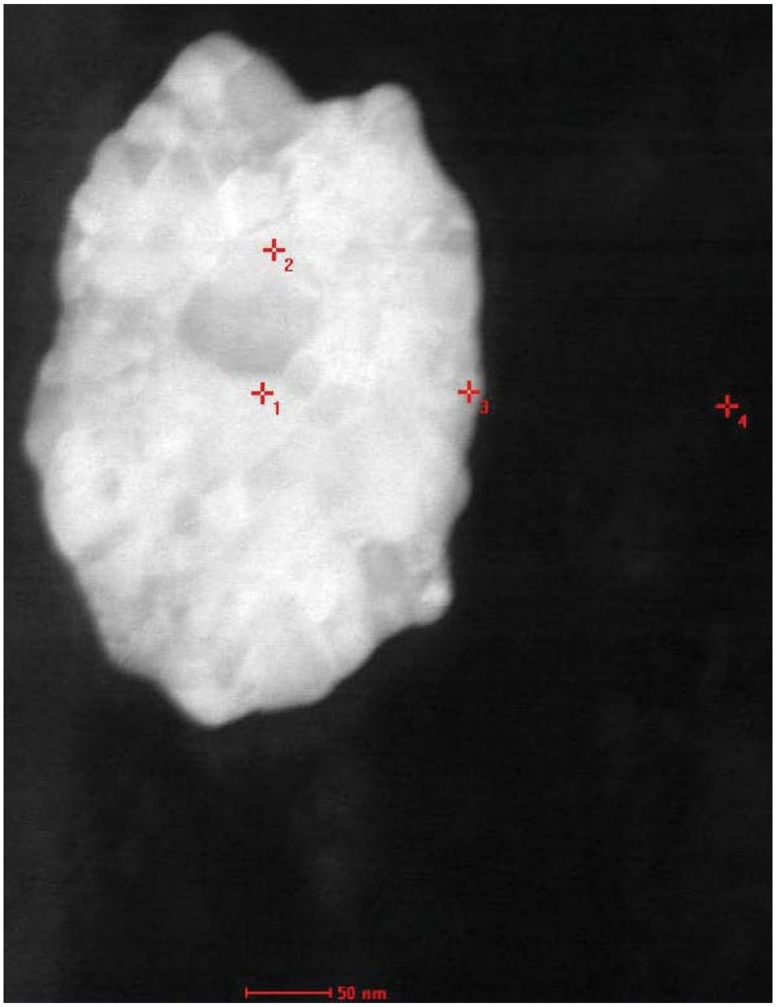

Figure 8.19: HAADF image of lithographed gold disk used for energy loss spectroscopy. Specific impact points to obtain spectra are shown in the figure.

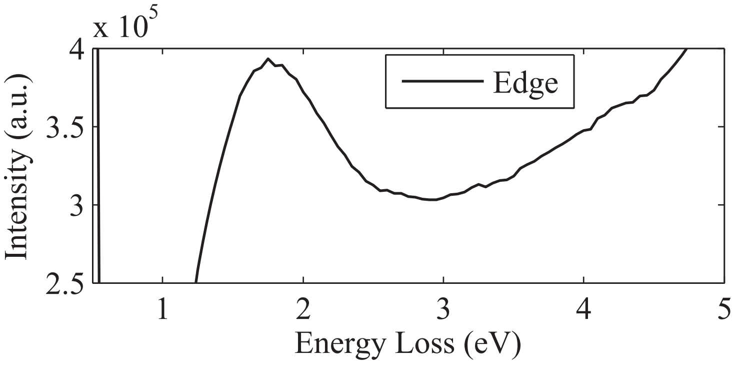

Figure 8.20: Extracted EELS spectra for the disk shown in Figure 8.19.

where no metal was present (4). One representative spectra is shown in Figure 8.20 for impact point 3 along the particle edge. Resonance locations for each impact point were found to be (point 1) 2.3 eV, (point 2) 1.1 and 2.1 eV, (point 3) 1.75 eV, and (point 4) no observed resonance. Energy loss spectra for point 4 was used in Figure 8.17 to show the effect of the SiN membrane without the presence of metal.

The observed resonances for the three impact points along the center, half-radius, and edge of the disk were not all observed to be located at the same energy value. The two resonance modes for the half radius (point 2) were blueshifted from the individual excited modes from the center (point 1) and edge (point 3). It was not clear if the observed resonances corresponded to the same, but shifted modes, or to a different mode entirely.

8.2.3.2 Ring

Energy loss spectra was taken from specific points on the fabricated gold nanoring structure that was shown in Figure 8.2. This same nanoring was modeled in Section 8.2.2.3 with experimental impact points the same as the simulated points. Specific impact points for the incident electron probe were along the center of the smaller and larger ring walls as well as the inner edge of the large wall from the ring previously shown in Figure 8.14. It was observed from Fig. 8.21 that a single resonance peak existed for each of the spectra. Peak locations were found to be 1.20 (1.033) and 1.45 (855 nm) eV for the edge and center of the larger wall thickness. The thin wall peak was observed to be approximately 1.35 (918 nm) eV.

Compared to the performed simulations, these experimental data were comparatively red shifted. However, redshifting was expected due to the presence of the substrate. The SiN substrate became polarized and acted against the restoring force of the induced charge distribution in the structure. This decreased the net energy of the plasmon modes. Simulations of smaller particles with fewer dipoles revealed that the effect of the SiN substrate shifted the dipole resonance as much as 10% (data not shown). Here, the simulated single plasmon resonance for the center of the thinner wall in vacuum from Figure 8.15 was predicted to be 2.00 eV (620 nm). A 10% redshift of

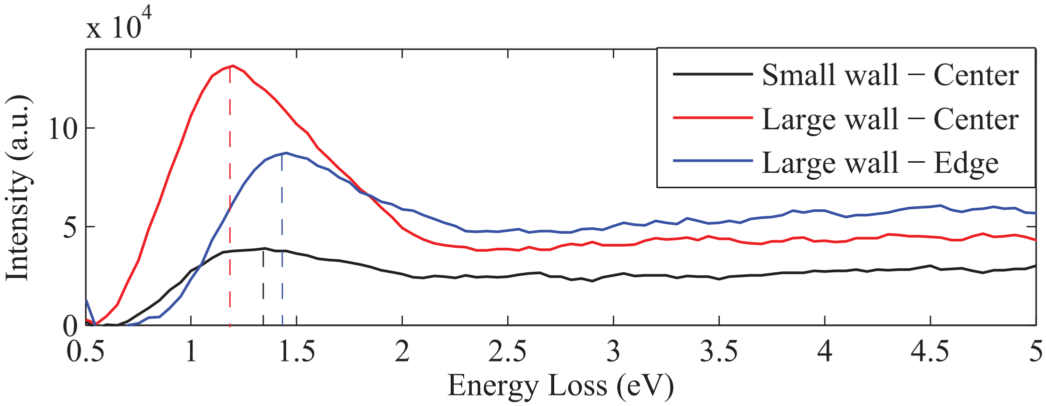

Figure 8.21: Extracted EELS spectra for three impact points of the ring shown in Figure 8.14.

the resonance due to the substrate would generate a plasmon peak at 1.80 eV, which did not fully explain the discrepancy between experiment and simulated plasmon resonance in EELS.

8.2.3.3 Ellipse

Electron energy loss spectroscopy was performed on the ellipse shown in Figure 8.22 with the indicated impact points labeled in the figure. The ellipse was measured to be approximately 230 nm across the short axis and 540 nm across the long axis. Impact points on the ellipse were chosen due to the rotational asymmetry of the structure. Contrast in the figure gave an indication of grain boundaries of the Au and variations in thickness. Brighter contrast suggested a thicker region owing to the imaging technique based off collection of scattered electrons. Impact points were chosen to correspond to the center (point 2), edges (points 1 and 3), and half radii (points 4 and 5) of the ellipse.

Spectra for the indicated impact points showed two primary oscillation modes excited at different impact points. Select spectra for impact point 2 at the center (red-dotted) and point 4 at the half-radius (solid-black) are shown in Figure 8.23. These two spectra indicated two distinct resonance modes with a single excited mode for point 2 located at an energy of 2.35 eV (528 nm) and two modes visible for point 4 with energies of 1.15 eV (1078 nm) and 2.3 eV (539 nm). For the remaining spectra not shown, point 5 was observed to support two resonances located at 1.35 eV (918 nm) and 2.5 eV (496 nm). Note that these resonances were blue shifted from the

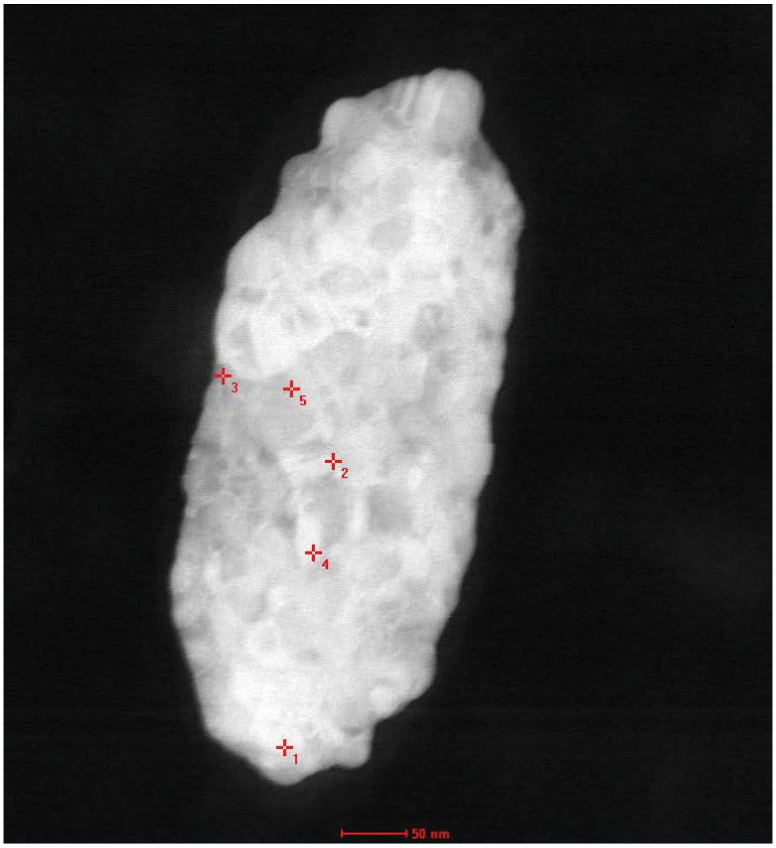

Figure 8.22: Scanning transmission electron micrograph of ellipse used for electron energy loss spectroscopy. Impact points of incident electron beam are labeled with 1 through 5.

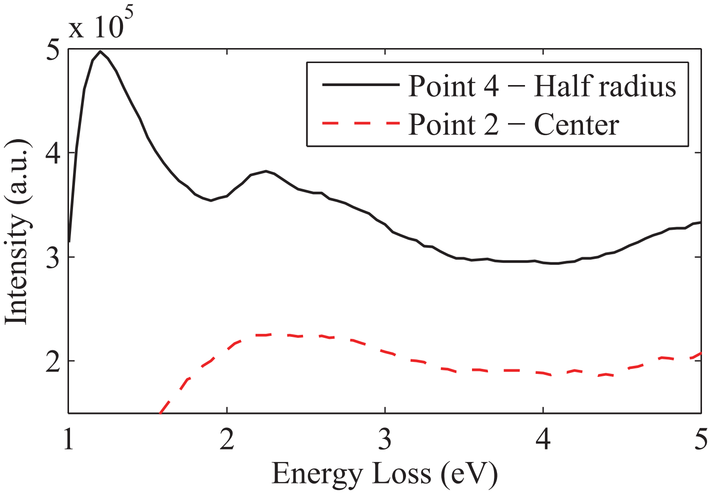

Figure 8.23: Extracted EELS spectra for select impact points indicated in Figure 8.22.

corresponding modes observed at point 4. This was consistent with plasmonic behavior in ellipses with incident photons. Light incident and polarized along the short axis produced a plasmon mode that was blueshifted as compared to polarization along the long axis [18].

Higher energy modes observed on this ellipse gave an indication of the electron oscillation that was supported on this specific structure. While these 'dark' modes were not excited efficiently with incident photons, near-field Fano resonances have been observed to allow broader absorption of photons through particle coupling. A 'bright' mode excited in one particular particle with incident photons can couple with the 'dark' mode of a close neighboring particle in order to enhance scattering and absorption of incident light not possible with a single, isolated structure.

Edge modes from impact points 1 and 3 were also observed to produce a resonance with behavior consistent with photon excitation. A single resonance was observed at both impact points with an energy of 1.3 eV (954 nm) for point 1 and 1.45 eV (855 nm) for point 3. A blueshift in the resonance for the short axis (excited at point 3 compared to the long axis excited at point 1) was consistent with photon excitation as explained in the previous paragraph. Analysis of EELS spectra for this elliptical particle provided information about local plasmonic behavior which corresponded directly to information about photonic excitation for the 'bright' modes excited along the edge of the particle.

8.2.4 Graphene Effects

Electron energy loss spectroscopy (EELS) was taken for multiple ellipses from the same lithographed area and compared when graphene was and was not present as a layer between the nanoparticle and the SiN membrane. This comparison was possible due to partial coverage of graphene on the sample before lithography was performed. The disks where EELS was collected are shown in Figure 7.10. Data were collected from ten different ellipses, five each from graphene and non-graphene situated particles. Spectra from the center and along the long edge were taken to give a comparison on the effect of graphene from two different types of plasmon modes. Data collected from the center of the ellipses corresponded to the 'dark' plasmon mode with a net zero

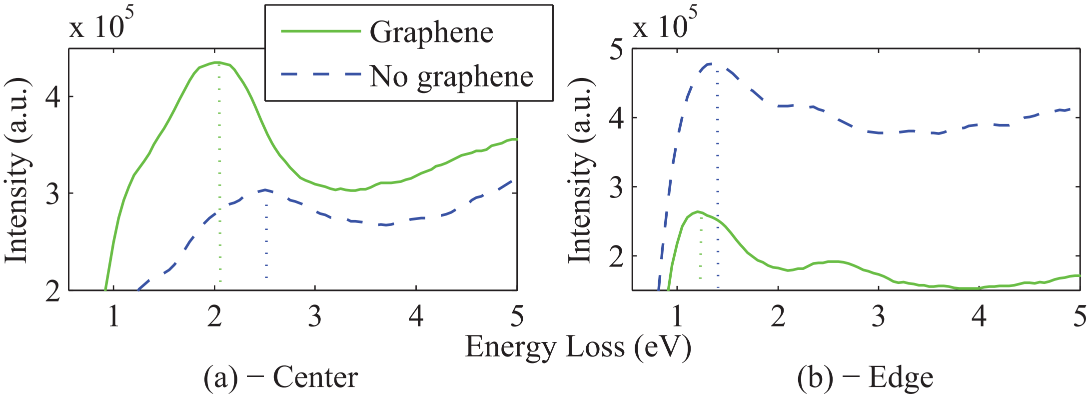

(a) − Center (b) − Edge

Figure 8.24: Extracted EELS spectra for an ellipse on graphene (solid-green) and off graphene (dotted-blue) with impact point at the (a) center and (b) long edge.

dipole moment and poor coupling to incident photons. Data collected from the long edge corresponded to the 'bright' mode which was the familiar plasmon mode seen in optical excitations.

Select spectra from the collected data for ellipses on (green-solid) and off (blue-dotted) graphene are shown in Figure 8.24. Impact points for the (a) center and (b) edge corresponded to 'dark' and 'bright' plasmon modes, respectively. Vertical dotted lines were added to help guide the eye. In (a) the 'dark' resonance mode was observed to redshift in the presence of graphene from a value of 2.45 to 2.05 eV. Full width at half max (FHWM) calculations were done on each spectra using the dip in the right leg of each spectra as the minimum. It was observed that the FWHM decreased in (a) from 1.10 to 0.95 eV. Similarly, a redshift of the 'bright' mode in (b) from 1.40 to 1.25 eV was observed when graphene was added. In contrast to the 'dark' mode, an increase in the bandwidth from 0.5 to 0.7 eV with the presence of graphene was measured. Data of each ellipse for 'dark' resonance energy and 'bright' resonance energy and FWHM with statistics are given in Table 8.1.

Data from the ellipses suggested that the presence of the graphene did affect the plasmon resonance energy location and bandwidth. The 'bright' plasmon mode showed a redshift in energy while the 'dark' mode showed a blueshift in energy due to the interaction of the graphene substrate. Data for the collected resonance energy and size distribution of the disks is shown in Table 8.1. Analysis of collected EELS data indicated that the 'dark' plasmon mode excited through incident

Table 8.1: Resonance energy location from EELS spectra collected from ellipses on and off graphene with impact point at center and the long edge of ellipse. Full width at half max for the edge mode is given in parentheses. Also given are long and short diameters of each ellipse. At the bottom are the average (μ) and standard deviations (σ).

	No-Graphene				Graphene			
	Spectra (eV) [Energy(FWHM)]		Size (nm)		Spectra (eV) [Energy(FWHM)]		Size (nm)	
	Center	Edge	Long	Short	Center	Edge	Long	Short
	2.35(0.95)	1.60(0.75)	544	230	2.05(0.95)	1.25(0.85)	550	200
	2.30(1.10)	1.35(0.60)	510	220	2.10(0.90)	1.25(0.70)	520	210
	2.25(1.05)	1.45(0.50)	545	235	2.15(1.05)	1.30(0.80)	550	220
	2.45(1.15)	1.35(0.55)	545	230	2.30(1.10)	1.25(0.75)	560	230
	2.45(1.10)	1.40(0.50)	555	220	2.35(1.10)	1.40(0.55)	560	230
μ	2.36(1.07)	1.43(0.58)	540	227	2.19(1.02)	1.29(0.73)	548	218

electron at the center was located at 2.36 eV (525 nm) with a sample standard deviation (σ) of 0.089 eV with graphene and 2.19 eV (566 nm) with a σ of 0.129 eV without graphene. This was a redshift of 0.17 eV (41 nm) which was 7.2% when the graphene was present. Similarly, the ’bright’ mode showed a redshift in resonance when graphene was present from 1.43 eV (867 nm) with a σ of 0.104 eV to 1.29 eV (961 nm) with a σ of 0.065 eV. While this mode was only redshifted by 0.14 eV giving a change of 9.8%, the wavelength shift was 94 nm owing to the inverse relationship between energy and wavelength.

Statistical analysis was completed with the data to perform hypothesis testing on the observed differences in means for energy and bandwidth values. First, analysis was completed for the edge mode where Welch’s t-test was performed to evaluate the null hypothesis, $H_0 : \mu_{\mathrm{G,E}} \neq \mu_{\mathrm{NoG,E}}$, where ’G’ and ’NoG’ represent graphene and no graphene samples and ’E’ stands for energy. The same test was also performed on the bandwidth means signified with a ’B’ instead of an ’E’. The variable for the test statistic used was defined as

$$t = \frac{\mu_1 - \mu_2}{[(\sigma_1^2 + \sigma_2^2)/n]^{1/2}} \tag{8.2.2}$$

where n is the number of observations. The calculated value for the test statistic was used to obtain a p-value which helped determine acceptance or rejection of the null hypothesis. For the energy value means and standard deviations, it was found that $t_{\mathrm{E}} = 2.55$. Using 6.7 degrees of freedom as determined by Welch's test, the p-value was determined to be 0.04 indicating that the probability that the null hypothesis should be accepted was 96%. The same treatment to test the null hypothesis for the bandwidth means, $H_0 : \mu_{\mathrm{G,B}} \neq \mu_{\mathrm{NoG,B}}$, indicated a p-value of 0.06. Within a confidence interval of 94%, the null hypotheses were accepted and the means were determined to be statistically different. Analysis of the center, 'dark' mode indicated that the energies of the resonance from ellipses on and off graphene were statistically different within a confidence interval of 95%. However, the bandwidth statistical analysis revealed that the null hypothesis must be rejected with a p-value of 0.37 suggesting there is no reason to believe the bandwidths are statistically different. Analysis of energy and bandwidth differences was only performed for the edge mode owing to the statistical similarities in the center mode bandwidth.

Redshifting of the observed modes were consistent with results from previous sections of this dissertation. For example, the 'bright' mode excited along the edge of the disk was found to be consistent with behavior of plasmon modes excited with incident photons. Introducing a non-vacuum medium around a plasmonic nanoparticle induced dipoles in the medium. These induced dipoles acted to damp to Coulombic restoring force from the plasmon oscillation, thus reducing the energy of the resonance mode. Increasing the value of the real component of refractive index has been demonstrated to cause greater redshifting of the plasmon energy as detailed in Chapter 6. The refractive index of SiN is approximately equal to 2 in the visible range while graphene has a real refractive index component of 3 [123]. However, the observed redshift in the EELS data was greater than expected based solely of refractive index effects.

Using results from Chapter 6, plasmon modes predictably shift with changing RI. Using the effective refractive index model from Equation 6.2.1, only a small change in RI was predicted. Using an overestimated graphene thickness of 1 nm at a wavelength of 500 nm, the effective RI with the presence of graphene increased from 1.500 to 1.501. Using Mie theory, this was predicted to give a redshift in the plasmon resonance of less than 1 nm. The observed shift in resonance from the EELS data was two orders of magnitude larger than the predicted amount based upon the effective medium approach.

It was suspected that the increased observed redshift was a result of the conductivity of the graphene film. As opposed to the medium simply becoming polarized when the plasmon oscillation occurs as described in Chapters 5 and 6, mobile electrons can flow along the graphene to effectively increase the induced polarization of the substrate. Graphene in this scenario behaved as a waveguide to transport electrons in response to the induced charge distribution of the nanostructure. Literature has reported plasmon resonance shifts of split ring resonators of 5-10% when graphene is added as a superstrate to the metal nanostructures [35]. Observed shift in this work were consistent with this report.

Additionally, excited (or ’hot’) electrons could transfer to the graphene as a decay route in addition to radiative and phonon decay. A description of hot electron transfer to graphene was given in Section 3.2 with reference to increased photocurrent in graphene decorated with plasmonic nanostructures. Hot electron transfer has been examined by consideration of bandwidth changes in plasmon resonance on and off graphene with a quartz substrate under photon excitation [124]. Ref. [124] showed the presence of the graphene caused a broadening of the plasmon peak using dark field spectroscopy and photoluminescence. This broadening indicates an additional damping mechanism for the decay of plasmon oscillation as hot electrons into the graphene.

Bandwidth of the plasmon resonance is effected by damping mechanisms. Contributions to a Lorentzian bandwidth can be separated by the superposition principle into linear sum where the total bandwidth is given as $\Gamma_{\text{tot}} = \sum \Gamma_i$. For particles with dimensions large enough where the incident light wave can no longer be treated as a uniform field, spontaneous emission of light must be considered. This radiative damping can be expressed as

$$\Gamma_{\text{Rad}} = 2\hbar\kappa V \tag{8.2.3}$$

where $\hbar$ is Plank’s constant, κ is a radiation damping coefficient, and V is the particle volume [125]. Assuming the ellipses are comparable to nanorods, κ was taken from the literature to be

4.0×10^{-7} fs^{-1}nm^{-3} [124]. Using the average values determined from Table 8.1 and using a thickness of 15 nm, the volume of the ellipses on and off graphene were 1.44×10^{6} nm^{3} and, 1.41×10^{6} nm^{3} respectively. Therefore, the radiative damping (Γ_{Rad}) of the plasmon resonance on and off graphene was calculated using Equation 8.2.3 to be 0.38 and 0.37 eV, respectively.

To determine validity of the observed experimental bandwidths, optical excitation simulations were performed to extract contributions from quasi static and radiative damping using single particle polarizability as described in Section 4.2. The quasi-static and modified long wavelength approximation (MLWA) polarizability models (Equation 4.2.2 and 4.2.5, respectively) were used with size values from Table 8.1 for the ellipses off graphene. A homogeneous background refractive index of 1.46 was used to match the simulated resonance with the experimental peak at 1.43 eV (867 nm). This value for RI matched intuition since the SiN substrate had an RI of 2 and vacuum had an RI of 1. Using the MLWA, the energy and FWHM of the plasmon peak were calculated to be 1.43 and 0.53, respectively. This was within experimental error to the observed bandwidth of 0.58 ± 0.10 eV from Table 8.1. It was expected that some additional damping was contributing to the observed plasmon peak as well as from the modeling assumption of a perfect ellipsoid particle. Using the quasi-static polarizability which did not include effects of radiative damping, a bandwidth of 0.23 eV was calculated. This gave a simulated contribution to radiative damping from the MLWA of 0.3 eV. Taking into account the assumptions used in the polarizability model of a point dipole, these results gave credence to the observed trends and relative contributions of radiative damping from emitted photons and quasi-static damping from intrinsic losses into phonons.

It was noted that intrinsic and radiative damping depend on the energy of the resonance. To determine the effect of plasmon shifting on the observed bandwidth, simulations were performed using the MLWA polarizability with the homogeneous RI adjusted to account for the observed shift. Since it was shown that an effective RI model with explicit modeling of graphene was ineffective to explain the observed resonance shift, RI was manually adjusted until the simulated spectra maxima was in line with EELS spectra for ellipses on graphene. This was done using the MWLA approximation with the same conditions for the simulations performed to assess relative contributions of radiation and quasi static damping in the previous paragraph. It was found that an RI of 1.63 resulted in the plasmon peak being located at a value of 1.29 eV (961 nm). The bandwidth of the plasmon peak for the quasi static and MLWA polarizabilities revealed the contributions to damping were Γ_{nRad}=0.22 eV and Γ_{Rad}=0.27 eV with a total bandwidth of 0.49 eV. The result of the plasmon shifting due to increased refractive index resulted in a net decrease in the plasmon bandwidth of 7.5%. This indicated the observed increase in bandwidth in the EELS spectra was not a result of the energy dependence on intrinsic and radiative decay.

Damping of the plasmon resonance due to the presence of graphene was used to determine the dephasing time constant from hot electron transfer. Total dephasing can be expressed as $T_2^{-1} = T_1^{-1} + T^{*-1}$ [125]. The terms T_1 and T_2 correspond to two inelastic decay of the plasmon mode and the plasmon dephasing time, respectvely. The time term T^* corresponds to pure elastic dephasing, which is neglected for further calculations. Obtaining time constants from line widths was done using the relations

$$T_{2,i} = 2\frac{\hbar}{\Gamma_i} \tag{8.2.4}$$

where i is the damping source. Broadening from the electron transfer was related to the electron transfer time by $T_{\mathrm{HE}} = 2\hbar/\Gamma_{\mathrm{HE}}$ [124]. Assuming the additional bandwidth from the graphene was due solely to HE transfer, Γ_{HE}=150 meV. This gave an electron transfer time of T_{HE} = 8.8 fs.

Efficiency of HE transfer as a decay route for plasmon excitation was evaluated from comparing the time constants in the different damping terms. This relation is given by

$$\beta = \frac{T_{\mathrm{HE}}^{-1}}{T_{\mathrm{nRad}}^{-1} + T_{\mathrm{Rad}}^{-1} + T_{\mathrm{HE}}^{-1}} \tag{8.2.5}$$

where 'Rad' and 'nRad' refer to radiative and non-radiative contributions [124]. Considering the average values for the ellipses on graphene from Table 8.1 and the calculations for Γ_{Rad}, the time constants for each process were determined to be 5.2, 4.0, and 9.4 fs for T_{nRad}, T_{Rad}, and T_{HE}, respectively. Using Equation 8.2.5, the efficiency of electron transfer as a decay route for excited plasmons in the gold elliptical disks was calculated to be 20%.

Chapter 9: Conclusion

Electron transfer between metal nanostructures and graphene can be achieved with incident light. Energy absorbed by photons can either be transferred into phonons to produce heat, into photons from scattering, or into hot electrons which can be transferred to a neighboring material. Each of these contributions contribute to the extinction of incident light and their relative contributions are dependent on the size, shape, composition, and environment. Understanding how to measure these contributions will allow control and enhancement of plasmon decay routes through careful choice of particle morphologies.

This dissertation described computational techniques to calculate macroscopic and microscopic response of nanoparticles to incident photons and electrons. Macroscopic response included extinction of light through scattering and absorption. Periodic placement of nanoparticles in arrays was shown to create a Fano resonance between particle plasmons and diffracted light. Tuning the energy location of the Fano resonance was simulated by changing particle size, lattice dimensions, and the embedding refractive index.

Microscopic response of nanoparticles to incident irradiation was determined by simulations and experiments using electron energy loss spectroscopy. Localized excitation of electrons in gold nanostructures was examined in a scanning transmission electron microscope (STEM) with a sub-nanometer electron probe. Incident electrons lost measurable amounts of energy to the nanostructure which correspond to different types of plasmon modes. Excitation of a particular plasmon mode was observed to depend on the spatial location of the incident electron probe on the particle. These modes have been identified in the literature as 'bright' and 'dark' depending on whether they can be excited with incident photons.

Inclusion of graphene allowed investigation on the decay of plasmons into the graphene as a viable option for photocurrent. Plasmon bandwidth was measured to increase with the presence of graphene indicating increased damping of the oscillation. Assuming the increased damping was purely a result of electron transfer into the graphene, an efficiency of 20% was calculated. This indicated absorbed energy can be used to generate current through a monolayer of graphene by the mechanism of hot electron transfer.

Future work can be done to utilize and expand on the results in this dissertation. More complex morphologies can be fabricated with experiments to determine which structures produce the greatest efficiency of electron transfer to graphene as a route of plasmon decay. This would allow optimization of devices for photocurrent applications with a transparent graphene conductive layer. Computation models can be extended to account for graphene using models that treat the substrate as more than a dielectric layer. Finally, near-field interactions between adjacent nanostructures can be probed with incident electrons and photons to determine which plasmon modes are most efficient for electron transfer between plasmonic structures and graphene.

This work provides a method and gives direction for greater understanding of energy transfer between light and matter in the context of plasmon excitation. Nanostructures can be tuned to produce high efficiencies of plasmon decay through absorption for thermal enhancement, scattering for light guiding and sensing, and hot electron transfer for photocurrent or light induced doping of graphene. Greater insight into plasmonic interactions allows design and creation of new technologies and devices that have an impact on society as a whole.

BIBLIOGRAPHY

[1] I. Willner and B. Willner *Functional nanoparticle architectures for sensoric, optoelectronic, and bioelectronic applications*, Pure Appl. Chem. **74** 1773-1783, (2002).

[2] X. Liu, L. Zhao, H. Shen, H. Xu, and L. Lu, *Ordered gold nanoparticle arrays as surface-enhanced Raman spectroscopy substrates for label-free detection of nitroexplosives*, Talanta **83** 1023-1029, (2011).

[3] D. DeJarnette, B. Harbin, and D. K. Roper, *Geometric Effects on Far-Field Coupling Between Multipoles of Nanoparticles in Square Arrays*, J. Opt. Soc. B, **29**, 88-100, (2012).

[4] F. J. Beck, S. Mokkapati, A. Polman, and K. R. Catchpole, *Asymmetry in Photocurrent Enhancement by Plasmonic Nanoparticle Arrays Located on the Front or the Rear of Solar Cells*, Appl. Phys. Lett. **96**, 033113, (2010).

[5] H. Chen, L. Shao, T. Ming, K. C. Woo, Y. C. Man, J. Wang, and H. Q. Lin, *Observation of the Fano resonance in gold nanorods supported on high-dielectric-constant substrates*, ACS Nano **5** 6754-6763, (2011).

[6] J. D. Jackson, *Classical Electrodynamics*, Third Ed. John Wiley & Sons, Inc. (1999).

[7] D. J. Griffiths, *Introduction to Electrodynamics*, Third Ed. Prentice Hall, Inc. (1999).

[8] F. J. Garcia de Abajo, *Optical Excitation in Electron Microscopy*, Rev. Mod. Phys. **82**, 209-274, (2010).

[9] G. A. Shah, *Numerical Methods for Mie Theory of Scattering by a Sphere*, Obs. Bull. Ser. A, **2**, 42-63, (1977).

[10] W. L. Barnes, A. Dereux, and T. W. Ebbesen, *Surface Plasmon Subwavelength Optics*, Nature, **424**, 824-830, (2003).

[11] J. R. Sambles, G. W. Bradbery, and F. Z. Yang, *Optical-Excitation of Surface-Plasmons-an Introduction*, Contemp. Phys. **32**, 173-183, (1991).

[12] C. R. Lavers and J. S. Wilinson, *A Waveguide-Coupled Surface-Plasmon Sensor for an Aqueous Environment*, Sensor Actuat. B, **22**, 75-81, (1994).

[13] T. Klar, M. Perner, S. Grosse, G. von Plessen, W. Spirkl, and J. Feldmann, *Surface-Plasmon Resonances in Single Metallic Nanoparticles*, Phys. Rev. Lett. **80**, 4249-4252, (1998).

[14] P. K. Jain, K. S. Lee, H. El-Sayed, and M. A. El-Sayed, *Calculated Absorption and Scattering Properties of Gold Nanoparticles of Different Size, Shape, and Composition: Applications in Biological Imaging and Biomedicine*, J. Phys. Chem. B, **110**, 7238-7248, (2006).

[15] N. Calander and M. Willander, *Theory of surface-plasmon resonance optical-field enhancement at prolate spheroids*, J. Appl. Phys. **92**, 4878-4884, (2002).

[16] C. L. Haynes and R. P. Van Duyne, *Nanosphere lithography: A versatile nanofabrication tool for studies of size-dependent nanoparticle optics*, J. Phys. Chem. B **105**, 5599-5611, (2001).

[17] B. K. Canfield, S. Kujala, K. Jefimovs. T. Vallius, J. Turunen, and M. Kauranen, *Polarization effects in the linear and nonlinear optical responses of gold nanoparticle arrays*, J. Opt. A: Pure Apl. Opt. **7**, S110, (2005).

[18] N. Felidj, J. Aubard, G. Levi, A. Hohenau, J. R. Krenn, and F. R. Aussenegg, *Grating induced plasmon mode in gold nanoparticle arrays*, J. Chem. Phys. **123**, 221103, (2005).

[19] D. DeJarnette, J. Norman, D. K. Roper, *Attribution of Fano resonant features to plasmonic particle size, lattice constant, and dielectric wavenumber in square nanoparticle lattices*, Photon. Res. **2**, 15-23, (2014).

[20] C. L. Haynes, A. D. McFarland, L. Zhao, R. P. Van Duyne, G. C. Schatz, L. Gunnarsson, J. Prikulis, B. Kasemo, and M. Kall, *Nanoparticles Optics: The Importance of Radiative Dipole Coupling in Two-Dimensional Nanoparticle Arrays*, J. Phys. Chem. B, **107**, 7337-7342, (2003).

[21] S. Mokkapatil, F. J. Beck, A. Polman, and K. R. Catchpole, *Designing Periodic Arrays of Metal Nanoparticles for Light-Trapping Applications in Solar Cells*, Appl. Phys. Lett. **95**, 053115, (2009).

[22] L. Zhao, K. L. Kelly, and G. C. Schatz, *The Extinction Spectra of Silver Nanoparticle Arrays: Influence of Array Structure on Plasmon Resonance Wavelength and Width*, J. Phys. Chem. **107**, 7343-7350, (2003).

[23] H. O. Pierson, *Handbook of Carbon, Graphite, Diamond and Fullerenes: Properties, processing and Applications*, Noyes Publications, (1993).

[24] J. N. Coleman, U. Khan, W. J. Blau, Y. K. Gun'ko, *Small but Strong: A Review od the Mechanical Properties of Carbon Nanotube-Polymer Composites*, Carbon, **44**, 1624-1652, (2006).

[25] P. R. Wallace, *The Band Theory of Graphite*, Phys. Rev. **71**, 622-634, (1947).

[26] H. P Boehm, A. Clauss, G. Fischer, and U. Hofmann, *Surface Properties of Extremely Thin Graphite Lamellae*, Proceedings of the Fifth Conference of Carbon Pergamon Press, 73-80, (1962).

[27] A. K. Geim and K. S. Novoselov, *The Rise of Graphene*, Nature **6**, 183-191, (2007).

[28] K. S. Novoselov, A. K. Geim, S. V. Morozov, D. Jiang, Y. Zhang, S. V. Dubonos, I. V. Grigorieva, A. A. Firsov, *Electric Field Effect in Atomically Thin Carbon Films*, Science, **306**, 666-669, (2004).

[29] M. I. Katsnelson, *Graphene: Carbon in Two Dimensions*, Cambridge University Press, Cambridge, NY, (2012).

[30] B. G. Streetman and S. K. Banerjee, *Solid State Electronic Devices* 6th Ed, Pearson Educational Inc., Upper Saddle River, NJ, (2006).

[31] F. Wang, Y. Zhang, C. Tian, C. Girit, A. Zettl, M. Crommie, and Y. R. Shen, *Gate-Variable Optical Transformations in Graphene*, Science **320**, 1152793, (2008).

[32] T.J. Echtermeyer, L. Britnell, P.K. Jasnos, A. Lombardo, R.V. Gorbachev, A.N. Grigorenko, A.K. Geim A.C. Ferrari, and K.S. Novoselov, *Strong plasmonic enhancement of photovoltage in graphene*, Nat. Commun. **2**, 458, (2011).

[33] L. Wu, H. S. Chu, W. S. Koh, and E. P. Li, *Highly sensitive graphene biosensors based on surface plasmon resonance*, Opt. Express **18**, 14395-14399, (2010).

[34] N. J. M. Horing, *Coupling of graphene and surface plasmons*, Phys. Rev. B **80**, 193401, (2009).

[35] N. Papasimakis, Z. Luo, Z. X. Shen, F. De Angelis, E. Di Fabrizio, A. E. Nikolaenko, and N. I. Zhludev, *Graphene in a photonic metamaterial*, Opt. Express **18**, 8353-8359, (2010).

[36] T. J. Echtermeyer, L. Britnell, P. K. Jasnos, A. Lombardo, R. V. Gorbachev, A. N. Grigorenko, A. K. Geim, A. C. Ferrari, and K. S. Novoselov, *Strong plasmonic enhancement of photovoltage in graphene*, Nat. Comm. **2**, 458, (2011).

[37] Z. Fang, Z. Liu, Y. Wang, P. M. Ajayan, P. Nordlander, and N. J. Halas, *Graphene-Antenna sandwich detector*, Nano Lett. **?**, ?, (2012).

[38] S, Schedin, E. Lidorikis, A. Lombardo, V. G. Kravets, A. K. Geim, A. N. Grigorenki, K. S. Novoselov, and A. C. Ferrari, *Surface enhanced Raman Spectroscopy of graphene*, ACS Nano **4**, 5617-5616, (2010).

[39] Y. Liu, R. Cheng, L. Liao, H. Zhou, J. Bai, L. Liu, Y. Huang, and X. Duan, *Plasmon resonance enhanced multicolour photodetection bet graphene*, Nat. Comm. **8**, 135-138, (2009).

[40] F. Xia, T. Mueller, Y. Lin, A. Valdes-Garcia, and P. Avouris, *Ultrafast graphene photodetector*, Nat. Nanotech. **4**, 839-843, (2009).

[41] Z. Fang, Y. Wang, Z. Liu, A. Schlather, P. M. Ajayan, F. H. L. Koppens, P. Nordlander, and N. J. Halas, *Plasmon-induced doping of graphene*, ACS Nano, **6**, 10222-10228, (2012).

[42] J. Lee, S. Shim, B. Kim, and H. S. Shin, *Surface-enhanced Raman scattering of single- and few-layer graphene by the deposition of golds nanoparticles*, Chem. Eur. J. **17**, 2381-2387, (2011).

[43] P. V. Kamat, *Graphene-based nanoarchitecture. Anchoring semiconductor and metal nanoparticle on a two-dimensional carbon support*, J. Phys. Chem. Lett. **1**, 520-527, (2010).

[44] Z. Fang, Z. Liu, Y. Wang, P. M. Ajayan, P. Nordlander, and N. J. Halas, *GrapheneAntenna Sandwich Photodetector*, Nano LeTt. **12**, 3808-3813, (2012).

[45] R. R. Nair, P. Blake, A. N. Grigorenko, K. S. Novoselov, T. J. Booth, T. Stauber, N. M. R. Peres, A. K. Geim, *Fine Structure Constant Defines Visual Transparency of Graphene*, Science, **320**, 1308, (2008).

[46] A. Gruneis, K. Kummer, and D. V. Vyalikh, *Dynamics of Graphene Growth on a Metal Surface: A Time-Dependent Photoemission Study*, New J. Phys. **11**, 073050 (2009).

[47] A. Reina, X. Jia, J. Ho, D. Nezich, H. Son, V. Bulovic, M. S. Dresselhaus, and J. Kong, *Large Area, Few-Layer Graphene Films on Arbitrary Substrates by Chemical Vapor Deposition*, Nano Lett. **9**, 1, 30-35, (2009).

[48] X. Li, W. Cai, J. An, S. Kin, J. Nah, D. Yang, R. Piner, A. Velamakanni, I. Jung, E. Tutuc, S. K. Banerjee, L. Colombo, and R. S. Ruoff, *Large Area Synthesis of High-Quality and Uniform Graphene films on Copper Foils*, Science, **324**, 1312-1314, (2009).

[49] X. Li, C. W. Magnuson, A. Venugopal, R. M. Tromp, J. B. Hannon, E. M. Vogel, L. Colombo, and R. S. Ruoff, *Large-Area Graphene Single Crystals Grown by Low-Pressure Chemical Vapor Deposition of Methane on Copper*, J. Am. Chem. Soc. **133**, 2816-2819, (2011).

[50] X. Wang, H. You, F. Liu, M. Li, L. Wan, S. Li, Q. Li, Y. Xu, R. Tian, Z. Yu, D. Xiang, and J. Cheng, *Large-Scale Synthesis of Few-Layered Graphene using CVD*, Chem. Vap. Deposition **15**, 53-56, (2009).

[51] J. Coraux, A. T. N'Diaye, M. Engler, C. Busse, D. Wall, N. Buckanie, F. J. M. zu Heringdorf, R. van Gastel, B. Poelsema, and T. Michely, *Growth of Graphene on Ir(111)*, New J. Phys. **11**, 023006 (2009).

[52] Y. Q. Wu, P. D. Ye, M. A. Capano, Y. Wuan, Y. Sui, M. Qi, and J. A. Cooper, *Top Gated Graphene Field-Effect-Transistors formed by decomposition of SiC*, Appl. Phys. Lett. **92**, 092102, (2008).

[53] S. Shivaraman, R. A. Barton, X. Yu, J. Alden, L. Herman, M. V. S. Chandrashekhar, J. Park, P. L. McEuen, J. M. Parpia, H. G. Craighead, and M. G. Spencer, *Free-Standing Epitaxial Graphene*, Nano Lett. **9**, 3100-3105, (2009).

[54] Z. Sun, Z. Yan, E. Beitler, Y. Zhu, and J. M. Tour, *Growth of Graphene from Solid Carbon Sources*, Nature **468**, 549-552, (2010).

[55] D. Gunlycke, and P. Sheehan, *Local Peeling of Graphene*, Science **331**, 1146-1147, (2011).

[56] A. Dimiev, D. V. Kosynkin, A. Sinitskii, A. Slesarev, Z. Sun, and J. M. Tour, *Layer-by-Layer Remocal of Graphene for Device Patterning*, Science **331**, 1168-1172, (2011).

[57] Xuesong Li, Yanwu Zhu, Weiwei Cai, Mark Borysiak, Boyang Han, David Chen, Richard D. Piner, Luigi Colombo, and Rodney S. Ruoff, *Transfer of Large-Area Graphene Films for High-Performance Transparent Conductive Electrodes*, Nano Lett. **9**, 4359-4363, (2009).

[58] X. Liang, B. A. Sperling, I. Calizo, G. Cheng, C. A. Hacker, Q. Z., Y. Obeng, K. Yan, H. Peng, Q. Li, X. Zhu, H. Yuan, A. R. H. Walker, Z. Liu, L. M. Peng, and C. A. Richter, *Toward Clean and Crackless Transfer of Graphene*, ACS Nano **5**, 9144-9153, (2011).

[59] Y. Lee, S. Bae, H. Jang, S. Jang, S. E. Zhu, S. H. Sim, Y. I. Song, B. H. Hong, and J. H. Ahn, *Wafer-Scale Synthesis and Transfer of Graphene Films*, Nano Lett. **10**, 490-493, (2010).

[60] L. G. De Arco, Y. Zhang, A. Kumar, and C. Zhou, *Synthesis, Transfer, and Devices of Single- and Few-Layer Graphene by Chemical Vapor Deposition*, IEEE Transactions on Nanotechnology **8**, 135-138, (2009).

[61] L. D. Negro, N. N. Feng, and A. Gopinath, *Electromagnetic Coupling and Plasmon Localization in Deterministic Aperiodic Arrays*, J. opt. A: Pure Appl. Opt., **10**, 064013, (2008).

[62] D. K. Roper, W. Ahn, B. Taylor, and A. G. Dall Asen, *Enhanced Spectral Sensing by Electromagnetic Coupling With Localized Surface Plasmons on Subwavelength Structures*, IEEE Sens. J. **10**, 531-540, (2010).

[63] C. Noguez, *Optical Properties of Isolated and Support Metal Nanoparticles*, Opt. Mat, **27**, 1204-1211, (2005).

[64] K. B. Crozier, E. Togan, E. Simsek, and T. Yang, *Experimental Measurements of the Dispersion Relations of the Surface Plasmon Modes of Metal Nanoparticle Chains*, Opt. Express **15**, 17482-17493, (2007).

[65] A. Mary, D. Koller, A. Hohenau, J. Krenn, A. Bouhelier, and A. Dereux, *Optical absorption of torus-shaped metal nanoparticles in the visible range*, Phys. Rev. B **76**, 245422, (2007).

[66] K. L. Kelly, E. Coronado, L. L. Zhao, and G. C. Schatz, *The Optical Properties of Metal Nanoparticles: Tee Influence of Size, Shape, and Dielectric Environment*, J. Phys. Chem. B, **107**, 668-677, (2003).

[67] M. D. McMahon, *Effects of geometrical order on the linear and nonlinear optical properties of metal nanoparticles [dissertation]*, Nashville, TN, Vanderbilt University (2006).

[68] M Born and E. Wolf, *Principles of Optics*, 6th ed. Pergamon, Oxford, (1980).

[69] M. Meier and A. Wokaun, *Enhanced Fields on Large Metal Particles: Dynamic Depolarization*, Opt. Lett. **8**, 581-583, (1983).

[70] W. T. Doyle, *Optical Properties of a Suspension of Metal Spheres*, Phys. Rev. B, **39**, 9852-9858, (1989).

[71] M. A. Yurkin and A. G. Hoekstra, *The discrete dipole approximation: an overview and recent developments*, J. Quant. Spectrosc. Rad. **106**, 558-589, (2007).

[72] B. T. Draine and P. J. Flatau, *Discrete dipole approximation for scattering calculations*, J. Opt. Soc. Am. A, **11**, 1491-1499, (1994).

[73] B. T. Draine and P. J. Flatau, *Discrete dipole approximation for periodic targets: theory and tests*, J. Opt. Soc. Am. A, **25**, 2593-2603, (2008).

[74] B. T. Draine and P. J. Flatau, *User guide to the discrete dipole approximation code DDSCAT 7.2*, http://arXiv.org/abs/1202.3424, (2012).

[75] N. Guequet, and L. Henrard, *EELS and optical response of a noble metal nanoparticle in the frame of a discrete dipole approximation*, Ultramicroscopy **110**, 1075-1080, (2010).

[76] P. B. Johnson and R. W. Christy , *Optical constants of the noble metals*, Phys. Rev. B **6**, 43790, (1972).

[77] D. DeJarnette, P. Blake, G. T. Forcherio, D. K. Roper, *Far-field Fano resonance in nanoring lattice modeled from extracted, point dipole polarizability*, J. Appl. Phys. **115**, 024306, (2014).

[78] U. Fano, *Effects of Configuration Interaction on Intensities and Phase Shifts*, Phys. Rev. **124** 1866, (1961).

[79] D. DeJarnette, J. Norman, and D. K. Roper, *Spectral patterns underlying polarization-enhanced diffractive interference are distinguishable by complex trigonometry*, Appl. Phys. Lett. **101** 183104, (2012).

[80] C. R. Yonzon, E. Jeoung, S. Zou, G. C. Schatz, M. Mrksich, and R. P. Van Duyne, *A Comparative Analysis of Localized and Propagating Surface Plasmon Resonance Sensors: The Binding of Concanavalin A to a Monosaccharide Functionalized Self-Assembled Monolayer*, J. Am. Chem. Soc. **126**, 12669-12676, (2004).

[81] A. Ishimaru, S. Jaruwatanadilok, and Y. Kuga, *Generalized Surface Plasmon Resonance Sensors Using Metamaterials and Negative Index Materials*, Progress In Electromagnetics Research, **51**, 139-152, (2005).

[82] H. Kano, and S. Kawata, *Surface-Plasmon Sensor for Absorption-Sensitivity Enhancement*, Appl. Opt. **33**, 5166-5170, (1994).

[83] H. Xu and M. Kall, *Modeling the Optical Response of Nanoparticle-Based Surface Plasmon Resonance Sensors*, Sensor Actuat. B, **87**, 244-249, (2002).

[84] K. A. Willets and R. P. Can Duyne, *Localized Surface Plasmon Resonance Spectroscopy and Sensing*, Annu. Rev. Phys. Chem. **58**, 267-297, (2007).

[85] J. Zhang, T. Atay, and A. V. Nurmikko, *Optical Detection of Brain Cell Activity Using Plasmonic Gold Nanoparticles*, Nano Lett. **9**, 519-524, (2008).

[86] P. Blake, J. Obermann, B. Harbin, and D. K. Roper, *Enhanced Nanoparticle Response from Coupled Dipole Excitation for Plasmon Sensors*, IEEE Sens. J. **?**, ?, (?).

[87] S. Herranz, M. Bockova, M. D. Marazuela, J. Homola, M. C. Moreno-Bondi, *An SPR Biosensor for the Detection of Microcystins in Drinking Water*, Appl. Phys. Lett. **94**, 011102, (2009).

[88] J. J. Xiao, J. Ng, Z. F. Lin, and C. T. Chan, *Whispering Gallery Mode Enhanced Optical Force with Resonant Tunneling Excitation in the Kretschmann Geometry*, Appl. Phys. Lett. **94**, 011102, (2009).

[89] J. Homola, H. B. Lu, G. G. Nenninger, J. Dostalek, and S. S. Yee, *A Novel Multichannel Surface Plasmon Resonance Biosensor*, Sensor. Acuator. B-Chem. **76**, 403-410, (2001).

[90] V. Koubova, L. Karasova, J. Skvor, J. Homola, J. Dostalek, P. Tobiska, and J. Rosicky, *Detection of Foodborne Pathogens Using Surface Plasmon Resonance Biosensors*, Sensor. Actuator. B-Chem. **74**, 100-105, (2001).

[91] H. Vaisocherova, J. Snasel, T. Springer, H. Sipova, I. Rosenberg, J. Stephanek, J. Homola, *Surface Plasmon Resonance Study on HIV-1 Integrase Strand Transfer Activity*, Anal. Bioanal. Chem. **393**, 1165-1172, (2009).

[92] K. Kajikawa, *Localized Surface Plasmon Sensing Platform*, Proc. of SPIE **6642**, 66420J-1, (2007).

[93] S. Zou and G. C. Schatz, *Narrow Plasmonic/Photonic Extinction and Scattering Line Shapes for One and Two Dimensional Silver Nanoparticle Arrays*, J. Chem. Phys. **121**, 12606-12612, (2004).

[94] B. Auguie and W. L. Barnes, *Diffractive Coupling in Gold Nanoparticle Arrays and the Effect of Disorder*, Proc. of SPIE **6642**, 66420J-1, (2007).

[95] A. B. Evylukhin, C. Reinhardt, A. Seidel, B. S. Luk'yanchuk, and V. N. Chichkov, *Optical Response Features of Si-Nanoparticle Arrays*, Phys. Rev. B, **82**, 045404, (2010).

[96] V. G. Kravets, F. Schedin, and A. N. Grigorenko, *Extremely Narrow Plasmon Resonance Based on Diffraction Coupling of Localized Plasmons in Arrays of Metallic Nanoparticles*, Phys. Rev. Lett. **101**, 087403, (2008).

[97] E. Simsek, *On the Surface Plasmon Resonance Modes of Metal Nanoparticle Chains and Arrays*, Plasmonics, **4**, 223-230, (2009).

[98] M. Bass, C. DeCusatis, G. Li, V. N. Mahajan, J. Enoch, E. Van Stryland, *Handbook of Optics: Optical Properties of Materials, Nonlinear Optics, Quantum Optics*, McGraw-Hill Prof Med/Tech, October 19, 2009.

[99] SOPRA N&K Database. <http://refractiveindex.info/?group=CRYSTALS&material=ITO>.

[100] B. Bai, X. Li, I. Vartiainen, A. Lehmuskero, and G. Kang, *Anomalous Complete Opaqueness in a Sparse Array of Gold Nanoparticle Chains*, Appl. Phys. Lett. **99**, 081911, (2011).

[101] J. Aizpurua, P. Hanarp, D. Sutherland, M. Kall, G. Bryant, and F. Garcia de Abajo, *Optical properties of gold nanorings*, Phys. Rev. Lett. **90**, 057401, (2003).

[102] F. Hao, P. Nordlander, Y. Sonnefraud, P. Van Dorpe, and S. A. Maier, *Tunability of subradiant dipolar Fano-type plasmon resonance in metallic ring/disk cavities: Implications for nanoscale optical sensing*, ACS Nano **3**, 643-652, (2009).

[103] C. Huang, J. Ye, S. Wang, T. Stakenborg, and L. Lagae, *Gold nanoring as a sensitive plasmonic biosensor for on -chip DNA detection*, Appl. Phys. Lett. **100**, 173114, (2012).

[104] F. Hao, E. M. Larson, T. A. Ali, D. S. Sutherland, and P. Nordlander, *Shedding light on dark plasmons in gold nanorings*, Chem. Phys. Lett. **458**, 262, (2008).

[105] H. Y. Tseng, C. K. Lee, S. Y. Wu, T. T. Chi, K. M. Yang, J. Y. Wang, Y. W. Kiang, C. C. Yang, M. T. Tsai, Y. C. Wu, H. Y. E. Chou, and C. P. Chiang , *Au nanorings for enhancing absorption and backscattering monitored with optical coherence tomography*, Nanotechnology **21**, 11-16, (2010).

[106] N. Buford and M. El-Shenawee, *Plasmonic enhancement of irregular shape nano-patch for thin film silicon solar cells*, Appl. Comput. Electromagn. Soc. J. **28**, 359-373, (2013).

[107] T. V. Teperik and A Dediron, *Numerical analysis of an optical toroidal antenna coupled to a dipole emitter*, Phys. Rev. B **83**, 245408, (2011).

[108] M. Lisunova, J. Norman, P. Blake, G. T. Forcherio, D. F. DeJarnette, D. K. Roper, *Modulation of plasmonic Fano resonance by the shape of the nanoparticles in ordered arrays*, J. Phys. D: Appl. Phys. **46**, 5103, (2013).

[109] Y. Francescato, V. Giannini, and S. Maier, *Plasmonic systems unveiled by Fano resonances*, ACS Nano, **6**, 1830-1838, (2012).

[110] A. N. Shipway, E. Katz, and I. Willner, *Nanoparticle Arrays on Surfaces for Electronic, Optical, and Sensor Applications*, Chem. Phys. Chem. **1**, 18-52, (2000).

[111] W. Ahn, B. Taylor, A. G. Dall'Asen, and D. K. Roper, *Electroless Gold Island Thin Films: Photoluminescence and Thermal Transformation to Nanoparticle Ensembles*, Langmuir, **24**, 4174-4184, (2008).

[112] G. G. Jang and D. K. Roper, *Continuous Flow Electroless Plating Enhances Optical Features of Au Films and Nanoparticles*, J. Phys. Chem. C, **113**, 19228-19236, (2009).

[113] F. P. Schmidt, H. Ditlbacher, U. Hohenester, A. Hohenau, F. Hofer, and J. R. Krenn, *Dark plasmonic breathing modes in silver nanodisks*, Nano Lett. **12**, 5780-5783, (2012).

[114] A. L. Koh, K. Bao, I. Khan, W. E. Smith, G. Kothleitner, P. Nordlander, S. A. Maier, and D. W. McComb, *Electron energy loss spectroscopy (EELS) of surface plasmons in single silver nanoparticles and dimers: Influence of beam damage and mapping of dark modes*, ACS Nano **3**, 3015-3022, (2009).

[115] J. Nelayah, M. Kociak, O. Stephan, F. J. Garcia de Abajo, M. Tence, L. Henrard, D. Taverna, I. Pastoriza-Santos, L. M. Liz-Marzan, and C. Colliex, *Mapping Surface Plasmons on a Single Metallic Nanoparticle*, Nature Phys. **3**, 348-353, (2007).

[116] H. Duan, A. I. Fernandez-Dominguez, M. Bosman, S. A. Maier, and J. K. W. Yang, *Nanoplasmonics: Classical down to the nanometer scale*, Nano Lett. **12**, 1683-1689, (2012).

[117] A. L. Koh, A. I. Fernandez-Dominguez, D. W. McComb, S. A. Maier, and J. K. W. Yang, *High-resolution mapping of electron-beam-excited plasmon modes in lithographically defined gold nanostructures*, Nano Lett. **11**, 1323-1330, (2011).

[118] F. J. Garcia de Abajo and M. Kociak, *Probing the Photonic Local Density of States with Electron Energy Loss Spectroscopy*, Phys. Rev. Lett. **100**, 106804, (2009).

[119] U. Hohenester, H. Ditlbacher, and J. R. Krenn, *Electron-Energy-Loss Spectra of Plasmonic Nanoparticles*, Phys. Rev. lett. **103**, 106801, (2009).

[120] B. Luk'yanchuk, N. I. Zheludev, S. A. Maier, N. J. Halas, P. Nordlander, H. Giessen, and C. T. Chong, *The Fano resonance in plasmonic nanostructures and metamaterials*, Nat. Mat. **9**, 707-715, (2010).

[121] Y. B. Zheng, B. K. Juluri, X. Mao, T. R. Walker, and T. J. Huang, *Systematic investigation of localized surface plasmon resonance of long-range ordered Au nanodisk arrays*, J. Appl. Phys. **103**, 014308, (2008).

[122] J. Aizpurua, P. Hanarp, D. S. Sutherland, M. Kall, G. W. Bryant, and f. J. Garcia de Abajo, *Optical properties of gold nanorings*, Phys. Rev. Lett. **90**, 057401, (2003).

[123] M. Bruna and S. Borini, *Optical constants of graphene layers in the visible range*, Appl. Phys. Lett. **94**, 031901, (2009).

[124] A. Hoggard, L. Y. Wang, L. Ma, Y. Fang, G. You, J. Olson, Z. Liu, W. S. Chang, P. M. Ajayan, and S. Link, *Using the plasmon linewidth to calculate the time and efficiency of electron transfer between gold nanorods and graphene*, ACS Nano **7**, 11209-11217, (2013).

[125] C. Sonnichsen, T. Franzl, G. von Plessen, J. Feldmann, O. Wilson, P. Mulvaney, *Drastic reduction in plasmon damping in gold nanorods*, Phys. Rev. Lett. **88**, 077402, (2002).

Appendix A: Description of Research for Popular Publication

Nanoarchitectures for Next Generation Photonics

New results at the University of Arkansas, Fayetteville shines light on nanoscale optics at interfaces between two different materials. Energy transfer between two materials must be optimized for increased efficiency for next generation devices. Faster computers, more sensitive detectors, and even optical cloaking could be achieved by careful choice of nanoparticle architectures. Special arrangement of these small particles is capable of guiding and absorbing light in news ways not seen in nature.

Light is guided and absorbed by these particles through surface electron oscillation in response to the incident light. This special oscillation, called a plasmon resonance, typically decays as heat through absorption or as re-radiated light through scattering. Relative amounts of absorption and scattering can be controlled be careful design of particles parameters including size, shape, and the environment the particles are embedded in.

An additional decay route of a plasmon into an electron for applications involving photo current was characterized using a transmission electron microscope. Such a device could allow for faster computer processors using new hybrid electronics with both electrons and photons. Drew DeJarnette, a PhD candidate in Microelectronics-Photonics at the University of Arkansas under the guidance of Dr. D. Keith Roper, showed one way that light can be converted to elec-

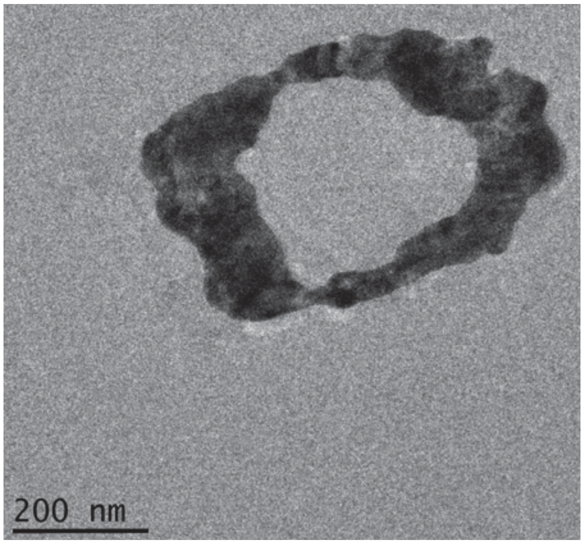

Figure A.1: Transmission electron micrograph of nanoring fabricated on silicon nitride membrane used to characterize plasmon excitation.

tricity using a characterization method called electron energy loss spectroscopy. This technique allowed DeJarnette to identify the relative efficiency of absorbed light converted to electrons of elliptical nanoparticles situated on a monolayer of carbon atoms, called graphene. DeJarnette said, ”Consideration of electron energy loss spectroscopy to probe plasmons as well as nanoparticles on graphene is already a topic in the literature. We simply combined these ideas together to create a new method of measuring light-induced electron transfer.”

Graphene is true two-dimensional materials discovered just one decade ago that possesses remarkable electronic and optical properties. Graphene has been shown to have one of largest electron mobilities of all known materials and can transport electron at nearly the speed of light. Additional electrons from light absorbed by metal nanoparticles located on top of graphene could be used in conjunction with the high electron mobility to create new devices and detectors. If the hybrid nanoparticle/graphene system can distinguish between the energies of the incident photons, a new type of camera could be created. Color images could be captured with limited light that is too faint or outside the visible receptors of human eyes.

Next generation computer processors are moving towards transferal of information using light to increase the speed at which information is processed. Integration of light in computer components necessitates the information be transfered into an electrical signal. Use of plasmon excitation and decay into electrical signals is one such path for new microprocessor device concepts. DeJarnette noted, ”The ability to characterize the transfer of energy from photons to electrons in individual nanostructures allows us optimize particle shape for maximal efficiency.” The team would like to expand this work to incorporate multiple types of particle shapes, sizes, and compositions to determine which specific nanoparticles would be best suited to create the next generation electrical devices.

Appendix B: Newly Created Intellectual Property

The following list indicate newly created intellectual property items.

1. Method to characterize plasmon decay through hot electron transfer into graphene using electron energy loss spectroscopy.
2. Method of fabricating plasmonic nanoparticles on graphene with a silicon nitride membrane as a substrate.
3. Identification of plasmon modes in rings and ellipses not previously discussed in the literature.

Appendix C: Potential Patent and Commercialization Aspects of listed Intellectual Property Items

C.1 Patentability of Intellectual Property

The three items listed were considered first from the perspective of whether or not the item could be patented.

1. Observing plasmon resonance using electron energy loss spectroscopy has been utilized in the literature for many years. The method of characterization here interprets results of existing characterization methods and does not constitute a patentable item.
2. The method used to create the nanostructures on silicon nitride with a graphene layer is a combination of existing methods. This item has the potential to be patented.
3. Predictions of a phenomenon using open source computational techniques does not constitute a patentable item.

C.2 Commercialization Prospects

The three items listed were then considered from the perspective of whether or not the item should be patented.

1. Not patentable.
2. This method was developed through combination of two established methods of lithography on TEM grids and graphene transfer. It is anticipated that the method is obvious to experts in the fields and a patent should not be sought.
3. Not patentable.

C.3 Possible Prior Disclosure of IP

The following items were discuses in a public forum or have published information that could impact the patentability of the listed IP.

1. Plasmon decay as electrons directly transfered to graphene has been discussed publicly as well a a method to characterize the transfer using photoluminescence. However, characterization this type of plasmon decay using electron energy loss spectroscopy has not been publicly disclosed.
2. The two methods of electron beam lithography on TEM grids and graphene transfer have been individually disclosed publicly, but not the combination therein.
3. Plasmon modes excited by electron beams using electron energy loss spectroscopy have been discussed in the literature. However, some of the specific resonances discussed in this work have not been publicly disclosed.

Appendix D: Broader Impacts of Research

D.1 Applicability of Research Methods to Other Problems

Methods used in completion of this work can be applied to other research problems at large. The use of electron energy loss spectroscopy to analyze plasmon decay routes from a single nanoparticle into graphene can be applied to consideration of alternate decay routes. Energy transfer from incident light to nanoparticles is dominated by plasmon resonance in the UV to IR spectral regime. Conversion of excited plasmons into alternate forms, such as heat for thermal applications and radiation for antennae, can be probed using this technique. Furthermore, plasmon decay routes from new sources not yet identified could also be probed using this methodology.

D.2 Impact of Research Results on U.S. and Global Society

Control and optimization of plasmon resonance and the associated decay as electrons for photocurrent applications has direct impact on global and society as a whole. Transferral of energy from light to conduction electrons in graphene has direct application in photodetector devices. Optimization of nanoparticle morphology for electron transfer efficiency is now possible using electron energy loss spectroscopy. Optimized devices would minimize losses through unwanted plasmon decay routes. Next generation electronic devices which would focus on light for transmittance of information would need a way to convert photons into electrical signals. This work provides a methodology for direct measurement and assessment of the feasibility of nanoparticles on graphene as a design for such devices. Additionally, sensitivity of plasmon resonance allows sensors and detectors to be developed for biological and chemical detection.

D.3 Impact of Research Results on the Environment

No known adverse environmental effects are known or are expected from the results of this dissertation. However, current research is being explored to determine nano toxicity from nanoparticles such as the ones fabricated for this work. Additionally, while the results of this work indicate a method to measure energy transfer from photons to electrons for photocurrent application, the results do not suggest a means of alternative energy in the form of photovoltaics.

Appendix E: Microsoft Project

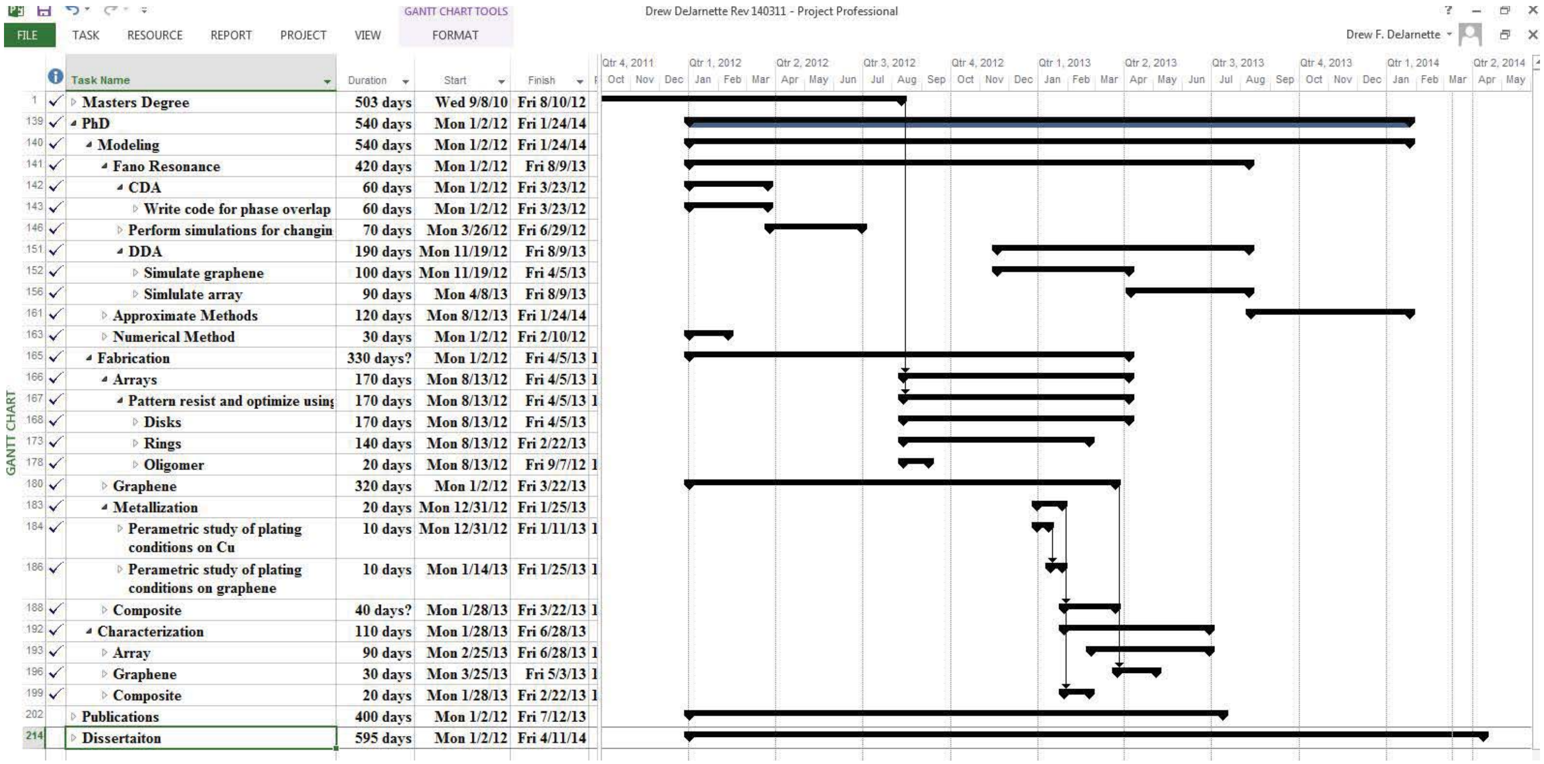

		Task Name	Duration	Start	Finish
1	✓	Masters Degree	503 days	Wed 9/8/10	Fri 8/10/12
139	✓	PhD	540 days	Mon 1/2/12	Fri 1/24/14
140	✓	Modeling	540 days	Mon 1/2/12	Fri 1/24/14
141	✓	Fano Resonance	420 days	Mon 1/2/12	Fri 8/9/13
142	✓	CDA	60 days	Mon 1/2/12	Fri 3/23/12
143	✓	Write code for phase overlap	60 days	Mon 1/2/12	Fri 3/23/12
146	✓	Perform simulations for changin	70 days	Mon 3/26/12	Fri 6/29/12
151	✓	DDA	190 days	Mon 11/19/12	Fri 8/9/13
152	✓	Simulate graphene	100 days	Mon 11/19/12	Fri 4/5/13
156	✓	Simlulate array	90 days	Mon 4/8/13	Fri 8/9/13
161	✓	Approximate Methods	120 days	Mon 8/12/13	Fri 1/24/14
163	✓	Numerical Method	30 days	Mon 1/2/12	Fri 2/10/12
165	✓	Fabrication	330 days?	Mon 1/2/12	Fri 4/5/13
166	✓	Arrays	170 days	Mon 8/13/12	Fri 4/5/13
167	✓	Pattern resist and optimize using	170 days	Mon 8/13/12	Fri 4/5/13
168	✓	Disks	170 days	Mon 8/13/12	Fri 4/5/13
173	✓	Rings	140 days	Mon 8/13/12	Fri 2/22/13
178	✓	Oligomer	20 days	Mon 8/13/12	Fri 9/7/12
180	✓	Graphene	320 days	Mon 1/2/12	Fri 3/22/13
183	✓	Metallization	20 days	Mon 12/31/12	Fri 1/25/13
184	✓	Perametric study of plating conditions on Cu	10 days	Mon 12/31/12	Fri 1/11/13
186	✓	Perametric study of plating conditions on graphene	10 days	Mon 1/14/13	Fri 1/25/13
188	✓	Composite	40 days?	Mon 1/28/13	Fri 3/22/13
192	✓	Characterization	110 days	Mon 1/28/13	Fri 6/28/13
193	✓	Array	90 days	Mon 2/25/13	Fri 6/28/13
196	✓	Graphene	30 days	Mon 3/25/13	Fri 5/3/13
199	✓	Composite	20 days	Mon 1/28/13	Fri 2/22/13
202		Publications	400 days	Mon 1/2/12	Fri 7/12/13
214		Dissertaiton	595 days	Mon 1/2/12	Fri 4/11/14

Appendix F: Identification of All Software Used in Research and Dissertation Generation

Computer #1:
  Model Number: Dell Optiplex 980,
  Serial Number: 3VNZPN1
  Location: BELL 2222
  Owner: University of Arkansas Chemical Engineering Dept.
Software #1:
  Name: Matlab 7.11.0 (R2010b)
  Purchased by: University of Arkansas Chemical Engineering Dept.
Software # 2:
  Name: Adobe Illustrator CS5
  Purchased by: University of Arkansas Site License
Software # 3:
  Name: Adobe Photoshop CS5
  Purchased by: University of Arkansas Site License

Computer # 2:
  Model Number: Dell Latitude E5510
  Serial Number: 9GJB8L1
  Location: Laptop
  Owner: Drew DeJarnette
Software # 1:
  Name: MiKTeX 2.9
  Purchased by: Open source program
Software # 2:
  Name: DDSCAT v. 7.3
  Purchased by: Open source code
Software # 3:
  Name: DDEELS v. 2.1
  Purchased by: Open source code

Appendix G: Publications Published, Submitted, and Planned

Publications

- M. Lisunova, X. Wei, D. DeJarnette, G. T. Forcherio, and D. K. Roper, *Photothermal response of plasmonic nanoconglomerates in films assembles by electroless plating*, RCS Adv. (2014). (Accepted)
- D. DeJarnette, P. Blake, G. T. Forcherio and D. K. Roper, *Far-field Fano resonance in nanoring arrays modeled from extracted, point dipole polarizability*, J. Appl. Phys. **115** 024306, (2014).
- D. DeJarnette, J. Norman, and D. K. Roper, *Attribution of Fano features to plasmonic particle size, lattice constant, and dielectric wavenumber in square nanoparticle lattices*, Photon. Res. **2** 15-23, (2014).
- J. Norman, D. DeJarnette, and D. K. Roper, *Polylogarithm-based computation of Fano resonance in arrayed dipole scatterers*, J. Phys. Chem. C **118** 627-634, (2014).
- M. Lisunova, J. Norman, P. Blake, G. T. Forcherio, D. DeJarnette, and D. K. Roper, *Modulation of plasmonic Fano resonance by shape of the nanoparticles in ordered arrays*, J. Phys. D: Appl. Phys. **46** 485103, (2013).
- D. K. Roper, P. Blake, D. DeJarnette, and B. Harbin, *Plasmon coupling enhanced in nanostructured chem/bio sensors*, Nano-Plasmonics:Advanced Device Applications 1st ed. James W. M. Chon and Kris Iniewski (ed.) CRC Press (2013).
- D. DeJarnette, J. Norman, and D. K. Roper, *Spectral patterns underlying polarization-enhanced diffractive interference are distinguishable by complex trigonometry*, Appl. Phys. Lett. **101** 183104, (2012).
- D. DeJarnette, B. Harbin, and D. K. Roper, *Geometric Effects on Far-Field Coupling Between Multipoles of Nanoparticles in Square Arrays*, J. Opt. Soc. B, **29**, 88-100, (2012).

Presentations

- D. DeJarnette, J. Normal, and D. K. Roper, *Nanooptics for refractive index sensors in fuel cycle application* Fuel Cycle Technologies Annual Review Meeting, Argonne, IL, 5-7 November, 2013. [invited] [**D.D.** presenter]
- D. DeJarnette, J. Normal, and D. K. Roper, *Fano resonance from constructive interference of scattered light in square plasmonic nanoparticle arrays tunable for wavelength specific application.* 6th International Conference on Surface Plasmon Photonics, Ottawa, Canada, 26-31 May, 2013 [**D.D.** presenter]
- D. K. Roper, D. DeJarnette, G. G. Jang, A. Russel, P. Blake, and K. Berry *Electromagnetically Active Nanocomposite Metamaterial Biosensors*, American Institute of Chemical Engineers [Annual Meeting], Pittsburgh, PA 28 October-2 November, 2012. [**D.K.R.** presenter]

- D. K. Roper, P. Blake, and D. DeJarnette, *Electron Optics of Self-Assembled Nanocomposite Metamaterials*, ,American Institute of Chemical Engineers [Annual Meeting], Pittsburgh, PA 28 October-2 November, 2012. [**D.K.R.** presenter]
- D. K. Roper, P. Blake, and D. DeJarnette, *EM active nanocomposite metamaterial sensors* 7th International Workshop on advanced Smart Materials, Bangalore, India, 27-28 July, 2012 [**D.K.R** presenter]
- D. DeJarnette, B. Harbin, and D. K. Roper, *Geometric Effects on Far-Field Coupling Between Multipoles of Nanoparticles in Square Arrays*, American Institute of Chemical Engineers [Annual Meeting], Minneapolis, Mn, 18 October, 2011. [**D.D.** presenter]

Publications Planned

- D. DeJarnette, G. Jang, P. Blake, and D. K. Roper, *Intensity and energy of far-field Fano resonance from multipole coupling in regular plasmonic nanolattices depends on polarization angle*, J. Opt. (2014). (Submitted)
- G. T. Forcherio, P. Blake, D. DeJarnette, and D. K. Roper, *Nanoring geometry effects on infrared Fano resonance and its sensitivity in square arrays*, Appl. Phys. Rev. (2014). (Submitted)
- D. DeJarnette and D. K. Roper, *Electron energy loss spectroscopy of gold nanoparticles on graphene*, Final Stages, (2014).
- D. DeJarnette and D. K. Roper, *A review of plasmonic interactions for ordered nanoparticle arrays*, Final Stages, (2014).